UNIVERSIDAD DE CHILE
FACULTAD DE CIENCIAS FÍSICAS Y MATEMÁTICAS
ESCUELA DE POSTGRADO

HEAT TRANSFER ENHANCEMENT STRATEGIES IN A SWIRL FLOW CHANNEL HEAT SINK BASED ON HYDRODYNAMIC RECEPTIVITY

TESIS PARA OPTAR AL GRADO DE
DOCTOR EN CIENCIAS DE LA INGENIERÍA, MENCIÓN FLUIDODINÁMICA

BENJAMÍN HERRMANN PRIESNITZ

PROFESOR GUÍA:
WILLIAMS CALDERÓN MUÑOZ

MIEMBROS DE LA COMISIÓN:
GERARDO DIAZ
RODRIGO SOTO BERTRÁN
ALVARO VALENCIA MUSALEM

SANTIAGO DE CHILE
2018

RESUMEN DE LA MEMORIA PARA OPTAR
AL TÍTULO DE DOCTOR EN CIENCIAS DE LA INGENIERÍA, MENCIÓN FLUIDODINÁMICA
POR: BENJAMÍN HERRMANN PRIESNITZ
FECHA: 2018
PROF. GUÍA: WILLIAMS CALDERÓN MUÑOZ

HEAT TRANSFER ENHANCEMENT STRATEGIES IN A SWIRL FLOW CHANNEL HEAT SINK BASED ON HYDRODYNAMIC RECEPTIVITY

El disipador de calor de canal con flujo espiral ha demostrado ser una alternativa prometedora para el manejo térmico de aplicaciones de alto flujo de calor, como electrónica y fotovoltaica concentrada. Temperaturas indeseadas son perjudiciales para el despempeño, la seguridad y la vida útil de estos dispositivos, por lo cual la investigación de tecnologías de enfriamiento de alto flujo de calor es una de las áreas de transferencia de calor con mayor actividad en la actualidad. En este trabajo se identifican estrategias eficientes para el aumento de la transferencia de calor en el disipador de calor de canal con flujo espiral estudiando la respuesta de las perturbaciones de temperatura frente a un forzamiento de momentum.

Se presentan simulaciones numéricas de los campos de velocidad y temperatura estacionarios en el dispositivo para investigar el efecto de los parámetros de diseño en el desempeño termohidráulico. La rotación del fluido induce una componente de flujo cruzado, y se encuentra que esto aumenta considerablemente la transferencia de calor convectiva debido a movimiento del fluido hacia la superficie de intercambio térmico.

En este estudio, se usa el marco de la teoría de estabilidad no modal para estudiar la estabilidad y receptividad del flujo estacionario en el canal de flujo espiral. Para este propósito, se formula un problema de perturbaciones lineales con un forzamiento armónico usando las aproximaciones de flujo local y paralelo.

Al contrario del flujo de Poiseuille plano, se encuentra que el crecimiento transiente de las perturbaciones es pequeño, y por lo tanto, no juega un rol en el mecanismo de transición. La transición se le atribuye a la inestabilidad de flujo cruzado que ocurre por el cambio en la forma del perfil de velocidad debido a los efectos rotacionales. Se lleva a cabo un experimento de visualización de flujo y se encuentra una concordancia cualitativa entre los patrones de difusión observados y el número de Reynolds crítico predicho.

La mayor amplificación en la respuesta de temperatura frente al forzamiento de momentum es presentada por vórtices y trazas longitudinales, seguidas por ondas viajeras radiales, y luego por ondas viajeras longitudinales. Se lleva a cabo un experimento para medir el desempeño del disipador de calor usando un flujo pulsante con frecuencias de forzamiento dentro del rango sugerido por el análisis de receptividad. Para obtener la misma temperatura de pared que en el caso sin pulsaciones, se observa una reducción de la potencia de bombeo de hasta un 26.6%, y usando la misma potencia de bombeo se obtiene un aumento del Nusselt de hasta un 10.3%. Este enfoque para identificar estrategias para el aumento de la transferencia de calor basado en física se puede extender a otras técnicas, por ejemplo, para seleccionar la longitud de onda en una superficie ondulada, la periodicidad de elementos de rugosidad, o la frequencia de vibraciones acústicas.

Abstract

The swirl flow channel heat sink has shown to be a promising alternative for thermal management of high heat flux applications, such as electronics and concentrated photovoltaics. Undesired temperatures are detrimental to the performance, safety, and lifetime of these devices, which is why high heat flux cooling technologies is one of the most active fields of heat transfer research today. This work identifies efficient heat transfer enhancement techniques in the swirl flow channel heat sink by studying the response of temperature disturbances to a momentum forcing input.

Numerical simulations of the steady state velocity and temperature fields in the device are carried our to investigate the effect of design parameters on thermohydraulic performance. Rotation of the fluid induces a crossflow component, this is found to enhance convective heat transfer considerably due to motion of fluid towards the heat exchange surface.

The framework of nonmodal stability theory is used to study the stability and receptivity of the steady state flow. For this purpose, a harmonically driven linear perturbation problem is formulated, and the methodology to apply the local and parallel flow approximations based on order of magnitude arguments is detailed.

As opposed to plane Poiseuille flow, transient growth of perturbations is found to be small, and consequently, it does not play a role in the transition mechanism. Transition is attributed to crossflow instability that occurs because of the change in the shape of the velocity profile due to rotational effects. A flow visualization experiment is conducted and qualitative agreement is found between the observed diffusion patterns and the critical Reynolds number predicted.

The largest amplification in the momentum to temperature response is presented by streamwise vortices and streaks, followed by axisymmetric inward travelling waves, and then by streamwise propagating waves. Experimental work is conducted to measure the performance of the heat sink using flow pulsations at the range of forcing frequencies suggested by the receptivity study. Compared to the unforced case, a lower wall temperature (up to 5°C cooler) was observed with pulsations, at the same imposed heat flux and flow rate. To get the same wall temperature as in the unforced case, a pumping power reduction of up to 26.6% was observed, and using the same pumping power resulted in up to a 10.3% Nusselt enhancement. This physics based approach to identify heat transfer enhancement strategies can be extended to other techniques, for instance, to select the wavelength of a wavy surface, the periodicity of surface roughness elements, or the frequency of acoustic vibrations.

Acknowledgments

I would like start by thanking my advisor, Williams Calderón, whose guidance and encouragement have been invaluable throughout my graduate studies. Williams trusted me with the freedom that allowed me to explore my own interests and, at the same time, challenged me to develop my independence as a researcher. I am grateful for his patience and optimism about my work.

I would also like to thank Rodrigo Soto for insightful discussions in his office and receiving me unannounced more than once. I also thank Gerardo Diaz and Alvaro Valencia for being on my thesis committee and for their advice along the way. My experimental work would not have been possible without Maria Luisa Cordero, Viacheslav Plotnikov, Andres Muñoz and Jorge Reyes who helped me with the laboratory equipment and setup, and Brian Zimmermann who machined the parts of the swirl flow channel heat sink.

It was a pleasure to share my early years in the doctoral program with Alfredo Aranda, Nicolás Amigo and Matías Quezada. Special thanks go to my *compadre* Felipe Escudero for short and sporadic conversations, where we celebrated and complained about our research and life as a graduate student.

During the last year of my studies, I was very fortunate to visit the University of California, Merced, and work with Gerardo Diaz on the experimental part of my research. I must thank Gerardo for being a wonderful host, he and his family received me kindly and made my stay in Merced a very pleasant experience. To everyone who was in and around Professor Diaz's group during my visit–Viacheslav Plotnikov, Andres Muñoz, Victor Zendejas and Sina Dehghan–sharing with you was a highlight of my time as a graduate student.

This thesis is dedicated to my wife Tania; her contagious happiness has motivated me every day of this journey, she has been a true source of inspiration and growth. Thanks to my parents, brother and sister, who where my first and most influential teachers. I would not be where I am without the constant love and support of my family.

I gratefully acknowledge the support of this work by the CONICYT-PCHA/Doctorado Nacional/2015-21150139 doctoral fellowship.

Contents

1 Introduction **1**
- 1.1 Motivation . . . 1
- 1.2 Historical perspective . . . 2
  - 1.2.1 Rotating boundary layer flows in channels . . . 2
  - 1.2.2 Hydrodynamic stability theory . . . 5
- 1.3 Overview of contributions . . . 8

2 Steady state flow **9**
- 2.1 Steady state governing equations . . . 9
- 2.2 Integral boundary layer equations and flow model . . . 12
  - 2.2.1 Momentum integral method . . . 13
  - 2.2.2 Entraining boundary layers . . . 14
  - 2.2.3 Non entraining boundary layers . . . 15
  - 2.2.4 Merged boundary layers . . . 16
- 2.3 Numerical methods . . . 16

3 Linear stability and receptivity analyses **18**
- 3.1 Linearized perturbation equations . . . 18
- 3.2 Choice of measure . . . 22
- 3.3 Growth of initial disturbances . . . 23
- 3.4 Response to componentwise external harmonic forcing . . . 23
- 3.5 Modal decomposition and order reduction . . . 24

4 Experimental methodology **25**
- 4.1 Device fabrication . . . 25
- 4.2 Experimental equipment and instrumentation . . . 26
- 4.3 Testing procedure . . . 29
- 4.4 Experimental calculations . . . 30

5 Results for steady state flow **31**
- 5.1 Validation of numerical results . . . 32
- 5.2 Structure of hydrodynamic boundary layers . . . 33
- 5.3 Streamlines and temperature field . . . 34
- 5.4 Design exploration . . . 36
  - 5.4.1 Effect of the channel height . . . 36
  - 5.4.2 Effect of the flow inlet angle . . . 37
  - 5.4.3 Effect of the Prandtl number . . . 38

5.4.4 Design recommendations . . . 40

6 Results for stability and receptivity 43

6.1 Base flow . . . 44

6.2 Mesh sensitivity and modal truncation . . . 46

6.3 Stability and transient growth . . . 46

6.4 Componentwise response . . . 50

6.5 Heat transfer enhancement strategies . . . 51

6.6 Case study: pulsating flow rate . . . 53

7 Conclusions 56

7.1 Concluding remarks . . . 56

7.2 Suggestions for future work . . . 58

Bibliography 60

A *Wolfram Mathematica* subroutines 68

B Heat sink fabrication schematic 70

C *NI Labview* code for data acquisition 74

List of Tables

2.1 Sensitivity analysis of the first step size. 17

4.1 Dimensions of the fabricated swirl flow minichannel heat sinks. 26
4.2 Instrumentation range and accuracy. 29

5.1 Design parameters for the experimental device of Ruiz and Carey. 32
5.2 Nondimensional numbers and predominant boundary layer structures. 34
5.3 Performance of swirl flow channel heat sink design variations at $\dot{V} = 400\mathrm{ml/min}$. 42

6.1 Local base flow parameters for $Re_o = 0.9$ at $r = 0.4r_o$. 46
6.2 Mesh sensitivity of the 10^{th} eigenvalue for $k = 1$ and $\theta_k = 0$. 46

List of Figures

1.1 Schematic of a swirl flow channel heat sink. 2
1.2 Sketch of von Kármán and Bödewadt boundary layer profiles. 3
1.3 Flow visualization of the boundary layer on a rotating disk. 5
1.4 Osborne Reynolds in 1883 standing behind his experiment in Manchester. . . 6
1.5 Reynolds experiment, repeated a century later using the original apparatus. . 7

2.1 Cavity with radial inflow and cylindrical system of coordinates. 9
2.2 Nondimensional boundary conditions for the swirl flow channel. 11
2.3 Schematic of possible radial velocity profiles in a rotating cylindrical cavity. . 12
2.4 Three dimensional boundary layer velocity profiles in streamline coordinates. 14

3.1 Parallel base flow schematic and local system of coordinates. 20

4.1 Swirl flow channel fabricated for the flow visualization experiment. 26
4.2 Heat sink fabricated for the performance measurement experiment. 27
4.3 Setup for the flow visualization experiment. 28
4.4 Setup for the performance measurement experiment. 28

5.1 Base configuration used for numerical simulations of the steady state flow. . 31
5.2 Comparison of numerical and experimental performance curves. 32
5.3 Classification of boundary layer structures on the θ_o–Re_o space. 33
5.4 Contours of dimensionless temperature T and streamlines in the r-z plane. . 35
5.5 Performance curves for channels of different heights. 37
5.6 Performance curves for channels with different flow inlet angles. 38
5.7 Suspension relative thermophysical properties. 39
5.8 Performance curves for working fluids with different Prandtl numbers. 40
5.9 Performance curves for design variations that present heat transfer enhancement. 41
5.10 Single phase microchannel heat sink comparison. 42

6.1 Base flow configuration used for the stability and receptivity analyses. 43
6.2 Base flow variables vs flow rate Reynolds number at different local radii. . . 44
6.3 Numerical and experimental performance variables vs Re_o. 45
6.4 Sensitivity of $\mathcal{R}_{u\tau}$ to the number of modes used for modal truncation. 47
6.5 Optimal growth $G(t)$ in the crossflow direction. 47
6.6 Maximum growth rate G_{max} as a function of k and θ_k for $Re_o = 0.8$. 48
6.7 Maximum growth rate G_{max} as a function of k and Re_o for $\theta_k = 90°$. 49
6.8 Maximum asymptotic growth rate for crossflow modes and flow visualization. 49

6.9 Response to radial momentum forcing $\mathcal{R}_{u\tau}$ as a function of k and θ_k. 50
6.10 Response to azimuthal momentum forcing $\mathcal{R}_{v\tau}$ as a function of k and θ_k. . . 50
6.11 Response to wall-normal momentum forcing $\mathcal{R}_{w\tau}$ as a function of k and θ_k. . 51
6.12 Response to wall-normal forcing of crossflow waves. 52
6.13 Response to radial forcing of streamwise propagating waves. 53
6.14 Experimental performance variables vs Re_o with and without forcing. 54
6.15 Heat sink performance response to flow pulsations. 54

Chapter 1

Introduction

1.1 Motivation

High heat flux removal is required in numerous industrial applications, such as electronics cooling [1], laser diodes cooling [2], and concentrated photovoltaics [3]. Thermal management is important for the performance, safety, and lifetime of these devices [4, 5], which is why high heat flux cooling technologies is one of the most active fields of heat transfer research today. Most promising solutions using single phase liquid cooled heat sinks include designs with jet impingement, flow through porous media, and microchannels [6, 7, 8]. During the last decade, several researchers have investigated single-phase heat transfer enhancement techniques for microchannels and minichannels with the goal of extending the applicability of single-phase cooling for critical applications, before more aggressive techniques, such as flow boiling, are considered [9, 10, 11, 12, 13]. Typical strategies include passive techniques, such as surface roughness, flow disruptions, channel curvature, out of plane mixing and fluid additives, as well as active techniques, such as vibration, electrostatic fields and flow pulsation [9]. In general, most advances on heat transfer augmentation are inspired by techniques that have proven to be successful in the past.

The swirl flow channel heat sink consists of an annular cavity closed at the top and bottom, where fluid is admitted through the outer radius, it spirals radially inward and exits through the inner radius, heat is removed from one of the channel walls whereas the other one is insulated. A schematic of the heat sink design is shown in Fig. 1.1. This device was designed and first studied by Ruiz and Carey in 2012 [14, 15]. In subsequent work in 2015, they built a prototype and compared experimental measurements using water to an analytical model for the heat and momentum transport in the heat sink. They found that the model underpredicted both, the pressure drop and total heat flux, due to not taking into account secondary flows and instabilities induced by rotation. The results from Ruiz and Carey also showed that the design is promising, a heat flux of 113W/cm^2 was achieved while maintaining a surface temperature below 80°C and a ratio of pumping power to heat rate of 0.03% [14, 15].

The objectives of this work are to study the effect of heat sink design on its thermohy-

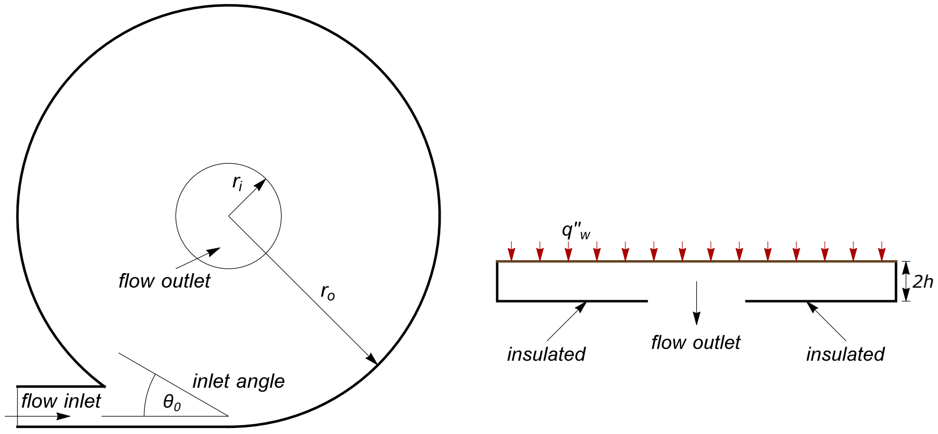

(a) (b)

Figure 1.1: Schematic of a swirl flow channel heat sink. (a) Top view. (b) Cross-sectional view.

draulic performance, determine the onset and mechanisms of hydrodynamic instabilities, and identify efficient strategies for heat transfer enhancement in the device. Specifically, numerical simulations of the velocity and temperature fields are used to investigate the influence of the device geometry, operating conditions, and working fluid on the steady state flow patterns. Subsequently, the effect of these flow patterns on the thermohydraulic performance of the heat sink is examined. Nonmodal stability theory is used to study the energy growth of linear perturbations of the steady state flow and determine the mechanisms responsible for the transition to turbulence. The same framework is used to study the spatio-temporal frequency response of temperature disturbances to a momentum forcing. The purpose of this is to identify efficient mechanisms to favor the emergence of specific flow structures that enhance convective heat transfer. Finally, experimental proof of concept is sought for a performance improvement strategy based on the latter receptivity analysis.

1.2 Historical perspective

A brief review of research on rotating boundary layer flows in channels and of the history of hydrodynamic stability theory are presented here.

1.2.1 Rotating boundary layer flows in channels

Rotating boundary layer flows are not only a subject of fundamental interest as prototype flows for three dimensional boundary layers, but they also appear in many diverse contexts. Many of these flows have features that appear in geophysics, such as atmospheric flows and wind-driven surface layers in the ocean. In turbomachinery, flows between rotating compressor and turbine disks can be idealized as flows confined between two co-rotating disks. These boundary layer flows are also present in rotor-stator systems, and have been used as models for aerodynamic applications such as the crossflow in a swept-wing [16].

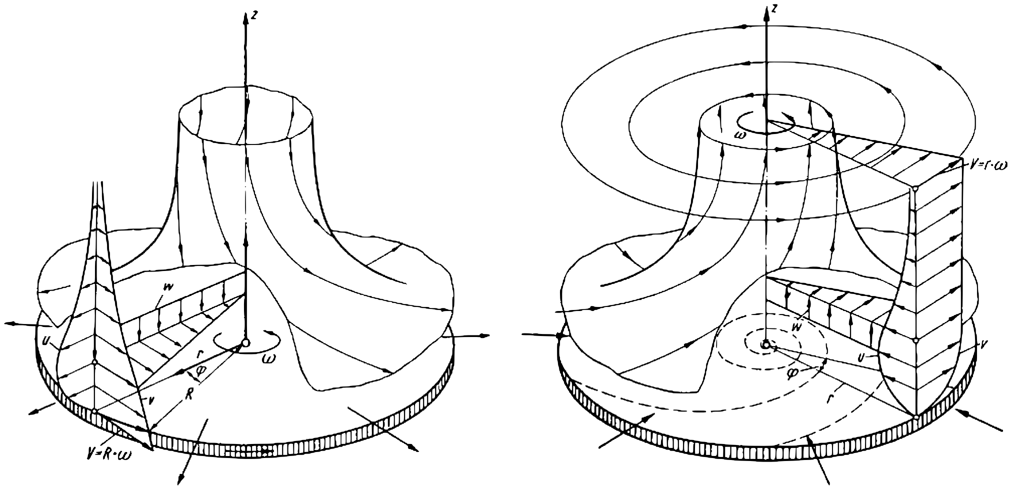

(*a*) (*b*)

Figure 1.2: Sketch of (*a*) von Kármán and (*b*) Bödewadt boundary layer profiles. From Ref. [16].

Ekman, von Kármán and Bödewadt boundary layers are three elemental cases of this family of rotating boundary layer flows. Since they are exact solutions of the Navier-Stokes equations they have often been used as canonical examples. In geophysical flows the Ekman layer is found when there is a geostrophic flow (there is a balance between Coriolis and horizontal pressure gradient) near a surface or boundary. The von Kármán boundary layer is the flow produced by an infinite disk rotating in quiescent fluid. Bödewadt studied the flow produced near a stationary disk immersed in fluid rotating at infinity with uniform angular velocity. A sketch of von Kármán and Bödewadt flows is showed in Fig. 1.2.

The flow inside a cylindrical cavity or channel is of basic interest in fluid mechanics. Throughout several decades, the problem has been addressed by many authors with different approaches and for different applications. The case of a rotating cavity with imposed radial outflow was investigated by Breiter and Pohlhausen in 1962 to study the performance of parallel disk pumps [17]. The authors provided an analytical solution to the linearized problem and a numerical solution to the equations of motion with the boundary layer approximation. Parallel disk turbomachinery was studied extensively by W. Rice, who did experimental measurements along with theoretical and numerical calculations [18, 19, 20]. In 1969 D. Wormley formulated an analytical model for short vortex chambers, and calculated the development of entraining and non entraining boundary layers in a non rotating cavity with radial inflow [21]. Owen et al. studied the case of radial inflow in a rotating cavity, solved non entraining boundary layers with integral methods and entraining boundary layers with a simple free disk or free vortex model. The line of work of these authors has continued the research of this flow with applications in cooling systems for gas turbines [22, 23, 24, 25]. Most research on heat transfer in cylindrical cavities has involved radial outflow in rotating and non-rotating configurations. Mochizuki and Yang conducted experimental studies of the heat transfer and friction loss for radial outflow and observed three distinct flow regimes: steady laminar, periodic laminar, and turbulent [26, 27]. Similar experiments were conducted by Suryanarayana et al. [28] who found correlations for the average Nusselt number and studied the effect of rotation. Devienne and Cognet studied experimentally the case of spiraling radial inflow for Newtonian and non-Newtonian fluids, and found the existence of secondary flows which are important for heat transfer[29]. Heat transfer using Al_2O_3 nanofluids in a cylindrical cavity with radial outflow was studied numerically by Roy et al. and also experimentally by Gherasim et al., heat transfer enhancement at an additional pumping cost was observed [30, 31, 32].

Recently, interest on cylindrical cavity flow has re-emerged, mainly because of novel applications such as miniature turbines and microchannel heat sinks [33, 34, 35, 36, 15]. Guha and Sengupta have published several articles regarding parallel disk turbines [37, 38, 39, 40, 41]. Using integral methods they obtained an approximate analytical solution, which is restricted to merged boundary layers. Ruiz and Carey studied the heat transfer in a spiraling radial inflow microchannel heat sink for high heat flux applications such as cooling electronics and concentrated solar photovoltaics systems [14, 15]. They used integral methods to formulate an analytical model and experiments to explore the design of the device.

Rotating boundary layer flows may become unstable to two different instabilities, designated Types I and II. Type I is usually referred to as inviscid or crossflow instability, and it is related to an inflection point in the velocity profile, similar to the Tollmien-Schlichting instability of the boundary layer on a flat plate, while Type II is called viscous instability and arises from centrifugal or Coriolis forces. Numerous works have been devoted to the investigation of these instabilities that appear in Bödewadt, Ekman and von Kármán boundary layers. The flow visualization record by Kobayashi, Kohama and Takamadate (1980) [42] shown in Fig. 1.3 is an excellent example that captures an image of the stationary crossflow modes in a rotating disk boundary layer.

The first experimental observation of stationary crossflow vortices and the first theoretical stability analysis for the rotating disc flow were presented by Gregory et al. [43]. Work on the modal and spatial stability continued with Malik, who computed the neutral curves for stationary disturbances using the parallel flow approximation [44]. The stability of Bödewadt flow was investigated by Savas who conducted spin-down experiments in a cylindrical cavity and observed spiral modes of instability similar to those found by Gregory et al. for the rotating disc [45, 46]. Savas observed an additional instability in the form of circular waves which propagated towards the axis of rotation before dying out. Lingwood followed by studying the absolute or convective nature of the instabilities [47]. Serre et al. carried out three dimensional direct numerical simulations in an annular cavity and also a cylindrical cavity. Their results show that the Bödewadt layer is unstable to axisymmetric circular radial waves and three dimensional multiarmed spiral waves [48]. MacKerrell conducted an asymptotic study of the Bödewadt layer flow in the limit of large Reynolds number. He showed that the stationary spiral instabilities observed experimentally can be described by a linear inviscid instability analysis [49]. Lopez et al. carried out a numerical investigation of the flow in an enclosed rotating cylinder with a stationary lower end wall, where the boundary layer has a profile that agrees with the Bödewadt layer solution [50]. They found that this boundary layer is not robust, suffering crossflow instability to multiarmed spiral waves via a supercritical Hopf bifurcation, as well as being susceptible to axisymmetric circular waves that travel radially inward. In a follow up study they showed that, in the absence of any external forcing, the circular waves are transitory, but low amplitude forcing can sustain them indefinitely [51]. Hydrodynamic stability of flows in cylindrical cavities for different

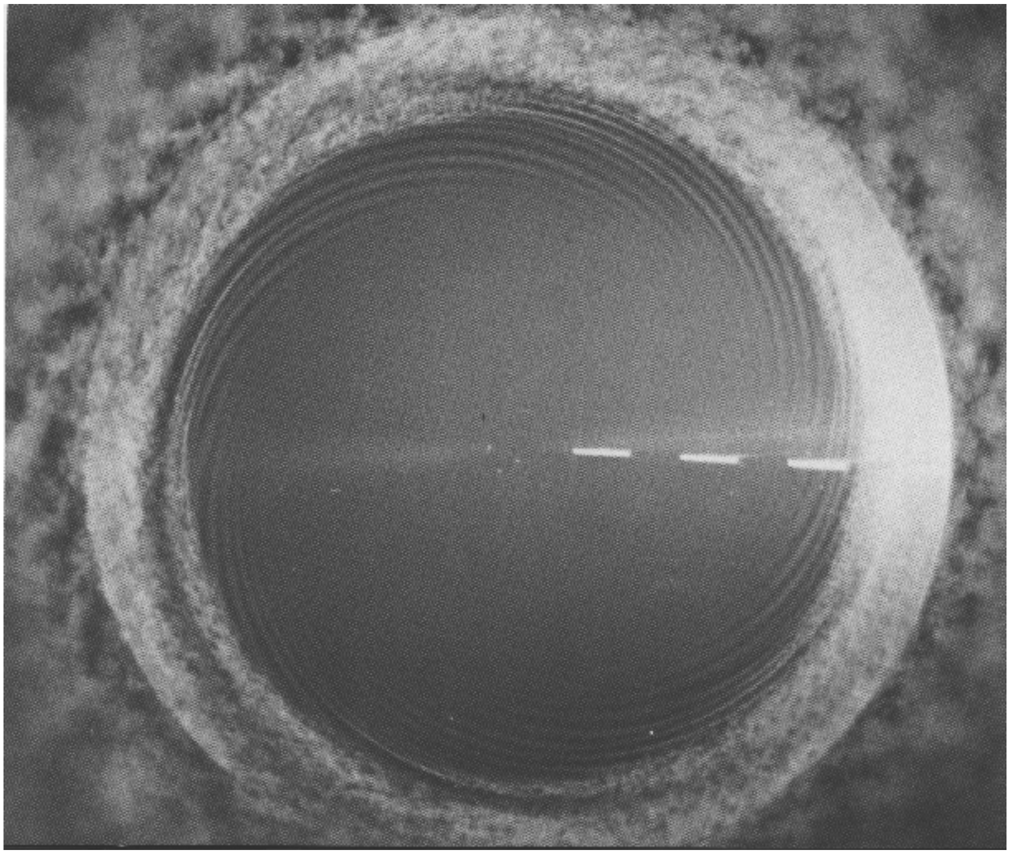

Figure 1.3: Flow visualization of the boundary layer on a rotating disk. From Ref. [42].

configurations has been investigated by several authors [52, 53, 54, 55].

1.2.2 Hydrodynamic stability theory

The celebrated experiment of Osborne Reynolds (1883) on the instability of a laminar flow in a tube, shown in Fig. 1.4, is often considered the foundational work of modern hydrodynamic stability theory [56]. His observations are illustrated in Fig. 1.5, which shows the behavior of a thin stream of dye injected at the glass tube entrance for three speeds, increasing from top to bottom. In the first photograph a straight dye stream is appreciated, the flow is laminar and remains so when subjected to small pertubations. In the second photograph the flow has become unstable, but the dye stream is quite distinct. In the last photograph the flow is turbulent and the dye spreads throughout the tube.

In the decades following Reynolds, important accomplishments in hydrodynamic stability theory were achieved. These early accomplishments predated the advantage of computational means and thus relied on simplifying assumptions and sophisticated asymptotic techniques [57]. Some of the now classical results, obtained throughout the past century, include the formulation of the viscous stability problem for parallel shear flows by Orr and Sommerfeld in 1907 and 1908, respectively [58, 59]. It was not until many years later, when Orszag in 1971 managed to get an accurate solution to this problem [60], and when Joseph in 1976 calculated

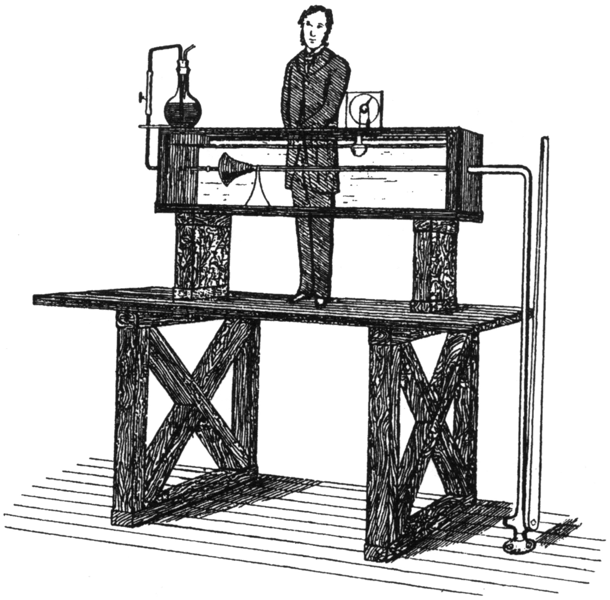

Figure 1.4: Osborne Reynolds in 1883 standing behind his experiment in Manchester. From Ref. [56].

the bounds on maximum energy growth [61]. Other important accomplishments are the theoretical prediction of waves in the Blasius boundary layer by Tollmien and Schlichting in 1929 and 1933 respectively [62, 63], and their experimental observation first by Schubauer and Skramstad in 1947 and followed by the work of Klebanoff et al. in 1962 [64, 65]. Secondary instability theory was developed by Orszag and Patera in 1983 and Herbert in 1988 [66, 67], and the identification of instability waves in a compressible boundary layer is attributed to Mack in 1963 [68]. Taylor rolls were discovered and described by Taylor in 1923 [69], the mathematical framework for spatial instabilities was established by Gaster in 1965 [70], rigorous criteria to distinguish between absolute or convective instabilities was determined by Huerre and Monkewitz in 1990 [71], and the parabolized stability equations were derived by Bertolotti et al. in 1992 and Chang and Malik in 1994 [72, 73].

Despite these remarkable accomplishments, many questions were left unanswered, including the discrepancy between the computed critical Reynolds number and the observed transitional Reynolds number in many wall-bounded shear flows, the nonexistence of finite critical Reynolds numbers for pipe or plane Couette flow, and a frequent failure to observe theoretically predicted structures in unforced experiments. Over the past two decades, nonmodal stability theory has emerged to provide a more complete picture of the linear perturbation dynamics for fluid flows using an initial-value problem formulation [75, 76, 77, 78, 79, 80, 81, 82]. The modal approach characterizes a flow as stable if all the eigenvalues of the dynamics operator are located on the left half of the complex plane. Nevertheless, for eigenvalues with negative real part, the flow may experience a large amplification due to linear transient growth before decaying asymptotically. The framework of nonmodal stability theory allows the incorporation of an external harmonic forcing term that may represent free-stream turbulence, wall roughness, acoustic perturbations or body forces among others. The response of the system to these external disturbances, i.e. receptivity of the flow, is determined by the particular solution to the harmonically driven problem. A componentwise receptivity

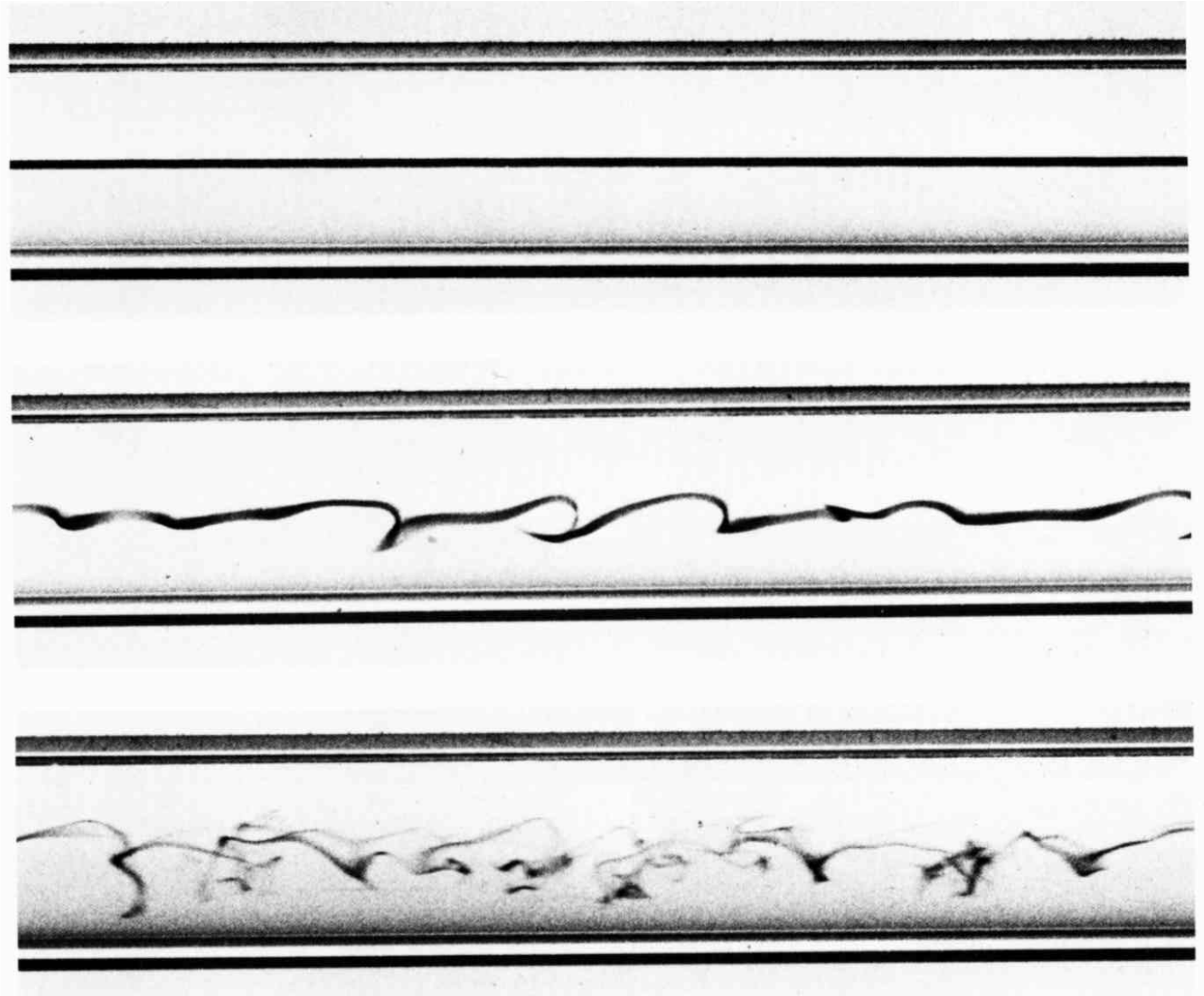

Figure 1.5: Reynolds experiment, repeated a century later by N. H. Johannesen and C. Lowe using the original apparatus preserved at the University of Manchester. The speed increases from top to bottom. From Ref. [74].

analysis for plane channel flows was carried out by Jovanović and Bamieh in 2005 [83]. Their results showed how the roles of Tollmien-Schlichting (T-S) waves, oblique waves, and streamwise vortices and streaks can be explained as input-output resonances of the spatio-temporal frequency responses. Therefore, one can identify efficient mechanisms to favor the emergence of specific flow structures. In a similar manner, a receptivity analysis can be used to identify efficient mechanisms to enhance convective heat transfer. This approach, based on physics rather than experience has not been presented elsewhere. In this work, we use the framework of nonmodal stability theory to study the response of temperature disturbances to a momentum forcing in the swirl flow channel heat sink.

1.3 Overview of contributions

The main contributions of this thesis are as follows:

- Numerical simulation of the steady state in a swirl flow channel heat sink.
- Classification of the steady state flow patterns in the space of governing nondimensional parameters.
- Investigation of the influence of the flow patterns on the thermohydraulic performance of the heat sink.
- Formulation of a forced linear initial value problem for nonmodal stability and receptivity analyses.
- Determination of the onset of hydrodynamic instability and the associated transition mechanism.
- Identification of efficient mechanisms to enhance heat transfer based on the componentwise response of temperature disturbances to a momentum forcing.
- Experimental demonstration of performance improvement using a receptivity based strategy.

Chapter 2 presents the formulation of the steady state flow problem along with the flow model and numerical methods developed to solve it. Chapter 3 presents the formulation of the forced linear perturbation problem and how the stability and receptivity analyses are carried out. Experimental work done is described in detail in Chapter 4, and results and discussions for steady state flow and for stability and receptivity are presented in Chapters 5 and 6, respectively.

Chapter 2

Steady state flow

This chapter presents the theoretical treatment of the fluid dynamics and heat transfer in a swirl flow channel operating in steady state. First, governing equations are presented, then a flow model is formulated to investigate hydrodynamic structure of boundary layers. The model considers mass and momentum transfer coupled between viscous boundary layers and an inviscid core region. A spatial initial value problem is obtained for the velocity field and the integral method along with an adaptive predictor-corrector Adams method is presented as a solution method. The temperature distribution is governed by a linear passive scalar transport equation and spatial discretization followed by matrix inversion is presented as a solution method.

2.1 Steady state governing equations

In this section, the governing equations for the steady state flow in an annular channel with imposed radial inflow are presented. The channel has a height $2h$, an outer radius r_o where the flow enters with an angle θ_o with respect to the tangent and temperature T_o, and an inner radius r_i where the flow exits. Using the cylindrical system of coordinates shown in Fig. 2.1, the steady state velocity vector is denoted $\mathbf{u} = u\hat{r} + v\hat{\theta} + w\hat{z}$.

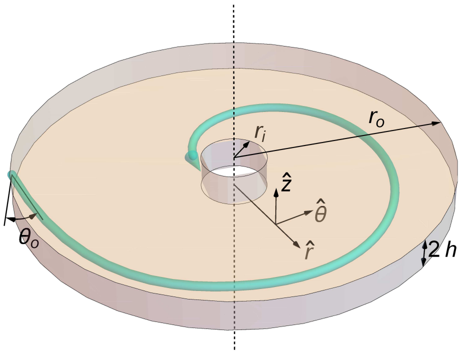

Figure 2.1: Cavity with radial inflow and cylindrical system of coordinates.

Mass, momentum, and thermal energy balances for the working fluid are governed by continuity, Navier-Stokes and thermal energy equations respectively. The main assumptions are that the fluid is incompressible and has constant physical properties, that the flow is in steady state and has axisymmetry, and that buoyant effects as well as viscous dissipation are negligible. With these assumptions, the governing equations become

$$\frac{1}{r^*}\frac{\partial\left(r^* u^*\right)}{\partial r^*}+\frac{\partial w^*}{\partial z^*}=0, \tag{2.1a}$$

$$u^*\frac{\partial u^*}{\partial r^*}+w^*\frac{\partial u^*}{\partial z^*}-\frac{v^{*2}}{r^*}=-\frac{1}{\rho}\frac{\partial p^*}{\partial r^*}+\nu\left(\frac{\partial^2 u^*}{\partial z^{*2}}+\frac{\partial}{\partial r^*}\left(\frac{u^*}{r^*}\right)+\frac{\partial^2 u^*}{\partial r^{*2}}\right), \tag{2.1b}$$

$$u^*\frac{\partial v^*}{\partial r^*}+w^*\frac{\partial v^*}{\partial z^*}+\frac{u^* v^*}{r^*}=\nu\left(\frac{\partial^2 v^*}{\partial z^{*2}}+\frac{\partial}{\partial r^*}\left(\frac{v^*}{r^*}\right)+\frac{\partial^2 v^*}{\partial r^{*2}}\right), \tag{2.1c}$$

$$u^*\frac{\partial w^*}{\partial r^*}+w^*\frac{\partial w^*}{\partial z^*}=-\frac{1}{\rho}\frac{\partial p^*}{\partial z^*}+\nu\left(\frac{\partial^2 w^*}{\partial z^{*2}}+\frac{1}{r^*}\frac{\partial w^*}{\partial r^*}+\frac{\partial^2 w^*}{\partial r^{*2}}\right), \tag{2.1d}$$

$$u^*\frac{\partial T^*}{\partial r}+w^*\frac{\partial T^*}{\partial z^*}=\alpha\left(\frac{\partial^2 T^*}{\partial z^{*2}}+\frac{\partial}{\partial r^*}\left(\frac{T^*}{r^*}\right)+\frac{\partial^2 T^*}{\partial r^{*2}}\right), \tag{2.1e}$$

where $()^*$ denotes dimensional variables, p is the static pressure, and T is the temperature. The fluid has density ρ, kinematic viscosity ν, and thermal diffusivity α. Governing equations are nondimensionalized by scaling flow variables as follows

$$r=\frac{r^*}{r_o},\quad z=\frac{z^*}{h},\quad u=\frac{u^*}{u_o},\quad v=\frac{v^*}{u_o},\quad p=\frac{p^*}{\rho\, u_o^2},\quad T=\frac{T^*-T_o}{T_s-T_o},$$

where the half-height of the channel h is used as vertical length scale, the outer radius r_o as horizontal length scale, and the radial velocity at the inlet of the cavity u_o is used as the scale for the velocities u and v. Pressure is nondimensionalized using the scale of the inertial terms, and T is nondimensionalized using T_o as the reference temperature and T_s-T_o as the characteristic temperature difference scale, where T_s is either the upper wall temperature T_w or the average temperature at the inner radius T_{i}. From the continuity equation, Eq. (2.1a), it follows that proper scaling for the axial velocity component is $w=w^*/(\varepsilon u_o)$. Where $\varepsilon=h/r_o$ is the aspect ratio of the channel. Therefore, the nondimensional form of Eqs. (2.1) is

$$\frac{1}{r}\frac{\partial\left(ru\right)}{\partial r}+\frac{\partial w}{\partial z}=0, \tag{2.2a}$$

$$u\frac{\partial u}{\partial r}+w\frac{\partial u}{\partial z}-\frac{v^2}{r}=-\frac{\partial p}{\partial r}+\frac{1}{Re_o}\left[\frac{\partial^2 u}{\partial z^2}+\varepsilon^2\left(\frac{\partial}{\partial r}\left(\frac{u}{r}\right)+\frac{\partial^2 u}{\partial r^2}\right)\right], \tag{2.2b}$$

$$u\frac{\partial v}{\partial r}+w\frac{\partial v}{\partial z}+\frac{uv}{r}=\frac{1}{Re_o}\left[\frac{\partial^2 v}{\partial z^2}+\varepsilon^2\left(\frac{\partial}{\partial r}\left(\frac{v}{r}\right)+\frac{\partial^2 v}{\partial r^2}\right)\right], \tag{2.2c}$$

$$\varepsilon^2\left(u\frac{\partial w}{\partial r}+w\frac{\partial w}{\partial z}\right)=-\frac{\partial p}{\partial z}+\frac{\varepsilon^2}{Re_o}\left[\frac{\partial^2 w}{\partial z^2}+\varepsilon^2\left(\frac{1}{r}\frac{\partial w}{\partial r}+\frac{\partial^2 w}{\partial r^2}\right)\right], \tag{2.2d}$$

$$u\frac{\partial T}{\partial r}+w\frac{\partial T}{\partial z}=\frac{1}{Re_o Pr}\left[\frac{\partial^2 T}{\partial z^2}+\varepsilon^2\left(\frac{\partial}{\partial r}\left(\frac{T}{r}\right)+\frac{\partial^2 T}{\partial r^2}\right)\right], \tag{2.2e}$$

these equations include the flow rate Reynolds number, Re_o, and the Prandtl number, Pr. These nondimensional numbers are defined as follows

$$Re_o = \varepsilon \frac{u_o h}{\nu} = \frac{u_o\, h^2}{\nu\, r_o}, \qquad Pr = \frac{\nu}{\alpha}.$$

Using a cavity with small aspect ratio, $\varepsilon \ll 1$, the terms of order $O(\varepsilon^2)$ can be neglected in Eqs. (2.2), resulting in the boundary layer approximation, as follows

$$\frac{1}{r}\frac{\partial (ru)}{\partial r} + \frac{\partial w}{\partial z} = 0, \tag{2.3a}$$

$$u\frac{\partial u}{\partial r} + w\frac{\partial u}{\partial z} - \frac{v^2}{r} = -\frac{\partial p}{\partial r} + \frac{1}{Re_o}\frac{\partial^2 u}{\partial z^2}, \tag{2.3b}$$

$$u\frac{\partial v}{\partial r} + w\frac{\partial v}{\partial z} + \frac{uv}{r} = \frac{1}{Re_o}\frac{\partial^2 v}{\partial z^2}, \tag{2.3c}$$

$$0 = -\frac{\partial p}{\partial z}, \tag{2.3d}$$

$$u\frac{\partial T}{\partial r} + w\frac{\partial T}{\partial z} = \frac{1}{Re_o Pr}\frac{\partial^2 T}{\partial z^2}, \tag{2.3e}$$

Due to the boundary layer approximation, the original elliptic partial differential equation (PDE) problem reduces to Eqs. (2.3), which is a parabolic PDE problem. Boundary conditions selected to model the swirl flow channel heat sink are shown in Fig. 2.2.

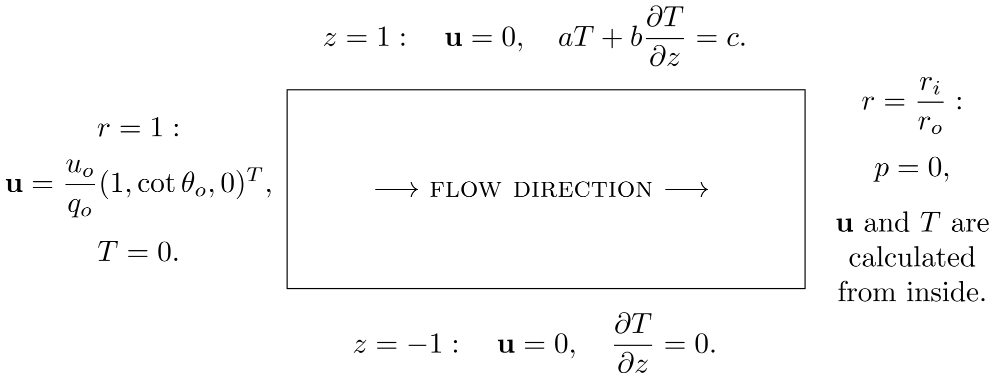

Figure 2.2: Nondimensional boundary conditions for the swirl flow channel.

Velocity components and temperature are specified at the channel inlet ($r = 1$), and no slip boundary conditions are used at both walls. For temperature, zero heat flux is imposed at the lower wall, and either a constant wall temperature or a constant heat flux is specified at the upper wall depending on the values of a, b and c. The reference pressure is set at the outlet ($r = r_\mathrm{i}/r_o$). The system of Eqs. (2.3) along with the boundary conditions shown in Fig. 2.2 constitute a well-posed parabolic PDE problem. The nondimensional numbers that characterize the problem are θ_o, Re_o and Pr.

2.2 Integral boundary layer equations and flow model

The flow is modelled considering two regions, (i) wall boundary layers where viscous effects are important, and (ii) an inviscid core region. Equation (2.3d) states that the static pressure remains constant through height of the cavity in the z direction. Inside the boundary layers, flow velocities in the radial and tangential directions are functions of r and z, while at the core they are assumed to depend only on r and are denoted as u_c and v_c. Figure 2.3 shows three possible radial velocity profiles that can be found for rotating flows inside the channel.

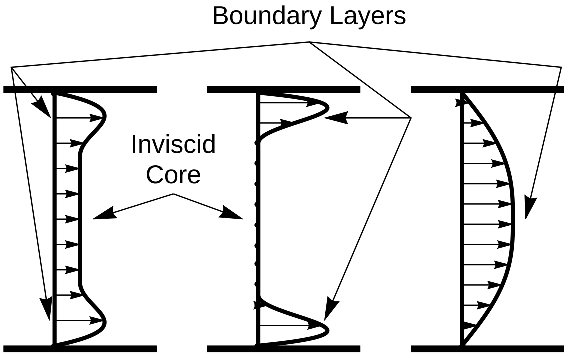

(a) Entraining boundary layers (b) Non entraining boundary layers (c) Merged boundary layers

Figure 2.3: Schematic of possible radial velocity profiles in a rotating cylindrical cavity.

If the flow enters the channel with a uniform velocity profile, very close to the inlet the radial velocity profile will resemble Fig. 2.3.(a) Due to rotational effects, a crossflow is induced inside the boundary layers, a maximum appears in the radial velocity and fluid from the core is drawn towards the walls. At the same time, boundary layers tend to grow. These two effects, flow entrainment and boundary layer thickening, compete against each other. Depending on the nondimensional numbers that characterize the hydrodynamics problem, θ_o and Re_o, the boundary layers may develop into the scenarios shown in Figs. 2.3.(b) or 2.3.(c). Radial velocity profile shown in Fig. 2.3.(b) corresponds to a case where, due to strong rotational effects, radial velocity in the core region becomes $u_c = 0$, which is expected for high Re_o and low θ_o. In this case, all the radial flow is forced to pass through the boundary layers and the fluid in the core remains in rotation without leaving the cavity. Radial velocity profile shown in Fig. 2.3.(c) corresponds to a case where, due to strong viscous effects, boundary layers grow until they merge. In this case, the core region disappears and velocity profiles are nearly parabolic, which is expected for low values of Re_o. Therefore, the structure of the hydrodynamic boundary layers is classified by considering these three possible scenarios: entraining, non entraining, and merged boundary layers.

A general flow model is formulated considering entraining boundary layers, as this is the most complex scenario. Furthermore, the models for non entraining and merged boundary layer are later derived as particular cases. A system of equations is obtained by considering mass and momentum transport coupled between these two regions, boundary layers and inviscid core. The continuity equation, Eq. (2.3a), is integrated across the cavity height, and momentum equations, Eqs. (2.3b)–(2.3d), are integrated inside the boundary layers.

Integral continuity:

$$\int_0^1 \frac{1}{r}\frac{\partial\,(ru)}{\partial r}\mathrm{d}z = 0. \tag{2.4}$$

Integral boundary layer r-momentum:

$$\int_0^\delta \left(\frac{1}{r}\frac{\partial\,(ru^2)}{\partial r} - \frac{u_c}{r}\frac{\partial\,(ru)}{\partial r} - \frac{v^2}{r}\right)\mathrm{d}z = -\delta\,\frac{\mathrm{d}p}{\mathrm{d}r} - \frac{1}{Re_o}\frac{\partial u}{\partial z}\bigg|_{z=0}. \tag{2.5}$$

Integral boundary layer θ-momentum:

$$\int_0^\delta \left(\frac{1}{r^2}\frac{\partial\,(r^2uv)}{\partial r} - \frac{v_c}{r}\frac{\partial\,(ru)}{\partial r}\right)\mathrm{d}z = -\,\frac{1}{\mathrm{Re}_o}\frac{\partial v}{\partial z}\bigg|_{z=0}. \tag{2.6}$$

Core $r-$momentum:

$$u_c\frac{\mathrm{d}u_c}{\mathrm{d}r} - \frac{v_c^2}{r} = -\frac{\mathrm{d}p}{\mathrm{d}r}. \tag{2.7}$$

Core $\theta-$momentum:

$$\frac{u_c}{r}\frac{\mathrm{d}\,(rv_c)}{\mathrm{d}r} = 0. \tag{2.8}$$

In Eqs. (2.4)–(2.8), δ is the thickness of the boundary layer, and the z coordinate is shifted so that $z = 0$ is at one of the channel walls and $z = 1$ is at the channel mid-plane. The flow field is symmetric with respect to the mid-plane, the shear stress vanishes at the inviscid core, and the velocity components are matched to those at the edge of the boundary layer, that is $w = \partial u/\partial z = \partial v/\partial z = 0$ at $z = 1$ and $u = u_c$ and $v = v_c$ at $z = \delta$.

2.2.1 Momentum integral method

The momentum integral method is used to solve the set of Eqs. (2.4)–(2.8) [16]. Using streamline coordinates, the velocity components in the streamwise direction, u_s, and in the crossflow direction, u_n, are defined as functions of $\eta = z/\delta(r)$ inside the boundary layers: $\frac{u_s}{q_c} = f(\eta)$ and $\frac{u_n}{q_c} = \gamma\, g(\eta)$. Where $\tan^{-1}\gamma$ is the angle between the directions of the surface limiting streamline and the streamline of the external flow at the core region, where the fluid velocity is q_c. A schematic of the velocity profiles in a three dimensional boundary layer in streamline coordinates is shown in Fig. 2.4.

The crossflow profile is induced because the lower-momentum fluid near the walls responds more rapidly to the pressure gradient than higher-momentum fluid in the core, therefore skewing the velocity vector across the boundary layer. With this coordinate system it is easy to see that the conditions that $f(\eta)$ and $g(\eta)$ must satisfy are: $f(0) = 0,\ g(0) = 0,\ f(1) = 1$, and $g(1) = 0$. Chosen functions are, a typical Kármán-Pohlhausen profile for the streamwise flow and a Mager crossflow profile [16, 84],

$$f(\eta) = 2\eta - 2\eta^3 + \eta^4, \qquad g(\eta) = (1-\eta)^2\, f(\eta). \tag{2.9}$$

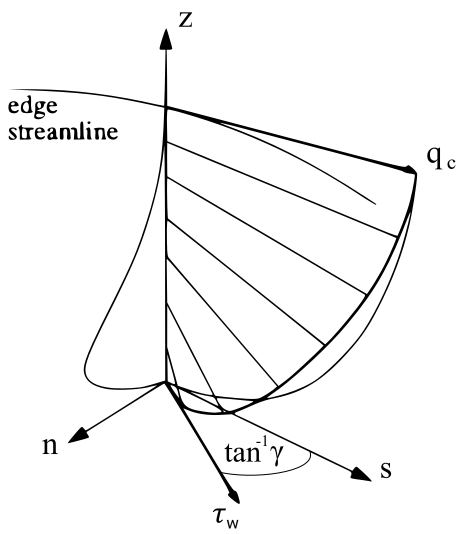

Figure 2.4: Three dimensional boundary layer velocity profiles in streamline coordinates.

Rewriting the radial and tangential velocity components in the cylindrical system of coordinates, we get

$$u(r,z) = \begin{cases} u_c(r)f(\eta) + \gamma(r)v_c(r)g(\eta), & \text{for } 0 \leq \eta \leq 1 \\ u_c(r), & \text{for } \eta > 1 \end{cases} , \tag{2.10}$$

$$v(r,z) = \begin{cases} v_c(r)f(\eta) - \gamma(r)u_c(r)g(\eta), & \text{for } 0 \leq \eta \leq 1 \\ v_c(r), & \text{for } \eta > 1 \end{cases} . \tag{2.11}$$

When u and v are replaced into the integral equations of motion, along with the chosen profile functions, the following constants are defined: $\alpha_0 = \left.\frac{\mathrm{d}f}{\mathrm{d}\eta}\right|_{\eta=0}$, $\alpha_1 = \int_0^1 f^2(\eta)\mathrm{d}\eta$, $\alpha_2 = \int_0^1 f(\eta)g(\eta)\mathrm{d}\eta$, $\alpha_3 = \int_0^1 g^2(\eta)\mathrm{d}\eta$, $\alpha_4 = \int_0^1 g(\eta)\mathrm{d}\eta$ and $\alpha_5 = \int_0^1 f(\eta)\mathrm{d}\eta$. Replacing these constants, a system of first order ordinary differential equations is obtained for the unknowns δ, u_c, v_c, γ, and p which are all functions only of r.

2.2.2 Entraining boundary layers

Using $(\,)'$ to denote differentiation with respect to r, we get the following set of equations for entraining boundary layers:

Continuity:

$$\begin{aligned} &\delta' \left[u_c(\alpha_5 - 1) - \gamma v_c \alpha_4\right] + u_c' \left[\delta(\alpha_5 - 1) + 1\right] - v_c'\ \delta\gamma\alpha_4 - \gamma'\ \delta v_c \alpha_4 \\ &\qquad = -\frac{1}{r}\left[u_c\delta(\alpha_5 - 1) + u_c + \delta\gamma v_c \alpha_4\right]. \end{aligned} \tag{2.12}$$

Boundary layer $r-$momentum:

$$\begin{aligned}
&\delta' \left[u_c^2(\alpha_5-\alpha_1)+\gamma u_c v_c(\alpha_4-2\alpha_2)+\gamma^2 v_c^2\alpha_3\right] \\
&+u_c'\ \delta\left[u_c(2\alpha_5-\alpha_1)+2\gamma v_c\alpha_2\right] \\
&+v_c'\ \delta\left[\gamma u_c(2\alpha_2-\alpha_4)-2\gamma^2 v_c\alpha_3\right] \\
&+\gamma'\ \delta\left[u_c v_c(2\alpha_2-\alpha_4)-2\gamma v_c^2\alpha_3\right]-p'\ \delta \\
&=\frac{\delta}{r}\left[u_c^2(\alpha_1-\alpha_5-\gamma^2\alpha_3)\ +\gamma u_c v_c(\alpha_4-4\alpha_2)+v_c^2(\alpha_1-\gamma^2\alpha_3)\right]-\frac{\alpha_0}{\delta Re_o}(u_c+\gamma v_c).
\end{aligned} \tag{2.13}$$

Boundary layer $\theta-$momentum:

$$\begin{aligned}
&\delta' \left[u_c^2\gamma\alpha_2+u_c v_c(\alpha_1-\alpha_5-\gamma^2\alpha_3)+\gamma v_c^2(\alpha_4-\alpha_2)\right] \\
&+u_c'\ \delta\left[2\gamma u_c\alpha_2+v_c(\alpha_5-\alpha_1+\gamma^2\alpha_3)\right] \\
&+v_c'\ \delta\left[u_c(\alpha_1-\gamma^2\alpha_3)+\gamma v_c(\alpha_4-2\alpha_2)\right] \\
&+\gamma'\ \delta\left[u_c^2\alpha_2-2\gamma u_c v_c\alpha_3+v_c^2(\alpha_4-\alpha_2)\right] \\
&=\frac{\delta}{r}\left[u_c v_c(\alpha_5-2\alpha_1+2\gamma^2\alpha_3)-2u_c^2\gamma\alpha_4+\gamma v_c^2(2\alpha_2-\alpha_4)\right]-\frac{\alpha_0}{\delta Re_o}(v_c-\gamma u_c).
\end{aligned} \tag{2.14}$$

For the momentum balance in the core, Eqs. (2.7) and (2.8) remain unchanged. The tangential velocity in the core, v_c, can be obtained analytically from Eq. (2.8) because $u_c \neq 0$ for entraining boundary layers

$$v_c = \frac{u_o/q_o}{r}. \tag{2.15}$$

This solution is the same as that of a free vortex, hence, angular momentum is conserved in the core for entraining boundary layers.

2.2.3 Non entraining boundary layers

For non entraining boundary layers we have that $u_c = 0$, therefore equations are simpler than those for the general case. In fact, Eq. (2.8) vanishes, leaving a system of 4 equations for the 4 unknowns δ, v_c, γ, and p. The resulting equations for continuity and boundary layer momentum balances are:

Continuity:

$$\delta'\gamma v_c v_c'\ \delta\gamma\alpha_4\gamma'\ \delta v_c\alpha_4 = \frac{\delta\gamma v_c\alpha_4}{r}. \tag{2.16}$$

Boundary layer $r-$momentum:

$$\delta'\gamma^2 v_c^2\alpha_3 - 2v_c'\ \delta\gamma^2 v_c\alpha_3 - 2\gamma'\ \delta\gamma v_c^2\alpha_3 - p'\ \delta = \frac{\delta v_c^2(\alpha_1-\gamma^2\alpha_3)}{r} - \frac{\alpha_0\gamma v_c}{\delta Re_o}. \tag{2.17}$$

Boundary layer $\theta-$momentum:

$$\delta'\gamma v_c^2(\alpha_4-\alpha_2) + v_c'\ \delta\gamma v_c(\alpha_4-2\alpha_2) + \gamma'\ \delta v_c^2(\alpha_4-\alpha_2) = \frac{\gamma\delta v_c^2(2\alpha_2-\alpha_4)}{r} - \frac{\alpha_0 v_c}{\delta Re_o}. \tag{2.18}$$

Radial momentum balance in the core is given by Eq. (2.7). The resulting model is very similar to that first used in 1985 by Owen *et al.* [85]. The only differences are the selection of the velocity profiles and the use of a skin friction correlation for the case of turbulent flow.

2.2.4 Merged boundary layers

When the upper and lower boundary layers meet, the inviscid core region disappears, hence we have that $\delta = 1$ and $\gamma = 0$. Substituting in Eqs. (2.12)–(2.14), we get the following equations for mass and momentum balances:

Continuity:

$$u_c' = -\frac{u_c}{r}. \tag{2.19}$$

Boundary layer $r-$momentum:

$$2u_c'\, u_c\alpha_5 + p' = \frac{v_c^2\alpha_1}{r} - \frac{u_c\alpha_0}{Re_o}. \tag{2.20}$$

Boundary layer $\theta-$momentum:

$$u_c'\, v_c\alpha_1 + v_c'\, u_c\alpha_1 = -\frac{2u_cv_c\alpha_1}{r} - \frac{v_c\alpha_0}{\mathrm{Re}_o}. \tag{2.21}$$

Equations (2.19)–(2.21) have been solved analytically by Guha and Sengupta for the case of a rotating cavity and parabolic velocity distributions along the channel gap [37, 38, 39, 40, 41]. Using the present notation, the radial and tangential velocity distributions obtained are

$$u_c = \frac{u_o/q_o}{\alpha_5 r}, \tag{2.22}$$

$$v_c = \frac{v_o/q_o}{\alpha_5 r}\exp\left[\frac{\alpha_0\alpha_5}{2(u_o/q_o)\alpha_1 Re_o}(1-r^2)\right], \tag{2.23}$$

The solution for the pressure drop is obtained by replacing the above expressions, Eqs. (2.22) and (2.23), into Eq. (2.20).

2.3 Numerical methods

This chapter describes the numerical methods used for the calculations the steady state velocity and temperature fields. All computations were carried out using the commercial software *Wolfram Mathematica 10.3.*

Using the momentum integral method presented in this chapter, the steady state fluid dynamics has been reduced to a spatial initial value problem. For entraining boundary layers, we have the system of 5 equations, Eqs. (2.12)–(2.14), for the 5 unknowns δ, u_c, v_c, γ, and p. If either merged or non entraining boundary layers develop, the governing equations are simplified.

A problem exists in starting the solution at the nondimensional radius $r = 1$ using a space marching technique, because the boundary layer thickness δ appears in a denominator in the equations. Therefore, an initial value other than $\delta = 0$ must be specified. Considering a first step of size Δr, an initial value for δ is estimated based on the flow over a flat plate. Hence, the following initial conditions are used at $r = 1$:

$$\delta = 5\sqrt{\frac{5\ \Delta r}{Re_o}},\ u_c = \frac{u_o}{q_o},\ v_c = \frac{u_o}{q_o}\cot\theta_o,\ \gamma = 0,\ p = 0.$$

It is noted that the solutions obtained do not depend critically upon the starting values of δ. In fact, solutions with changes of 50% on the initial values of δ are obtained using different values of Δr. These solutions differed less than 1% by $r = 1 - 10^{-6}$ and differed less than 0.1% by $r = 0.995$, as shown in Table 2.1.

Table 2.1: Sensitivity analysis of the first step size.

First step size	δ at position		
$\Delta r \times 10^8$	$r = 1$	$r = 1 - 10^{-6}$	$r = 0.995$
0.5	0.0007	0.0116	0.5342
1	0.0010	0.0117	0.5342
5	0.0022	0.0118	0.5342

In some cases, a very small step size is required for numerical stability near $r = 1$. An adaptive multi-step method is used to reduce the computational time. A 4^{th} order Adams predictor-corrector integration scheme is used, initialized with a 4^{th} order Runge Kutta. Solution is started with $\Delta r = 10^{-8}$ and the local truncation error between the predictor and corrector steps is evaluated to adjust the step size. The subroutines programmed for the Runge Kutta and adaptive Adams method are presented in Appendix A. During each step, the results are checked to see if boundary layers become non entraining, which happens when $u_c = 0$. In that case, the corresponding simplified Eqs. (2.16),(2.17),(2.18) and (2.7) are solved using the same method to calculate δ, v_c γ, and p. Merging of the boundary layers is also monitored during each step. If the boundary layer thickness reaches $\delta = 1$, then u_c is obtained from Eq. (2.22), and v_c and p are calculated using the same numerical method from Eqs. (2.20) and (2.21).

Once the velocity field is known, solving Eq. (2.3e) to obtain the steady state temperature field is a linear passive scalar transport problem. Therefore, it can be solved using spatial discretization followed by matrix inversion. Specifically, we use the Chebyshev pseudospectral collocation method to discretize in the z direction and a 2^{nd}-order upwind scheme to discretize in the r direction [86, 87, 88]. The subroutine used to calculate the Chebyshev differentiation and integration matrices is shown in Appendix A.

Chapter 3

Linear stability and receptivity analyses

The boundary layer nature of the steady state in a swirl flow channel was presented in the previous chapter. In this chapter we are concerned with small perturbations about this steady state flow, in particular the time evolution of initial disturbances and the response to external forcing. The formulation of a harmonically driven linear initial-value problem for the perturbation dynamics in a swirl flow channel is detailed. The methodology to apply the local and parallel flow approximations based on order of magnitude arguments is presented.

Stability of the flow is determined by the amplification or dampening of initial disturbances in time, i.e. stability of the flow, is determined by the homogeneous solution of the resulting problem. The harmonic forcing term may represent free-stream turbulence, wall roughness, acoustic perturbations or body forces among others. The response of the system to these external disturbances, i.e. receptivity of the flow, is determined by the particular solution of the problem.

3.1 Linearized perturbation equations

Through this section we cover in detail the formulation of the stability and receptivity problems for the swirl flow channel. The approximations presented allow these problems to be solved using standard nonmodal techniques taken from, e.g., Schmid and Henningson, 2001 [80].

The steady state flow is governed by the boundary layer Eqs. (2.3). In this chapter we use capital letters to denote the steady state variables, hence $\mathbf{U} = (U, V, W)^T$ is the velocity field in cylindrical coordinates $(\hat{\mathbf{r}}, \hat{\boldsymbol{\theta}}, \hat{\mathbf{z}})$, P is the pressure, and T is the temperature. Using this notation, the dimensional steady state equations become

$$\frac{1}{r}\frac{\partial (rU)}{\partial r} + \frac{\partial W}{\partial z} = 0, \tag{3.1a}$$

$$U\frac{\partial U}{\partial r} + W\frac{\partial U}{\partial z} - \frac{V^2}{r} = -\frac{1}{\rho}\frac{\partial P}{\partial r} + \nu\frac{\partial^2 U}{\partial z^2}, \tag{3.1b}$$

$$U\frac{\partial V}{\partial r} + W\frac{\partial V}{\partial z} + \frac{UV}{r} = \nu\frac{\partial^2 V}{\partial z^2}, \tag{3.1c}$$

$$0 = -\frac{1}{\rho}\frac{\partial P}{\partial z}, \tag{3.1d}$$

$$U\frac{\partial T}{\partial r} + W\frac{\partial T}{\partial z} = \alpha\frac{\partial^2 T}{\partial z^2}, \tag{3.1e}$$

$$\begin{aligned} &z = h: \quad \mathbf{U} = 0, \quad \kappa\frac{\partial T}{\partial z} = q''_w, \qquad r = r_o: \quad \mathbf{U} = U_o\left(1, \cot\theta_o, 0\right)^T, \quad T = T_o, \\ &z = -h: \quad \mathbf{U} = 0, \quad \frac{\partial T}{\partial z} = 0, \qquad r = r_\mathrm{i}: \quad P = 0, \end{aligned} \tag{3.1f}$$

where ρ is the density, ν is the kinematic viscosity, and κ and α are thermal conductivity and thermal diffusivity, respectively. Boundary conditions are shown in Eq. (3.1f): no slip and a constant heat flux at the upper wall, no slip and zero heat flux at the lower wall, specified velocity components and temperature at the inlet, and a reference pressure is set at the outlet.

Linearizing the incompressible Navier-Stokes equations and energy equations in cylindrical coordinates about an axisymmetric base flow yields the following system of equations

$$\frac{\partial u}{\partial r} + \left(\frac{u}{r}\right)_c + \frac{1}{r}\frac{\partial v}{\partial \theta} + \frac{\partial w}{\partial z} = 0, \tag{3.2a}$$

$$\begin{aligned} &\frac{\partial u}{\partial t} + U\frac{\partial u}{\partial r} + \frac{V}{r}\frac{\partial u}{\partial \theta} + w\frac{\partial U}{\partial z} + \left(u\frac{\partial U}{\partial r} + W\frac{\partial u}{\partial z}\right)_{np} - \left(\frac{2Vv}{r}\right)_c = \\ &\qquad -\frac{\partial p}{\partial r} + \frac{1}{Re}\left[\frac{\partial^2 u}{\partial r^2} + \frac{1}{r^2}\frac{\partial^2 u}{\partial \theta^2} + \frac{\partial^2 u}{\partial z^2} + \left(\frac{1}{r}\frac{\partial u}{\partial r} - \frac{u}{r^2} - \frac{2}{r^2}\frac{\partial v}{\partial \theta}\right)_c\right] + f_u, \end{aligned} \tag{3.2b}$$

$$\begin{aligned} &\frac{\partial v}{\partial t} + U\frac{\partial v}{\partial r} + \frac{V}{r}\frac{\partial v}{\partial \theta} + w\frac{\partial V}{\partial z} + \left(u\frac{\partial V}{\partial r} + W\frac{\partial v}{\partial z}\right)_{np} + \left(\frac{uV + Uv}{r}\right)_c = \\ &\qquad -\frac{1}{r}\frac{\partial p}{\partial \theta} + \frac{1}{Re}\left[\frac{\partial^2 v}{\partial r^2} + \frac{1}{r^2}\frac{\partial^2 v}{\partial \theta^2} + \frac{\partial^2 v}{\partial z^2} + \left(\frac{1}{r}\frac{\partial v}{\partial r} - \frac{v}{r^2} + \frac{2}{r^2}\frac{\partial u}{\partial \theta}\right)_c\right] + f_v, \end{aligned} \tag{3.2c}$$

$$\begin{aligned} &\frac{\partial w}{\partial t} + U\frac{\partial w}{\partial r} + \frac{V}{r}\frac{\partial w}{\partial \theta} + \left(u\frac{\partial W}{\partial r} + w\frac{\partial W}{\partial z} + W\frac{\partial w}{\partial z}\right)_{np} = \\ &\qquad -\frac{\partial p}{\partial z} + \frac{1}{Re}\left[\frac{\partial^2 w}{\partial r^2} + \frac{1}{r^2}\frac{\partial^2 w}{\partial \theta^2} + \frac{\partial^2 w}{\partial z^2} + \left(\frac{1}{r}\frac{\partial w}{\partial r}\right)_c\right] + f_w, \end{aligned} \tag{3.2d}$$

$$\frac{\partial \tau}{\partial t} + U\frac{\partial \tau}{\partial r} + \frac{V}{r}\frac{\partial \tau}{\partial \theta} + w\frac{\partial T}{\partial z} + \left(u\frac{\partial T}{\partial r} + W\frac{\partial \tau}{\partial z}\right)_{np} = \frac{1}{RePr}\left[\frac{\partial^2 \tau}{\partial r^2} + \frac{1}{r^2}\frac{\partial^2 \tau}{\partial \theta^2} + \frac{\partial^2 \tau}{\partial z^2} + \left(\frac{1}{r}\frac{\partial \tau}{\partial r}\right)_c\right] + f_\tau, \quad (3.2e)$$

where $\mathbf{u} = (u, v, w)^T$ is the perturbation velocity, p is the perturbation pressure, and τ is the perturbation temperature. We have added an external forcing term $(f_u, f_v, f_w, f_\tau)^T$ to the momentum and energy equations, which will later be used for the receptivity analysis. The terms inside the parentheses $(\ )_c$ and $(\ )_{np}$ correspond to curvature and non-parallel flow effects respectively. Equations (3.2) have been nondimensionalized using the half-height of the channel h as the characteristic length scale, the velocity magnitude $\sqrt{U^2+V^2}$ at the midplane of the channel as the characteristic velocity scale, T_o is set as the temperature reference, and $T_\mathrm{i} - T_o$ is used as the characteristic temperature difference scale, where T_i is the average temperature at the inner radius (outlet). Therefore, here $Re = \sqrt{U^2+V^2}h/\nu$ is a local Reynolds number.

In this study, we are concerned with the local behavior of flow structures of length scale h, around a certain radial station r. If the radius is sufficiently large compared to the length scales of interest i.e., $\varepsilon = h/r \ll 1$, the flow can be regarded as locally Cartesian in the coordinates $(\hat{\mathbf{r}}, r\hat{\boldsymbol{\theta}}, \hat{\mathbf{z}})$, therefore the curvature terms $(\ )_c$ can be neglected. Due to the boundary layer nature of the flow, the normal velocity component W is much smaller than those parallel to the walls U and V, and radial dependence of $\mathbf{U}$ and T is much smaller than their dependence in the direction normal to wall. In fact, these are smaller by a factor of order $O(\varepsilon)$, and by neglecting them we get $\mathbf{U} \approx (U(z), V(z), 0)^T$ and $T \approx T(z)$. This results in the elimination of the non-parallel flow effects denoted by $(\ )_{np}$, which is known in literature as the parallel flow approximation. Both, the local system of coordinates and a schematic of the parallel base flow are shown in Fig. 3.1.

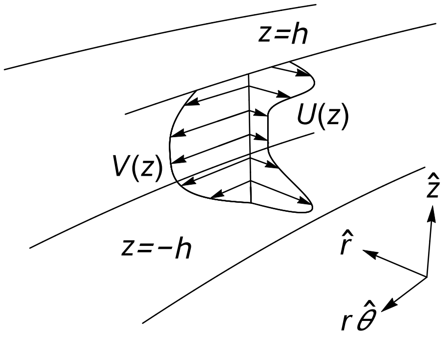

Figure 3.1: Parallel base flow schematic and local system of coordinates.

Using the local base flow $(U(z), V(z), 0)^T$ and the parallel flow approximation yields the following system of equations

$$\frac{\partial u}{\partial r} + \frac{1}{r}\frac{\partial v}{\partial \theta} + \frac{\partial w}{\partial z} = 0, \quad (3.3a)$$

$$\frac{\partial u}{\partial t} + U\frac{\partial u}{\partial r} + \frac{V}{r}\frac{\partial u}{\partial \theta} + wU' = -\frac{\partial p}{\partial r} + \frac{1}{Re}\nabla^2 u + f_u, \quad (3.3b)$$

$$\frac{\partial v}{\partial t} + U\frac{\partial v}{\partial r} + \frac{V}{r}\frac{\partial v}{\partial \theta} + wV' = -\frac{1}{r}\frac{\partial p}{\partial \theta} + \frac{1}{Re}\nabla^2 v + f_v, \quad (3.3c)$$

$$\frac{\partial w}{\partial t}+U\frac{\partial w}{\partial r}+\frac{V}{r}\frac{\partial w}{\partial \theta}=-\frac{\partial p}{\partial z}+\frac{1}{Re}\nabla^2 w+f_w, \tag{3.3d}$$

$$\frac{\partial \tau}{\partial t}+U\frac{\partial \tau}{\partial r}+\frac{V}{r}\frac{\partial \tau}{\partial \theta}+wT'=\frac{1}{RePr}\nabla^2 \tau+f_\tau, \tag{3.3e}$$

where $'$ denotes differentiation of the base flow with respect to to z, and ∇^2 stands for $\frac{\partial^2}{\partial r^2}+\frac{1}{r^2}\frac{\partial^2}{\partial \theta^2}+\frac{\partial^2}{\partial z^2}$, which is the Cartesian Laplace operator in the local coordinates $(\hat{\mathbf{r}}, r\hat{\boldsymbol{\theta}}, \hat{\mathbf{z}})$. The temporal evolution problem for the perturbations is completed with appropriate initial conditions, and the boundary conditions i.e., $u=v=w=\tau=0$ at $z=\pm 1$. Equations (3.3) have coefficients that do not depend on r and θ, this allows for the perturbation variables to be expanded as Fourier modes in these directions $\mathbf{u}(r,\theta,z,t)=\hat{\mathbf{u}}(z,t)\ \mathrm{e}^{\mathrm{i}(\alpha r+m\theta)}$, where α is the radial wavenumber, and m is the integer azimuthal wavenumber. Identical expansions are carried out for the perturbation pressure, perturbation temperature, and external forcing terms. Governing equations are simplified to

$$\mathrm{i}\alpha\hat{u}+\mathrm{i}\beta\hat{v}+\mathcal{D}\hat{w}=0, \tag{3.4a}$$

$$\frac{\partial \hat{u}}{\partial t}+\mathrm{i}\left(\alpha U+\beta V\right)\hat{u}+U'\hat{w}=-\mathrm{i}\alpha\hat{p}+\frac{1}{Re}\left(\mathcal{D}^2-k^2\right)\hat{u}+\hat{f}_u, \tag{3.4b}$$

$$\frac{\partial \hat{v}}{\partial t}+\mathrm{i}\left(\alpha U+\beta V\right)\hat{v}+V'\hat{w}=-\mathrm{i}\beta\hat{p}+\frac{1}{Re}\left(\mathcal{D}^2-k^2\right)\hat{v}+\hat{f}_v, \tag{3.4c}$$

$$\frac{\partial \hat{w}}{\partial t}+\mathrm{i}\left(\alpha U+\beta V\right)\hat{w}=-\mathcal{D}\hat{p}+\frac{1}{Re}\left(\mathcal{D}^2-k^2\right)\hat{w}+\hat{f}_w, \tag{3.4d}$$

$$\frac{\partial \hat{\tau}}{\partial t}+\mathrm{i}\left(\alpha U+\beta V\right)\hat{\tau}+T'\hat{w}=\frac{1}{RePr}\left(\mathcal{D}^2-k^2\right)\hat{\tau}+\hat{f}_\tau, \tag{3.4e}$$

where $\beta=m/r$, the total wavenumber is $k=(\alpha^2+\beta^2)^{\frac{1}{2}}$, and $\mathcal{D}$ denotes differentiation with respect to z of the perturbation variables. A more compact formulation is obtained by rewriting the system in terms of the normal vorticity $\hat{\eta}$ and the normal velocity $\hat{w}$ instead of the primitive variables. To do this, we first derive the transport equation for $\hat{\eta}$ by taking the z component of the curl of the momentum Eqs. (3.4b)–(3.4d). Secondly, we obtain an expression for the pressure by taking the divergence of the momentum Eqs. (3.4b)–(3.4d) and using the continuity Eq. (3.4a). The resulting expression is substituted into Eq. (3.4d) to eliminate $\hat{p}$ from the system

$$\mathcal{M}\frac{\partial \hat{w}}{\partial t}=-\mathrm{i}\mathcal{M}\left(\alpha U+\beta V\right)\hat{w}-\mathrm{i}\left(\alpha U''+\beta V''\right)\hat{w}-\frac{1}{Re}\mathcal{M}^2\hat{w}+\mathrm{i}\alpha\mathcal{D}\hat{f}_u+\mathrm{i}\beta\mathcal{D}\hat{f}_v+k^2\hat{f}_w, \tag{3.5a}$$

$$\frac{\partial \hat{\eta}}{\partial t}=-\mathrm{i}\left(\alpha U+\beta V\right)\hat{\eta}-\frac{1}{Re}\mathcal{M}\hat{\eta}+\mathrm{i}\left(\alpha V'-\beta U'\right)\hat{w}+\mathrm{i}\beta\hat{f}_u-\mathrm{i}\alpha\hat{f}_v, \tag{3.5b}$$

$$\frac{\partial \hat{\tau}}{\partial t}=-\mathrm{i}\left(\alpha U+\beta V\right)\hat{\tau}-\frac{1}{RePr}\mathcal{M}\hat{\tau}-T'\hat{w}+\hat{f}_\tau, \tag{3.5c}$$

where $\mathcal{M}=(k^2-\mathcal{D}^2)$. The boundary conditions for the normal vorticity, normal velocity, and temperature become $\mathcal{D}\hat{w}(\pm 1)=\hat{w}(\pm 1)=\hat{\eta}(\pm 1)=\hat{\tau}(\pm 1)=0$. Equations (3.5) are discretized using the Chebyshev collocation method and the operator $\mathcal{D}$ is replaced with the Chebyshev differentiation matrix $\mathbf{D}$. We obtain a linear dynamical system where the state variables are the normal velocity, normal vorticity, and temperature evaluated at the collocation points. The matrix representation of the system is

$$\frac{\mathrm{d}}{\mathrm{d}t}\begin{bmatrix}\hat{w}\\ \hat{\eta}\\ \hat{\tau}\end{bmatrix} = \underbrace{\begin{bmatrix}\mathbf{L_{OS}} & 0 & 0\\ \mathbf{L_{C1}} & \mathbf{L_{SQ}} & 0\\ \mathbf{L_{C2}} & 0 & \mathbf{L_{H}}\end{bmatrix}}_{\mathbf{L}}\begin{bmatrix}\hat{w}\\ \hat{\eta}\\ \hat{\tau}\end{bmatrix} + \underbrace{\begin{bmatrix}\mathrm{i}\alpha\mathbf{M}^{-1}\mathbf{D} & \mathrm{i}\beta\mathbf{M}^{-1}\mathbf{D} & \mathbf{M}^{-1}k^2 & 0\\ \mathrm{i}\beta & -\mathrm{i}\alpha & 0 & 0\\ 0 & 0 & 0 & 1\end{bmatrix}}_{\mathbf{B}}\begin{bmatrix}\hat{f}_u\\ \hat{f}_v\\ \hat{f}_w\\ \hat{f}_\tau\end{bmatrix}, \tag{3.6}$$

where $\mathbf{M}$ is the discretized representation of $\mathcal{M}$, and $\mathbf{L_{OS}}$, $\mathbf{L_{SQ}}$, and $\mathbf{L_{C1}}$ are the familiar Orr-Sommerfeld, Squire, and coupling operators for a base flow that has velocity components along both, the spanwise and streamwise directions. The matrix denoted as $\mathbf{L_H}$ corresponds to the linearized heat equation operator, and $\mathbf{L_{C2}}$ is the coupling term with the normal velocity perturbation. The rate of change of the state vector $\hat{\mathbf{q}} = (\hat{w}, \hat{\eta}, \hat{\tau})^T$ is related to its current state by operator $\mathbf{L}$, and to the input forcing $\hat{\mathbf{f}} = (\hat{f}_u, \hat{f}_v, \hat{f}_w, \hat{f}_\tau)^T$ by operator $\mathbf{B}$. The system can be written in compact notation as follows

$$\frac{\mathrm{d}\hat{\mathbf{q}}}{\mathrm{d}t} = \mathbf{L}\hat{\mathbf{q}} + \mathbf{B}\hat{\mathbf{f}}, \tag{3.7a}$$

$$\hat{\mathbf{y}} = \mathbf{C}\hat{\mathbf{q}}, \tag{3.7b}$$

where $\hat{\mathbf{y}}$ is a an observation of the state $\hat{\mathbf{q}}$ through the linear mapping $\mathbf{C}$. Equation (3.7) governs the dynamics of the perturbation variables for a generalized forcing and a linear observable function. In particular, we are interested in two particular cases: the temporal evolution of initial disturbances and the long-time response to external harmonic forcing.

3.2 Choice of measure

An important question we still need to answer is what measure should we use to quantify the size of disturbances. In order to measure the velocity and temperature perturbations we need to define an energy norm $||\cdot||_E$. A physically relevant choice to measure velocity perturbations is the kinetic energy [89], and for the temperature perturbations we use the standard (Euclidean) L_2-norm, as it measures the deviation from the steady state temperature field. Hence, for a state vector $\hat{\mathbf{x}} = (\hat{u}, \hat{v}, \hat{w}, \hat{\tau})^T$, the following energy norm is defined

$$||\hat{\mathbf{x}}||_E^2 = \int_{-1}^{1}\left[\frac{1}{2}\left(|\hat{u}|^2 + |\hat{v}|^2 + |\hat{w}|^2\right) + |\hat{\tau}|^2\right]\mathrm{d}z = \hat{\mathbf{x}}^H\mathbf{Q}\hat{\mathbf{x}}, \tag{3.8}$$

where $\mathbf{Q}$ is the energy weight matrix that contains the appropriate weighting of the variables at the collocation points, as well as the integration weights between the channel walls. A Cholesky decomposition of $\mathbf{Q} = \mathbf{F}^H\mathbf{F}$ allows us to relate this norm to an equivalent standard (Euclidean) L_2-norm $||\hat{\mathbf{x}}||_E = ||\mathbf{F}\hat{\mathbf{x}}||_2$. The energy norm of a matrix $\mathbf{A}$ is easily derived using the definition of a vector-induced norm

$$||\mathbf{A}||_E = \max_{\hat{\mathbf{x}}\neq 0}\frac{||\mathbf{A}\hat{\mathbf{x}}|_E}{||\hat{\mathbf{x}}||_E} = \max_{\hat{\mathbf{x}}\neq 0}\frac{||\mathbf{F}\mathbf{A}\mathbf{F}^{-1}\mathbf{F}\hat{\mathbf{x}}||_2}{||\mathbf{F}\hat{\mathbf{x}}||_2} = ||\mathbf{F}\mathbf{A}\mathbf{F}^{-1}||_2 = \sigma_{max}(\mathbf{F}\mathbf{A}\mathbf{F}^{-1}), \tag{3.9}$$

where σ_{max} is the largest singular value of the matrix.

3.3 Growth of initial disturbances

For a given initial condition $\hat{\mathbf{q}}(0) = \hat{\mathbf{q}}_0$, the solution to Eqs. (3.7) without any external forcing is given by

$$\hat{\mathbf{q}} = \exp(t\mathbf{L})\hat{\mathbf{q}}_0. \tag{3.10}$$

In order to study the stability of the system, we calculate the maximum energy amplification over a specified time interval and optimized over all initial conditions

$$G(t) = \max_{\hat{\mathbf{q}}_0 \neq 0} \frac{||\hat{\mathbf{q}}(t)||_E^2}{||\hat{\mathbf{q}}_0||_E^2} = \max_{\hat{\mathbf{q}}_0 \neq 0} \frac{||\exp(t\mathbf{L})\hat{\mathbf{q}}_0||_E^2}{||\hat{\mathbf{q}}_0||_E^2} = ||\exp(t\mathbf{L})||_E^2, \tag{3.11}$$

The flow is asymptotically unstable when $G(t) \to \infty$ as $t \to \infty$, which will occur when at least one eigenvalue of $\mathbf{L}$ has a positive real part. On the counterpart, the flow is called asymptotically stable when $G(t) \to 0$ as $t \to \infty$. Nevertheless, for eigenvalues with negative real part, the flow may experience a large amplification due to linear transient growth before decaying asymptotically, which occurs in the case of nonnormal eigenvectors [79, 90].

3.4 Response to componentwise external harmonic forcing

For an external harmonic forcing $\hat{\mathbf{f}}(t) = \tilde{\mathbf{f}} \exp(\mathrm{i}\omega t)$, the particular solution to Eqs. (3.7) is given by

$$\hat{\mathbf{y}} = \mathbf{C}\,(\mathrm{i}\omega\mathbf{I} - \mathbf{L})^{-1}\mathbf{B}\hat{\mathbf{f}}. \tag{3.12}$$

For an asymptotically stable flow, this solution represents the long-term response of the system. The operator $\mathbf{H}(\alpha, \beta, \omega) = \mathbf{C}\,(\mathrm{i}\omega\mathbf{I} - \mathbf{L})^{-1}\mathbf{B}$ is closely related to the concept of the transfer function of a linear time-invariant system, so that $\hat{\mathbf{y}} = \mathbf{H}(\alpha, \beta, \omega)\hat{\mathbf{f}}$. Hence, this operator maps the input forcing $\hat{\mathbf{f}}$ to the observable $\hat{\mathbf{y}}$, and it is a function of the forcing frequency ω and the wavenumbers α and β.

In order to study the receptivity of the system, we calculate the maximum energy amplification of the output with respect to the input, optimized over all shapes of the input forcing

$$\mathcal{R}(\alpha, \beta, \omega) = \max_{\hat{\mathbf{f}} \neq 0} \frac{||\hat{\mathbf{y}}||_E}{||\hat{\mathbf{f}}||_E} = \max_{\hat{\mathbf{f}} \neq 0} \frac{||\mathbf{H}(\alpha, \beta, \omega)\hat{\mathbf{f}}||_E}{||\hat{\mathbf{f}}||_E} = ||\mathbf{H}(\alpha, \beta, \omega)||_E. \tag{3.13}$$

Hence, the response of the system is measured as the energy norm of the transfer function. The response maximized over all temporal frequencies is known in literature as the $\mathcal{H}_\infty$-norm and can be interpreted as the worst case amplification of deterministic inputs [91].

$$||\mathbf{H}||_{\mathcal{H}_\infty}(\alpha, \beta) = \max_{\omega} \mathcal{R}(\alpha, \beta, \omega). \tag{3.14}$$

Equation (3.14) shows how we calculate the $\mathcal{H}_\infty$-norm. We define the componentwise transfer function, $\mathbf{H}_{xs}(\alpha, \beta, \omega)$, as the mapping from the x-component of the forcing $\hat{\mathbf{f}}$ to the s-component of the observable $\hat{\mathbf{y}}$, and it is obtained by zeroing out the corresponding columns of $\mathbf{B}$ and rows of $\mathbf{C}$. In this work we are interested in the response of the disturbance temperature τ to an external forcing in each of the momentum components, i.e., we want to measure $\mathbf{H}_{u\tau}$, $\mathbf{H}_{v\tau}$ and $\mathbf{H}_{w\tau}$.

$$\mathcal{R}_{xs}(\alpha, \beta, \omega) = ||\mathbf{H}_{xs}(\alpha, \beta, \omega)||_E, \tag{3.15}$$

$$||\mathbf{H}_{xs}||_{\mathcal{H}_\infty}(\alpha, \beta) = \max_{\omega} \mathcal{R}_{xs}(\alpha, \beta, \omega). \tag{3.16}$$

As shown in Eqs. (3.15) and (3.16), the componentwise response is defined as the energy norm of the componentwise transfer function, and the $\mathcal{H}_\infty$-norm is obtained by maximizing over all temporal frequencies.

3.5 Modal decomposition and order reduction

This section presents the methods employed to carry out the nonmodal stability and receptivity analyses. Before we can compute the optimal growth G, optimal response $\mathcal{R}$, and componentwise response $\mathcal{R}_{xs}$ from Eqs. (3.11),(3.13) and (3.15) respectively, we have to perform a modal decomposition of the dynamics operator $\mathbf{L} = \mathbf{V}\mathbf{\Lambda}\mathbf{V}^{-1}$. Here, $\mathbf{V}$ is the matrix whose columns are the eigenvectors of $\mathbf{L}$, and $\mathbf{\Lambda}$ is a diagonal matrix containing its eigenvalues. This way, the time evolution operator and the resolvent operator in Eqs. (3.11) and (3.12), respectively, are obtained as follows

$$\exp(t\mathbf{L}) = \mathbf{V}\exp(t\mathbf{\Lambda})\mathbf{V}^{-1}, \qquad \mathbf{C}\,(\mathrm{i}\omega\mathbf{I} - \mathbf{L})^{-1}\mathbf{B} = \mathbf{C}\mathbf{V}\,(\mathrm{i}\omega\mathbf{I} - \mathbf{\Lambda})^{-1}\mathbf{V}^{-1}\mathbf{B}.$$

Using the above expressions, the optimal growth optimal growth G, optimal response $\mathcal{R}$, and componentwise response $\mathcal{R}_{xs}$ can be easily computed, since now we are only required to calculate the exponential and the inverse of diagonal matrices instead full ones.

Using N Chebyshev collocation points, the length of the state vector $\hat{\mathbf{q}} = (\hat{w}, \hat{\eta}, \hat{\tau})^T$ is $3N - 6$ (since it does not include the domain boundaries), and therefore computing the eigenvalues and eigenfunctions requires $O((3N-6)^3)$ arithmetic operations. To reduce the amount of computational work, we restrict our attention to the K least stable modes instead of all $3N - 6$, thus requiring only $O(K^3)$ operations [77, 80]. This order reduction technique is known as modal truncation [92, 93]. All numerical algebra was carried out using the commercial software *Wolfram Mathematica 10.3.*

Chapter 4

Experimental methodology

As a complement to the theoretical and numerical work presented, experiments are carried out with two specific goals: to determine the onset of hydrodynamic instabilities in the swirl flow channel, and to provide proof of concept of the performance enhancement in the heat sink using a receptivity based strategy. To accomplish the first of these objectives, a flow visualization experiment is designed, where colored water is injected to the channel for a range of flow rates and streaklines are photographed. Observation of the diffusion patterns in the flow and their change with the Reynolds number provide a qualitative comparison to results from the linear stability analysis. To accomplish the second goal, a performance measurement experiment is designed, where the surface temperature and pressure drop in the heat sink are measured at different flow rates and an imposed constant heat flux. This allows an assessment of the validity of the numerical base flow results, and to study the influence of receptivity based heat transfer enhancement strategies. In particular, the effect of flow pulsations on the device performance is studied for the range of forcing frequencies obtained from the componentwise receptivity analysis. This chapter describes the manufacturing of the swirl flow channel heat sinks built for each experiment, the equipment and instrumentation used, the testing procedure, and how the experimental calculations were performed.

4.1 Device fabrication

Different swirl flow channel heat sinks are fabricated for each experiment. For the flow visualization experiments the device consists of two parts: A body made from Technyl® thermoplastic, where the channel was manufactured using a CNC router and conventional lathe and mill techniques; and a transparent acrylic cover. Inlet and outlet ports were machined in the body, as well as two small ports designed for the injection of colored water. The device fabricated for the flow visualization experiment is shown in Fig. 4.1.

For the performance measurement experiment, the heat sink also consists of two parts: a thermally insulating body made from nylon thermoplastic, where the channel was manufactured using conventional lathe and mill techniques; and a thermally conductive cover made from a 6061 aluminum sheet used as the heat exchange surface. Inlet and outlet ports were

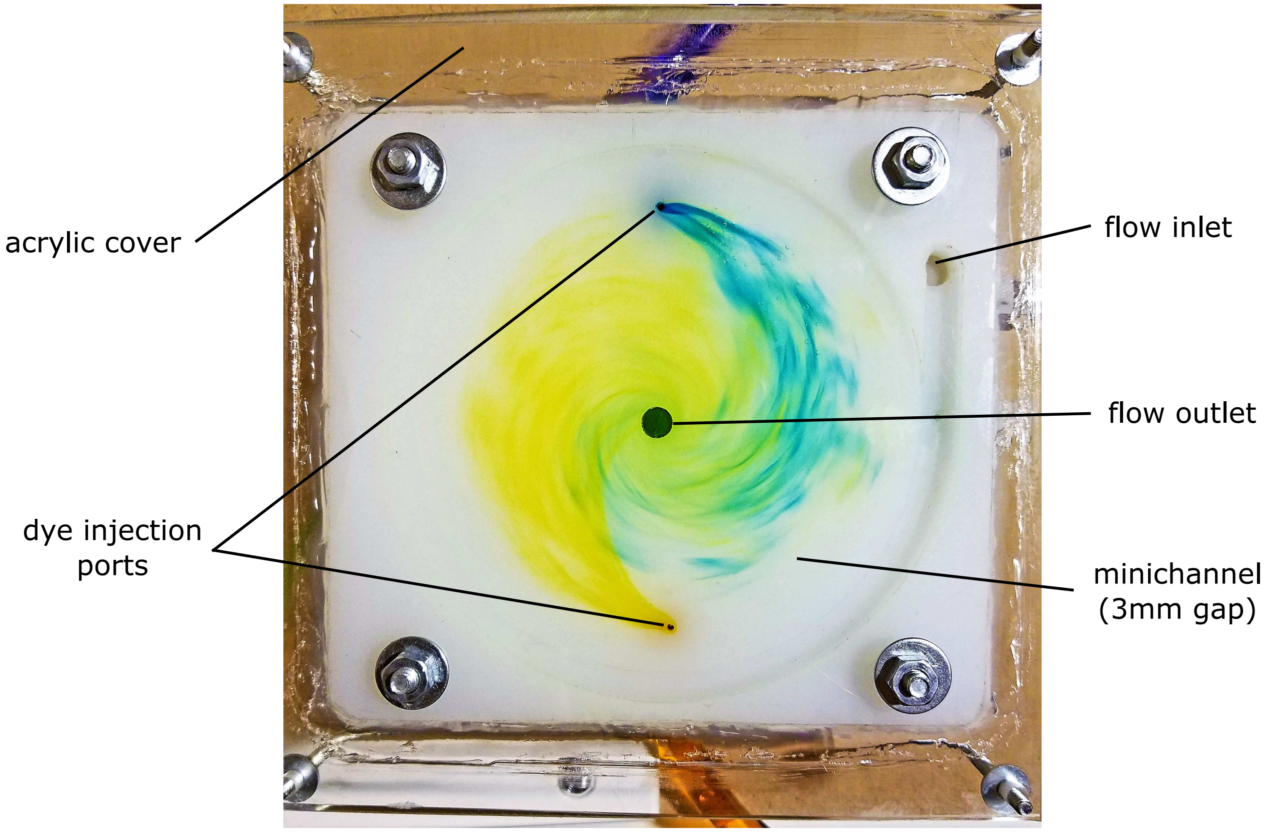

Figure 4.1: Swirl flow channel fabricated for the flow visualization experiment.

machined in the body, as well as a feeder channel, holes for screws and a groove for the o-ring used to seal the two pieces. The feeder channel is 12.7mm deep and 3.18mm wide, and is designed to get a flow inlet angle $\theta = 4°$. A disassembled view of this device is shown in Fig. 4.2, and the fabrication schematics can be found on Appendix B.

The most important design dimensions are preserved for the two swirl flow minichannel heat sinks fabricated, and are shown in Table 4.1.

Table 4.1: Dimensions of the fabricated swirl flow minichannel heat sinks.

$2h$	r_o	r_i	θ_0
3mm	50mm	3.18mm	4°

4.2 Experimental equipment and instrumentation

For both experiments water is pumped from a reservoir and through a Vinyl tubing using a Cole-Parmer® gear pump. A needle valve and an in-line flowmeter (both Cole-Parmer®) are used to regulate and to measure the flow rate.

For the flow visualization experiment, an open loop configuration is used. Water with food

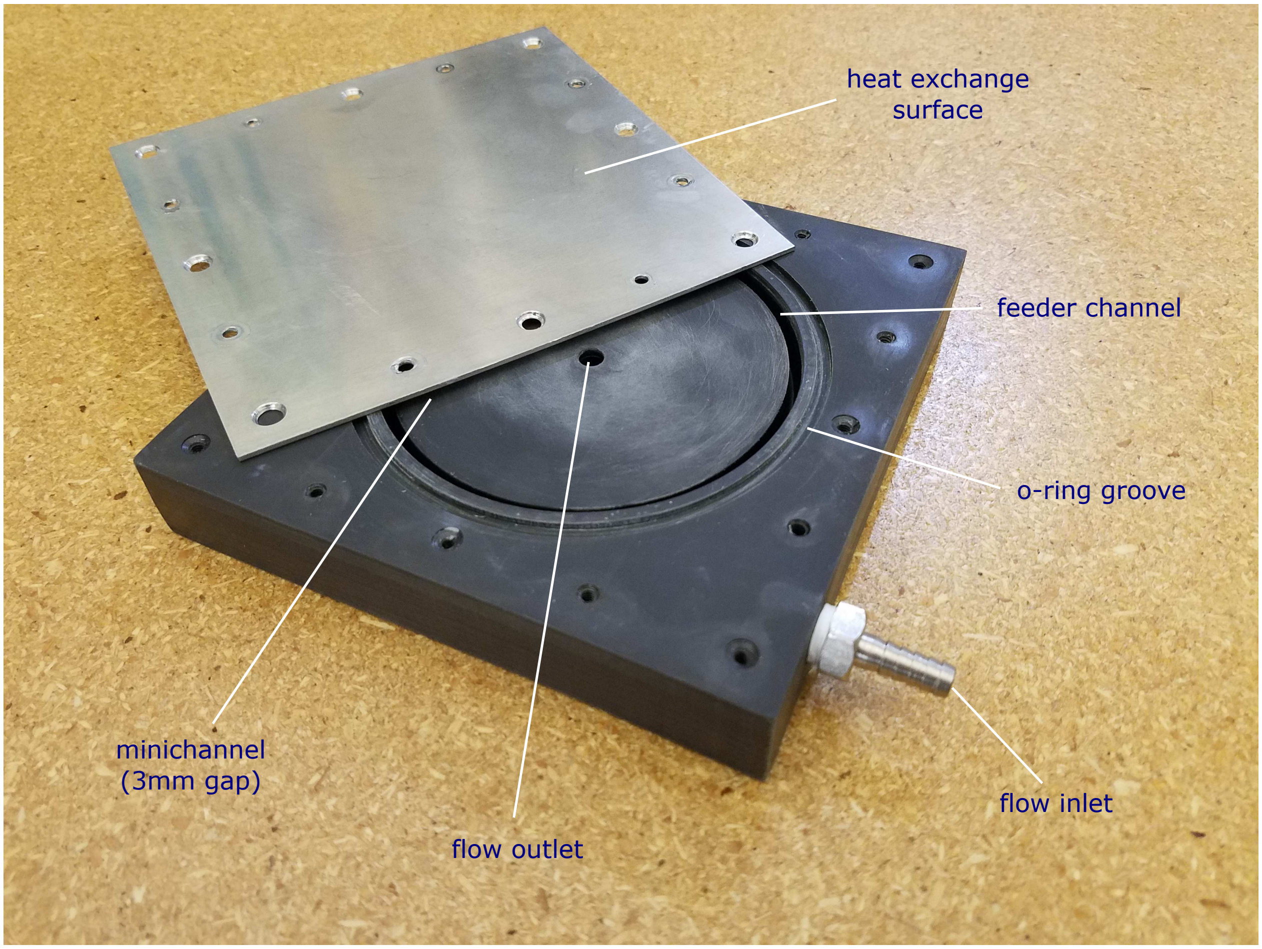

Figure 4.2: Heat sink fabricated for the performance measurement experiment.

colorant is injected to the channel through the injection ports using a KD Scientific syringe pump. Streaklines and diffusion patterns are photographed at different flow rates using a 3840 × 2160pixels resolution camera with a stand. Figure 4.3 shows the main components of the setup for the flow visualization experiment.

For the performance measurement experiment, a closed loop configuration is used. An Omega$^{\text{TM}}$ ultra-thin heat sheet with an output of 250W is attached to the aluminum cover of the minichannel to act as a heat source. Hot water leaving the heat sink goes through a finned coil heat exchanger, there heat is rejected to the ambient air via forced convection using fans, water cools down and then it returns to the reservoir. A pulsating flow generator was built to superimpose a pulsating flow rate over the mean flow provided by the gear pump. The mechanism of this actuator consists in periodically squeezing the Vinyl tubing before the inlet of the heat sink, and this is achieved using a 200rpm and 12VDC motor to drive a wheel that has rods attached to it. These rods are parallel to the axis of the wheel but are eccentric, therefore pressing and releasing the tubing on every rotation cycle. Figure 4.4 shows the main components of the experimental setup and the wheels with different number of rods that are used to generate pulsations at different frequencies.

The pressure drop in the minichannel is measured using two Cole-Parmer® high-accuracy

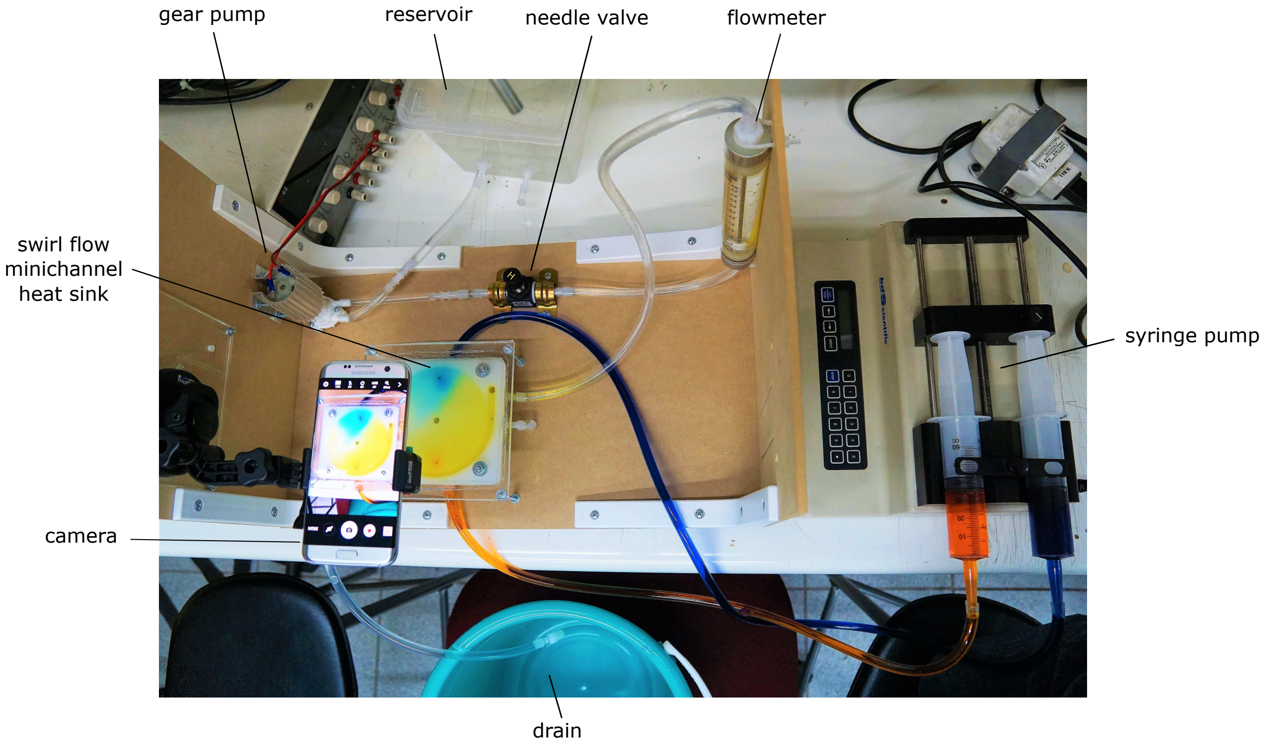

Figure 4.3: Setup for the flow visualization experiment.

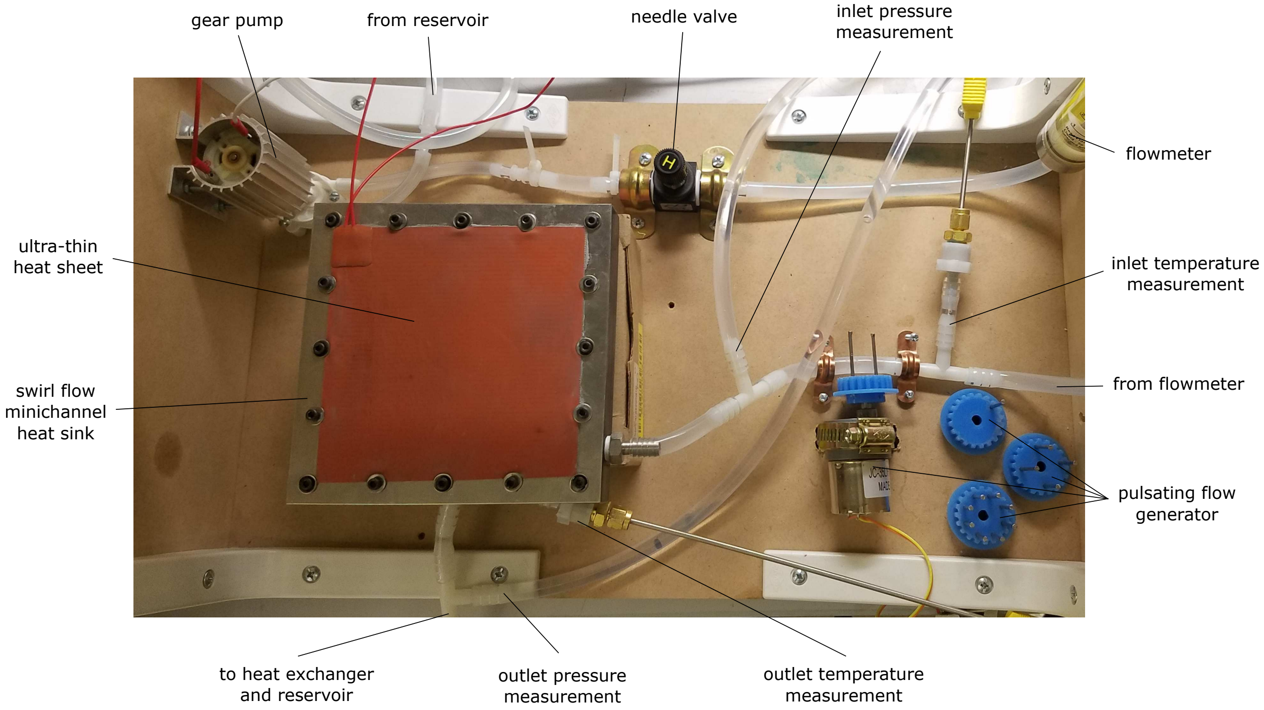

Figure 4.4: Setup for the performance measurement experiment.

pressure transducers and the inlet and outlet flow temperatures are measured using K-type thermocouples. National Instruments$^{\mathrm{TM}}$ data acquistion systems (DAQs) along with the software *NI Labview 2015* were used for both, pressure and flow temperature measurements.

The *NI Labview* code is shown in Appendix C. In order to estimate the inside wall temperature in the minichannel, we measure temperature at the center of the exposed side of the ultra-thin heat sheet using a Flir$^{\text{TM}}$ spot thermal camera with a tripod. The range and accuracy of the instrumentation used for the experiments are shown in Table 4.2, this excludes the range and resolution of the DAQs which was taken into account in the uncertainty analysis.

Table 4.2: Instrumentation range and accuracy.

Measurement	Device range	Accuracy
Flow rate	0.4–4 l/min	5%
Pressure	0–345kPa	0.86kPa
Flow temperature	−200–1250°C	Greater of 1.1°C or 0.4%
Surface temperature	−25–380°C	Greater of 1.5°C or 1.5%

4.3 Testing procedure

For the flow visualization experiment, streaklines were photographed at 600, 800, 1000, 1200, and 1400ml/min ($Re_o = 0.57,\ 0.76,\ 0.95,\ 1.14$, and 1.33). The procedure started by turning on the gear pump and opening the valve to get 1400ml/min, then the syringe pump was set to 0.4ml/min and turned on to inject the colored water. A photograph was taken after an interval 20s, which was enough for the system to reach a steady or periodic state. The flow rate was lowered and the process repeated. Qualitative agreement is found between three series of photographs.

For the performance measurement experiment, inlet and outlet flow temperatures, surface temperature, and pressure drop in the minichannel were registered simultaneously for a range of flow rates with and without pulsations at different frequencies. The procedure started by turning on the pump and heater and letting the system run for 25min, until the closed loop reached a thermal steady state. Throughout the testing, room temperature was maintained between 20 and 22°C. Pressure drop and flow temperatures were recorded over a period of 5s, and the surface temperature reading was annotated. The flow rate was lowered and new measurements were taken after the temperature fluctuations were smaller than 0.5°C/min. Once the minimum flow rate was reached, the needle valve was fully opened again, and the procedure was repeated with the pulsating flow generator turned on, and for each of the of four different wheels that give different pulsating frequencies. Therefore, the data set is composed of measurements at 17 different flow rates for each of the 6 pulsating frequencies (including no pulsations). Results presented in this article are the average of three series of data sets.

4.4 Experimental calculations

No experimental calculations were required for the flow visualization experiment. For the performance measurement experiment, for each flow rate and pulsating frequency, the pumping power $\dot{\mathcal{W}}$, the average wall heat flux q''_w, the wall temperature at the inside of the minichannel T_w, and the Nusselt number Nu were calculated as follows

$$\dot{\mathcal{W}} = \dot{V}\Delta p, \tag{4.1}$$

$$q''_w = \frac{\rho C_p \dot{V}\left(T_{out} - T_{\mathrm{in}}\right)}{\pi\left(r_o^2 - r_{\mathrm{i}}^2\right)}, \tag{4.2}$$

$$T_w = T_{top} - \frac{q''_w}{R_{th}}, \tag{4.3}$$

$$Nu = \frac{q''_w \mathrm{d}_h}{\kappa(T_w - T_{av})}, \tag{4.4}$$

where $\dot{V}$ is the volume flow rate, Δp is the root mean square (RMS) of the total pressure drop signal, r_{i} and r_o are the inner and outer radius respectively, T_{in}, T_{out} and T_{av} correspond to the flow temperatures measured at the inlet of the channel, at the outlet, and the average between both, T_{top} is the surface temperature measured from the outside, R_{th} is the conductive thermal resistance of the aluminum cover, d_h is the hydraulic diameter taken as twice the channel height, and C_p and κ are the heat capacity and thermal conductivity of water, respectively.

Uncertainty of the measured quantities is calculated using the instrumentation information shown in Table 4.2, as well as the range and resolution of the data acquisition systems. Systematic uncertainty of the flow temperature difference $T_{out} - T_{\mathrm{in}}$ is eliminated by zeroing the measurement of both thermocouples using the same reference. Uncertainty is propagated from the measurements to the calculated variables q''_w, T_w and Nu using the Taylor series method.

$$\mathrm{e}^2_{f(x_1,\ldots,x_n)} = \sum_{\mathrm{i}=1}^{n}\left(\frac{\mathrm{d}f}{\mathrm{d}x_{\mathrm{i}}}\mathrm{e}_{x_{\mathrm{i}}}\right)^2. \tag{4.5}$$

Equation 4.5 shows how we compute the uncertainty e_f for a calculated variable f which depends on measurements $x_1, \ldots, x_n$, each with uncertainty $\mathrm{e}_{x_{\mathrm{i}}}$.

Chapter 5

Results for steady state flow

The steady state flow in the swirl flow channel heat sink is calulated using the integral method for the velocity field, and spatial discretization followed by matrix inversion for the temperature field, as presented in Chapter 2. The base configuration of interest in this chapter is presented in Fig. 5.1.

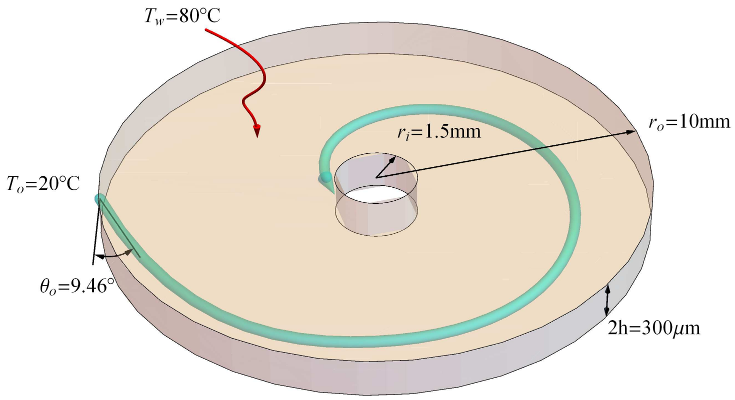

Figure 5.1: Base configuration used for numerical simulations of the steady state flow.

First, the structure of hydrodynamic boundary layers is investigated and the influence of the flow rate Reynolds number and the flow inlet angle over the flow patterns is analyzed. The effects of varying the channel height, the flow inlet angle, and the Prandtl number on the heat sink performance are investigated. For the Prandtl number variation, heat sink performance using water is compared to that of using a 2vol% and a 4vol% water-Cu nanofluid. We compare the benefits of changing to a nanofluid to the performance increase obtained with geometric design variations. Design recommendations are discussed in terms of the boundary layer structures and their consequences on the thermohydraulic performance of the swirl flow channel heat sink.

5.1 Validation of numerical results

Ruiz and Carey fabricated a swirl flow channel heat sink prototype and carried out experimental measurements of the device performance [15]. Distilled water was used as the operating fluid, and volumetric flow rates up to 387ml/min were used. Important heat sink design parameters used by these authors are shown in Table 5.1.

Table 5.1: Design parameters for the experimental device of Ruiz and Carey [15].

θ_o	$2h$	r_o	r_{i}	T_o
9.46^o	300μm	1cm	0.15cm	20^oC

Parameters shown in Table 5.1, corresponding to the experimental device from Ruiz and Carey in Ref. [15], are taken as the base case design for the analysis in Section 5.4. Numerical solutions for the steady state velocity and temperature fields in the swirl flow channel heat sink are obtained using the methods presented in Chapter 2. Subsequently, the total pressure drop, Δp, and the average wall heat flux, q''_w are calculated. For the present analysis, a constant temperature boundary condition is preferred because we are interested in the heat rate that can be obtained with a device designed to keep the wall temperature under $T_w = 80^o$C, which is a common requirement for applications such as thermal management of electronics [6, 14]. Experimental curves for the total pressure drop and the average wall heat flux as a function of volume flow rate $\dot{V}$, with an average wall temperature of 80^oC, are extracted from the results in Ref. [15]. A comparison between the performance curves obtained experimentally and those obtained numerically is presented in Fig. 5.2.

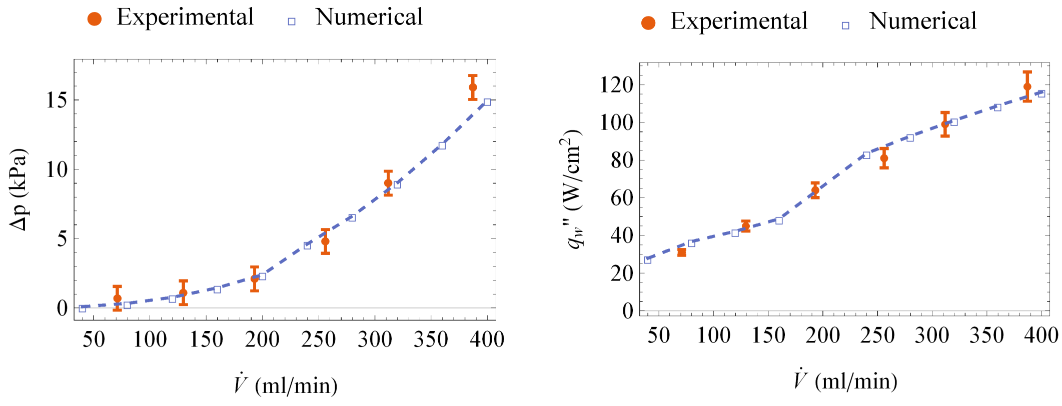

(a) (b)

Figure 5.2: Comparison of numerical performance curves to experimental ones from Ruiz and Carey in Ref. [15]. (a) Pressure drop vs flow rate, including entry and exit effects. (b) Average wall heat flux vs flow rate.

For consistency with the experimental device, numerical values for the total pressure drop shown in Fig. 5.2 include additional energy losses from entry and exit effects. Specifically, a sudden contraction and sudden expansion are considered at the flow inlet and outlet respectively, as well as a 90^o turn in both of these regions [94]. As shown in Fig. 5.2, numerical results for both, Δp and q''_w, are in good agreement with the experimental results from Ref. [15].

5.2 Structure of hydrodynamic boundary layers

The flow model and integral method are used to calculate the phase-space regarding the structure of the hydrodynamic boundary layers in the flow. The flow rate Reynolds number, Re_o, was defined as

$$Re_o = \frac{u_o h^2}{\nu r_o} = \frac{\dot{m} h}{4\pi \nu r_o^2},$$

where $\dot{m}$ is the mass flow rate. The steady state flow is obtained for 800 combinations of Re_o and the inlet angle θ_o, ranging from 0.1 to 1000 and from 0.1^o to 90^o, respectively. As the fluid moves radially inward through the channel, depending on the nondimensional parameters, entraining boundary layers can merge, become non entraining or remain as entraining boundary layers. The structure of the boundary layers inside the channel is assessed by classifying the phenomena as follows:

I. Predominantly entraining: Boundary layers do not merge and remain as entraining boundary layers up to values of r smaller than 0.6 ($r^* < 0.6 r_o$).

II. Predominantly non entraining: Boundary layers do not merge and become non entraining for values of r larger than 0.6 ($r^* > 0.6 r_o$).

III. Predominantly merged: Boundary layers merge for values of r larger than 0.6 ($r^* > 0.6\ r_o$).

Using this classification, the steady state flow physics of the system is characterized on the θ_o–Re_o space, as shown in Fig. 5.3.

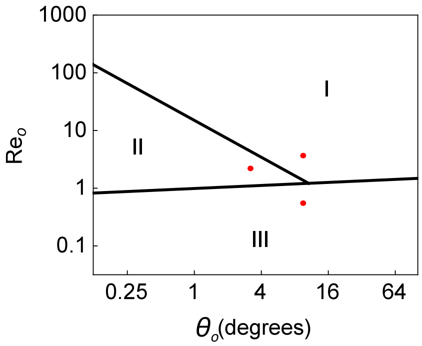

Figure 5.3: Classification of boundary layer structures on the θ_o–Re_o space. I: Predominantly entraining. II: Predominantly non entraining. III: Predominantly merged.

Figure. 5.3 shows that boundary layers merge under a certain value of Re_o which increases as θ_o increases. As the flow rate Reynolds number decreases, viscous shear stress becomes stronger than advection and as a consequence boundary layers become thick enough to merge. For $\theta_o < 14^o$ boundary layers are predominantly non entraining inside a band of Re_o that increases its width as θ_o decreases. The more tangentially the flow enters the channel, the stronger the crossflow induced by the momentum difference between rotating and near wall flows. This crossflow carries fluid inside the boundary layers radially inward and generates the entrainment of fluid from the core. Predominantly entraining boundary layers are found for large flow rate Reynolds numbers, where the crossflow is not strong enough to carry all the flow rate through the boundary layers.

5.3 Streamlines and temperature field

Temperature fields are solved to showcase the three different boundary layer structures described in the previous section. Combinations of the flow inlet angle and the Reynolds number used for each case are selected to represent different geometries and operating conditions. A fixed value is used for the Prandtl number, $Pr = 2.20$, as it only depends on the fluid properties. The selected θ_o and Re_o for each case are marked as dots in Fig. 5.3 and are shown in Table 5.2, these correspond to values used in the next section to explore the design of the swirl flow channel heat sink using water as the operating fluid.

Table 5.2: Nondimensional numbers and predominant boundary layer structures.

Case	θ_o	Re_o	Pr	Boundary layers
1	9.46^o	3.67	2.20	Entraining (I)
2	3.18^o	2.20	2.20	Non entraining (II)
3	9.46^o	0.55	2.20	Merged (III)

To visualize the velocity field in the $r-z$ plane, streamlines are calculated. Figure 5.4 shows the dimensionless temperature distribution, T, and streamlines in the $r-z$ plane for the three cases solved. Streamlines provide visualization of the evolution and transitions between the different boundary layer structures. In Fig. 5.4(c) streamlines are parallel to each other because boundary layers merge and radial velocity profiles become parabolic. Figure 5.4(a) shows entraining boundary layers, where the movement of fluid towards the walls is induced by the swirl difference between the flow in the core and the flow in the boundary layers. When the swirl is strong enough so that the induced crossflow carries all the flow rate that is passing through the channel, then non entraining boundary layers develop, as shown in Fig. 5.4(b), and the fluid in the core stays in a pure rotation state. A comparison between Fig. 5.4(b) and the flow visualization experiments carried out by Owen et al. in Ref. [85], identifies the source region observed by these authors as the entraining boundary layers found in this study. Experimental measurements of the velocity field should be carried out in order to make a quantitative comparison with the model.

From the contours of dimensionless temperature, a thermal boundary layer on the lower wall can be recognized. In Fig. 5.4(c) the development of the thermal boundary layer resembles that found in the flow between parallel plates. A thinner thermal boundary layer is found in Fig. 5.4(a), because a higher flow rate is concentrated near the walls due to the

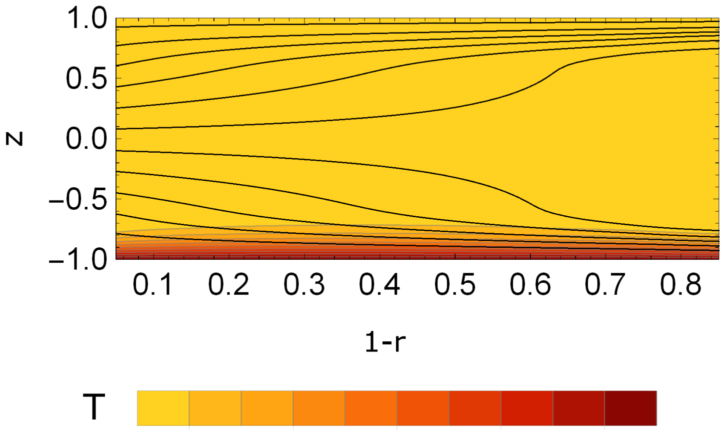

(a) Case 1: $\theta_o = 9.46°$, $Re_o = 3.67$, and $Pr = 2.20$.

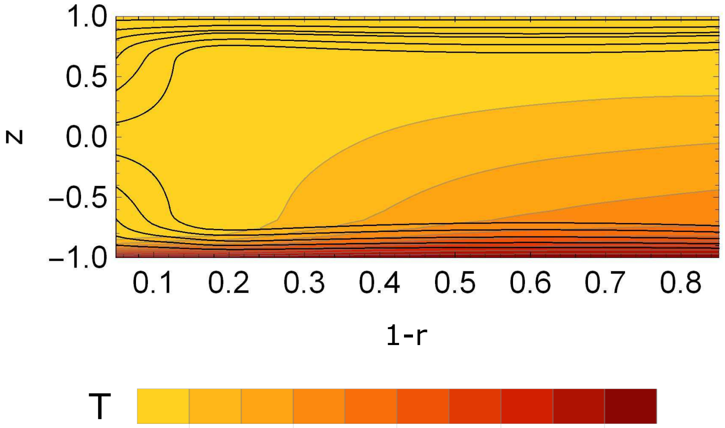

(b) Case 2: $\theta_o = 3.18°$, $Re_o = 2.20$, and $Pr = 2.20$.

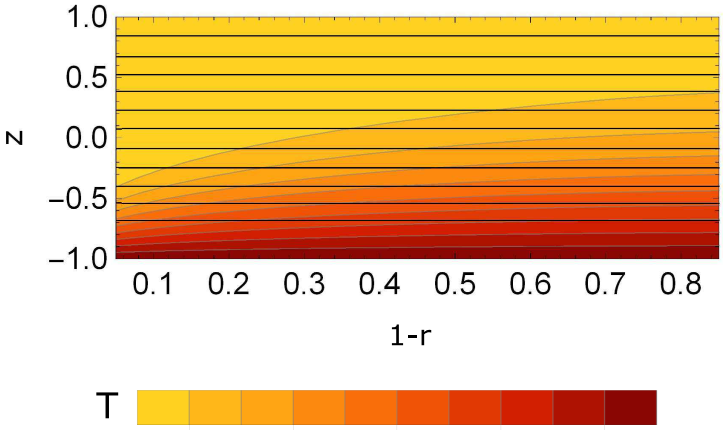

(c) Case 3: $\theta_o = 9.46°$, $Re_o = 0.55$, and $Pr = 2.20$.

Figure 5.4: Contours of dimensionless temperature T and streamlines in the r-z plane.

entrainment. An abrubt increase in the thickness of the thermal boundary layer is observed in Fig. 5.4(b), where the hydrodynamic boundary layers are non entraining. The influence of the higher wall temperature penetrates through the viscous boundary layer and reaches the inviscid core where no velocity gradients are present, therefore the heat transfer mechanism in the core is pure conduction.

Results show that entrainment effects will enhance heat transfer in the swirl flow channel heat sink, therefore θ_o and Re_o should be adjusted to manipulate the boundary layer structure. In order to take advantage of this effect, θ_o should be as small as possible, which means that the fluid should be admitted in the channel as tangent as possible. For a swirl flow channel heat sink of a certain radius, Re_o can be increased by increasing the flow rate or the channel height. Intuition suggests that the average wall heat flux will increase with the flow rate and decrease with the channel height, as in conventional microchannel heat sinks. Nonetheless, this may not be the case for the device studied here, as entrainment effects are present when increasing Re_o over a certain value. Heat transfer can also be enhanced by decreasing the Prandtl number, which can be done by changing to a working fluid with a higher thermal conductivity.

5.4 Design exploration

In this section, we consider a base case with the design parameters shown in Table 5.1, which correspond to the device studied experimentally by Ruiz and Carey in Ref. [15]. Starting from the base case, which uses water as the working fluid, we evaluate the effect of certain design variations on the total pressure drop and average wall heat flux through the device. In particular, the effect of the channel height, h, the effect of the flow inlet angle, θ_o, and the effect of the Prandtl number, Pr. All heat sink designs are required to maintain wall temperature at $T_w = 80^o$C, use an inlet temperature of $T_o = 20^o$C, and performance is investigated for volume flow rates up to $\dot{V} = \dot{V}_{\max} = 400$ml/min.

5.4.1 Effect of the channel height

The effect of the channel height on the performance of the swirl flow channel heat sink is investigated. For this purpose the total pressure drop, Δp, and the average wall heat flux, q''_w, are calculated for three designs with different channel heights $2h = 100\mu$m, 300μm and 500μm. Performance curves for flow rates up to $\dot{V}_{\max}$ are shown in Fig. 5.5.

When the flow rate increases, the total pressure drop through the heat sinks grows at an increasing rate, as shown in Fig. 5.5(a). It is observed that the smaller the height of the channel, the larger the pressure drop. This effect is due to the reduction in the flow passage area, and becomes more important as the flow rate increases. The average wall heat flux also grows with $\dot{V}$ but at a decreasing rate, as shown in Fig. 5.5(b). For $2h = 300\mu$m and 500μm, abrupt increments in q''_w are observed at given flow rates. This happens because, for these cases, hydrodynamic boundary layers merge at low $\dot{V}$ and become non

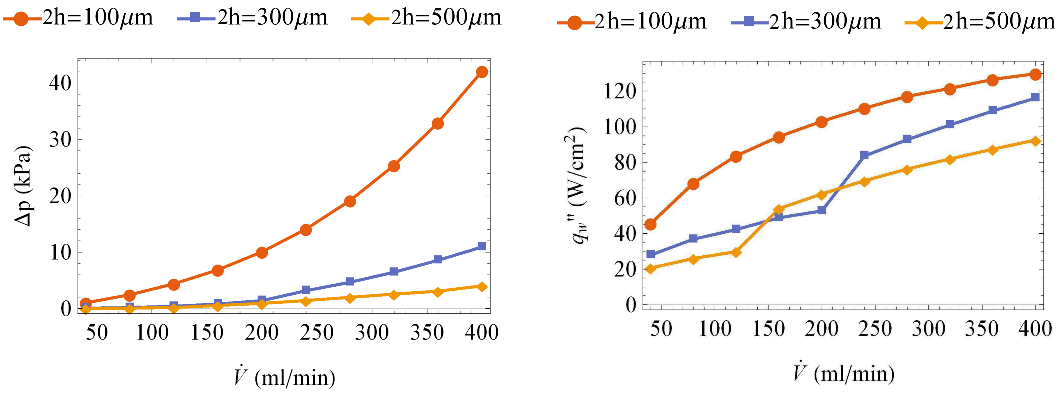

(a) (b)

Figure 5.5: Performance curves for channels of different heights. (a) Pressure drop vs flow rate. (b) Average wall heat flux vs flow rate.

entraining over a critical value of $\dot{V}$. For the design with $2h = 500\mu$m, streamlines and temperature contours before and after the abrupt increment in q_w'' are shown in Figs. 5.4(c) and 5.4(a), which correspond to flow rates of 60ml/min and 400ml/min respectively. As shown in Fig. 5.3, for a given θ_o, this transition occurs at a certain value of Re_o, therefore if the channel height increases, then the critical flow rate decreases. Heat transfer is enhanced when boundary layers do not merge because of the flow rate concentration near the walls due to the swirl induced crossflow and entrainment. For $2h = 100\mu$m the curve is smooth because hydrodynamic boundary layers always merge for the calculated flow rates.

Reducing the channel height is desired for high heat flux cooling applications, but only up to a point. The designer should keep in mind Fig. 5.3 and the structure of the boundary layers, as entrainment enhances heat transfer substantially.

5.4.2 Effect of the flow inlet angle

The effect of flow inlet angle on the performance of the swirl flow channel heat sink is investigated. For this purpose the total pressure drop, Δp, and the average wall heat flux, q_w'', are calculated for three designs with different flow inlet angles $\theta_o = 3.18^o$, 9.46^o and 26.57^o. Performance curves for flow rates up to $\dot{V}_{\text{max}}$ are shown in Fig. 5.6.

As shown in Fig. 5.6(a), the smaller the flow inlet angle, the larger the pressure drop. Due to the increase in the inlet swirl, the pressure gradient must also increase to overcome the centrifugal acceleration, this effect becomes more important as the flow rate increases. The average wall heat flux also grows with a more tangential flow inlet (smaller θ_o), as shown in Fig. 5.6(b). For the base case design, $\theta_o = 9.46^o$, an abrupt increment in q_w'' is observed at given flow rates. As discussed in the previous section this happens because, for this case, hydrodynamic boundary layers merge at low $\dot{V}$ and become non entraining over a critical value of $\dot{V}$. As shown in Fig. 5.3, for a smaller θ_o, this transition occurs for a smaller value of Re_o, therefore if the flow inlet angle decreases, then the critical flow rate also decreases. For $\theta_o = 3.18^o$ boundary layers become non entraining for $\dot{V} > 160$ml/min, whereas for $\theta_o = 26.57$

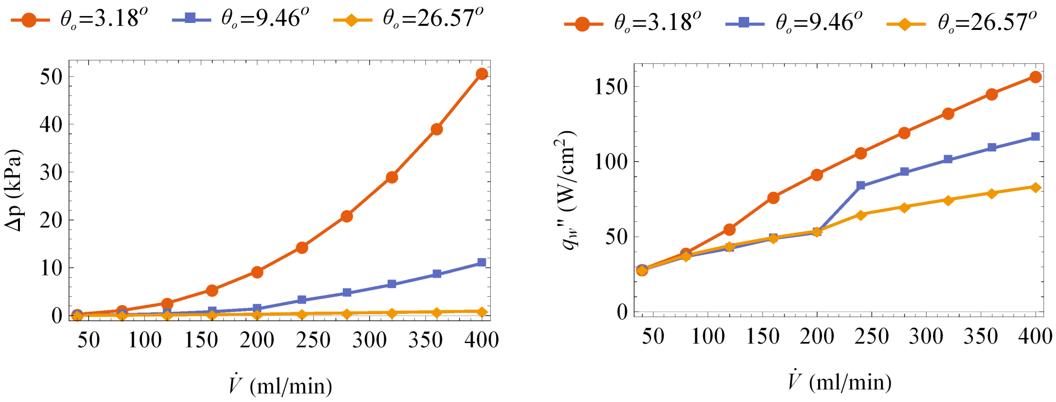

(a) (b)

Figure 5.6: Performance curves for channels with different flow inlet angles. (a) Pressure drop vs flow rate. (b) Average wall heat flux vs flow rate.

boundary layers never become non entraining. Streamlines and temperature contours for the case with $\theta_o = 3.18$ at a flow rate of 400ml/min correspond to those shown in Fig. 5.4(b). It is interesting to point out that the inlet angle has practically no effect over q''_w when boundary layers are merged, as can be observed by comparing the curves for $\theta_o = 9.46^o$ and 26.57^o for $\dot{V} \leq 200$ml/min in Fig. 5.6(b). With this in mind, it is clear that boundary layer structure is able to enhance convective heat transfer substantially.

For high heat flux cooling applications the inlet swirl should be increased as much as practically possible. Therefore the design of the fluid admission system will play an important role in the performance of the device. A feeder, plenum chamber, spiral casing, or several injection nozzles should be designed so that fluid is admitted into the channel as tangentially as possible.

5.4.3 Effect of the Prandtl number

In order to study the effect of changing the Prandtl number, the working fluid is changed. Conventional process fluids, such as oil, water, and ethylene glycol mixture are poor heat transfer fluids because of their low thermal conductivity. Over the last decade, convective heat transfer enhancement with nanofluids has been an active research topic [95, 96, 97, 98, 99, 100]. Nanofluids are colloidal suspensions with solid particle diameters of 1–100nm, and are considered to offer important advantages over conventional heat transfer fluids. The materials of suspended nanoparticles, such as Al_2O_3, CuO, Cu, SiO, and TiO, have a thermal conductivity which is much higher than the base fluid. Therefore, the effective thermal conductivity of the suspension is significantly higher than that of the base fluid, thus increasing heat transfer substantially even at low concentrations [98].

In this subsection, convective heat transfer enhancement using a water-Cu nanoparticles suspension is investigated for the swirl flow channel heat sink. For this purpose, the effective thermophysical properties of the nanofluid are approximated using several models found in literature [101, 102, 103, 104, 105]. For the density a simple volume-weighted average is used as follows

$$\rho_\mathrm{eff} = \rho_\mathrm{f}\ (1-\phi) + \rho_\mathrm{p}\ \phi. \tag{5.1}$$

The same is used for the specific heat capacity

$$(\rho C_p)_\mathrm{eff} = (\rho C_p)_\mathrm{f}\ (1-\phi) + (\rho C_p)_\mathrm{p}\ \phi. \tag{5.2}$$

In the year 1952 Brinkman extended Einstein's formula and derived a model for the dynamic viscosity of suspensions with moderate particle concentrations, up to 4vol% [102]. According to a review by Mishra et al., Ref. [101], the model of Brinkman is widely accepted among researchers

$$\mu_\mathrm{eff} = \frac{\mu_\mathrm{f}}{(1-\phi)^{2.5}}. \tag{5.3}$$

Thermal conductivity is approximated with the expression given by Hamilton and Crosser [103]

$$\kappa_\mathrm{eff} = \kappa_\mathrm{f}\left(\frac{\kappa_\mathrm{p} + (n-1)\kappa_\mathrm{f} - (n-1)\phi(\kappa_\mathrm{f} - \kappa_\mathrm{p})}{\kappa_\mathrm{p} + (n-1)\kappa_\mathrm{f} + \phi(\kappa_\mathrm{f} - \kappa_\mathrm{p})}\right), \tag{5.4}$$

where n is a shape factor, for a sphere $n = 3$ and for a cylinder $n = 6$. In Eqs. (5.1)–(5.4), ϕ is the particle volume fraction, and the subscripts $()_\mathrm{eff}$, $()_\mathrm{f}$ and $()_\mathrm{p}$ denote the thermophysical properties of the suspension, the base fluid and the solid particles respectively.

Performance of the heat sink base case design is investigated for three Prandtl numbers $Pr = 2.20$, $Pr = 1.87$, and $Pr = 1.62$. These values are obtained using a suspension with water as the base fluid and different concentrations of spherical Cu particles, $\phi = 0$vol%, 2vol% and 4vol% respectively. The properties of copper that were used are $\rho_\mathrm{p} = 8933\,\mathrm{kg/m^3}$, $(C_p)_\mathrm{p} = 385$ J/(kg K), and $\kappa_\mathrm{p} = 401$ W/(mK). In order to explain the results, changes in the termophysical properties of the water-Cu nanofluid with the particle volume fraction are calculated using Eqs. (5.1)–(5.4), as shown in Fig. 5.7.

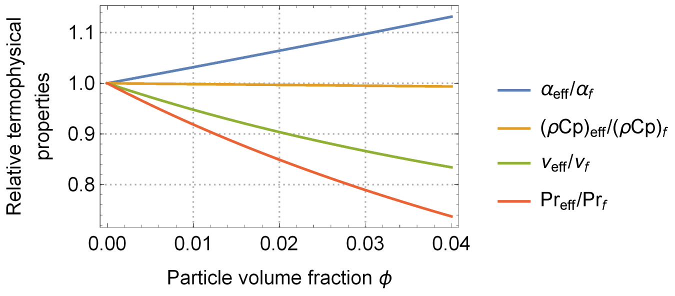

Figure 5.7: Suspension relative thermophysical properties: thermal diffusivity, specific heat capacity, kinematic viscosity, and Prandtl number as a function of the particle volume fraction.

Total pressure drop and average wall heat flux are calculated for the three Prandtl numbers $Pr = 2.20$, $Pr = 1.87$, and $Pr = 1.62$, which correspond to pure water, a 2vol% water-Cu nanofluid, and a 4vol% water-Cu nanofluid, as shown in Fig. 5.8.

Using the working fluid with lower Prandtl number results in a slight increase of the total pressure drop, as shown in Fig. 5.8(a). This happens because of the lower relative kinematic viscosity associated with the higher particle volume fraction, as shown in Fig. 5.7, which

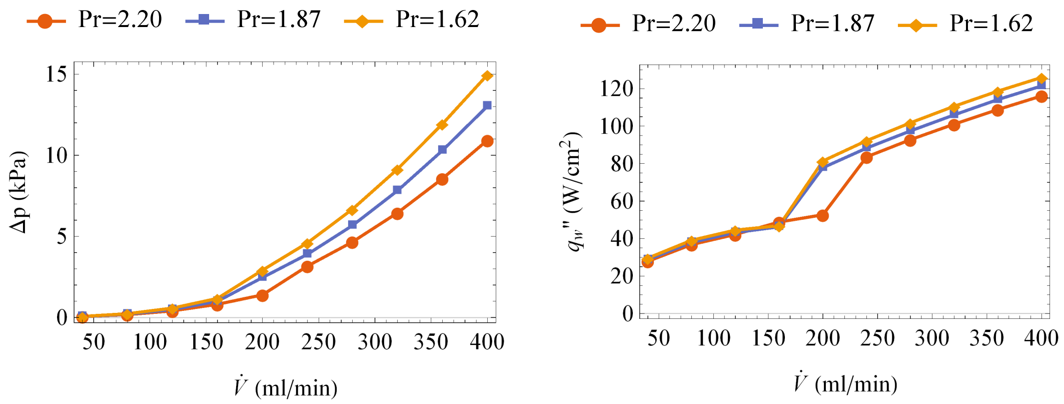

(*a*) (*b*)

Figure 5.8: Performance curves for working fluids with different Prandtl numbers. (*a*) Pressure drop vs flow rate. (*b*) Average wall heat flux vs flow rate.

increases the Reynolds number. With a decrease in the Prandtl number, the average wall heat flux increases for flow rates over 160ml/min, as shown in Fig. 5.8(*b*). Because of the decrease in kinematic viscosity, there is an increase in Re_o, therefore the transition to non entraining boundary layers occurs at a lower value of $\dot{V}$. The higher q_w'' after the change in boundary layer structure is attributed to this increase in Re_o, as well as the higher thermal diffusivity also associated with the lower Pr. Compared to ν and α, changes in the specific heat capacity are so small that its effect on the total heat flux is negligible.

5.4.4 Design recommendations

In previous sections, it was found that, compared to the base case design, heat transfer in the device is enhanced when reducing the channel height, decreasing the flow inlet angle, or lowering the Prandtl number by changing from water to a nanofluid. A comparison of the heat sink performance for these cases, where heat transfer enhancement is observed, is presented. It is also important to compare the average Nusselt number, which is calculated as $Nu = (4h)q_w''/\kappa(T_w - T_m)$, where T_m is the mean temperature inside the channel. The total pressure drop, average wall heat flux, the ratio of pumping power to heat rate, $\dot{\mathcal{W}}/\dot{Q}$, and the Nusselt number are shown in Fig. 5.9.

Heat transfer enhancement reducing the channel height or decreasing flow inlet angle is greater than that obtained using a working fluid with lower Prandtl number, but at the cost of a greater pressure drop, as shown in Figs. 5.9(*a*) and 5.9(*b*). Figure 5.9(*c*) shows that the ratio of pumping power to heat rate is higher for the variations in h and θ_o, whereas changing to a nanofluid results in a slight increase from the base case. The mechanisms for heat transfer enhancement are identified by comparing the average Nusselt number obtained for the base case to that of the other design modifications in Fig. 5.9(*d*). It is shown that, Nu is nearly constant with increasing flow rate for merged boundary layers, and it grows with increasing flow rate when entraining effects and secondary flows are present. Therefore, for the reduction in the channel height, the increase in q_w'' is mainly due to an increase in

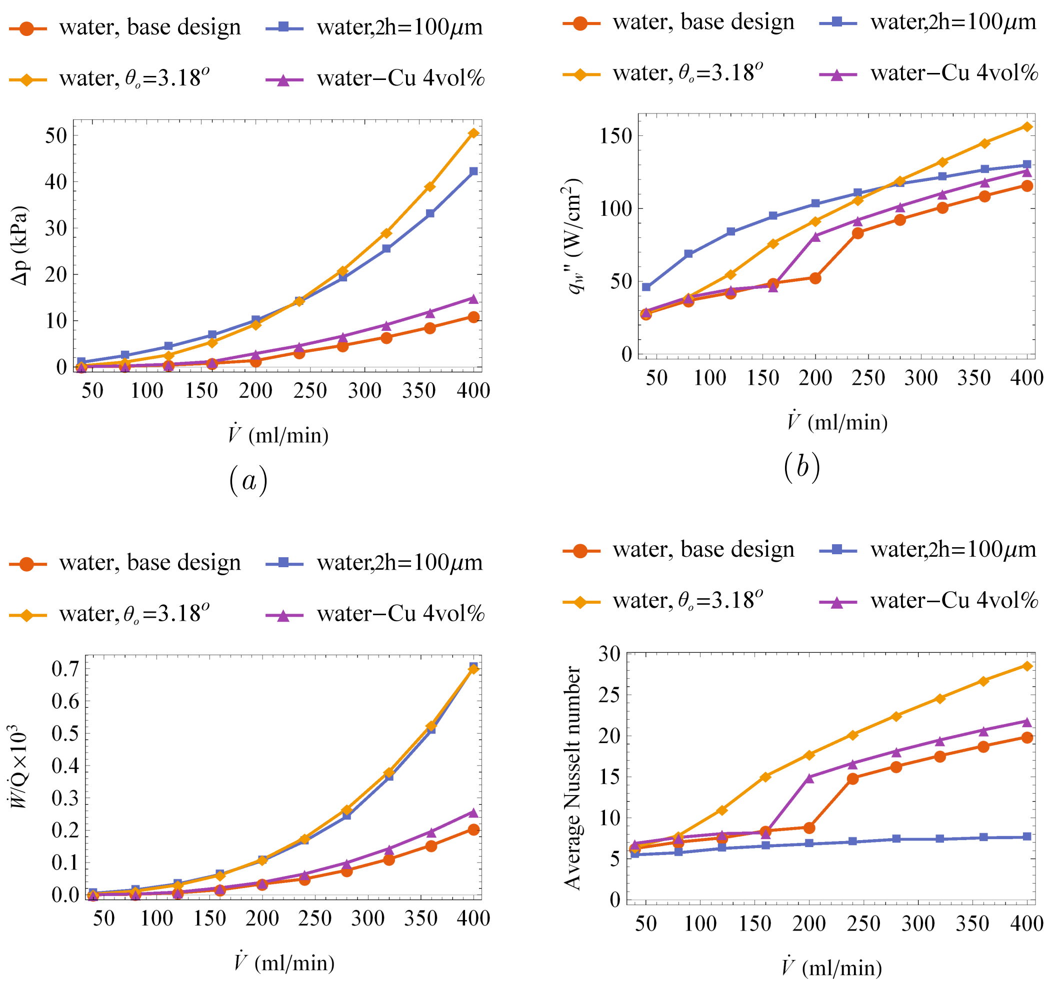

(*a*) (*b*)

(*c*) (*d*)

Figure 5.9: Performance curves for design variations that present heat transfer enhancement. (*a*) Pressure drop vs flow rate. (*b*) Average wall heat flux vs flow rate. (*c*) Ratio of pumping power to heat rate vs flow rate. (*d*) Average Nusselt number vs flow rate.

conductive heat transfer. On the other hand, for the change to nanofluid and the decrease in the flow inlet angle, q''_w increases due to convective heat transfer enhancement. In future research, correlations for the average Nusselt number could be established for each type of boundary layer structure.

A parameter commonly used to compare and select heat sinks is the thermal resistance defined as $R_{hs} = (T_w - T_o)/q''_w$. Table 5.3 shows a summary of the performance characteristics at $\dot{V} = 400\text{ml/min}$ of the swirl flow channel heat sink designs studied in this section.

Values in Table 5.3 are compared to data for other devices used for high heat flux applications from the review by Agostini et al. [6]. The average heat flux for the base design of the device studied is about 25% of the highest value reported in the review, nevertheless the ratio of pumping power to heat rate is about 20% of the lowest value listed, as shown in Fig. 5.10.

Table 5.3: Performance of swirl flow channel heat sink design variations at $\dot{V} = 400$ml/min.

Working fluid	$2h$ (μm)	θ_o (^{o})	Δp (kPa)	q''_w (W/cm^2)	$\dot{\mathcal{W}}/\dot{Q}$ ($\times 10^3$)	R_{hs} (K cm^2/W)
water	300	9.46	10.93	116.11	0.204	0.52
water-Cu 4 vol%	300	9.46	15.93	128.76	0.269	0.47
water	100	9.46	42.11	129.66	0.704	0.46
water	300	3.18	50.71	156.85	0.702	0.38

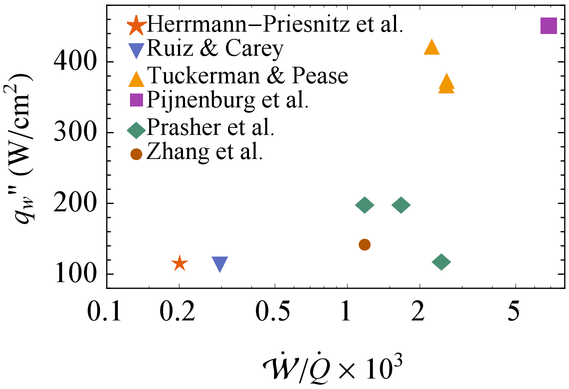

Figure 5.10: Single phase microchannel heat sink comparison. Data from Refs. [6] and [15].

The data from Ref. [6] used for comparison is only that of single phase microchannel heat sinks that use water as the operating fluid and are designed to maintain wall temperature below 85^{o}C, which is a common requirement for applications such as thermal management of electronics.

Chapter 6

Results for stability and receptivity

Steady state flow in the swirl flow channel heat sink was studied numerically in the previous chapter, and different boundary layer structures were observed depending on the governing parameters. Rotation of the fluid induces a crossflow and entrainment, which was found to enhance convective heat transfer considerably due to motion of fluid towards the heat exchange surface. This effect depends on the structure of hydrodynamic boundary layers, and is intensified for small flow inlet angles and high Reynolds number. Parabolic velocity profiles are found for low Reynolds numbers, while large inflection of the radial velocity component occurs for higher values. Whether these highly inflected profiles can occur in the real world device is a matter of stability.

In this chapter, we use the framework of nonmodal stability theory presented in Chapter 3 to study optimal energy growth of initial perturbations and the response of temperature disturbances to a momentum forcing. Configuration of the steady state base flow used for the latter analyses is presented in Fig. 6.1.

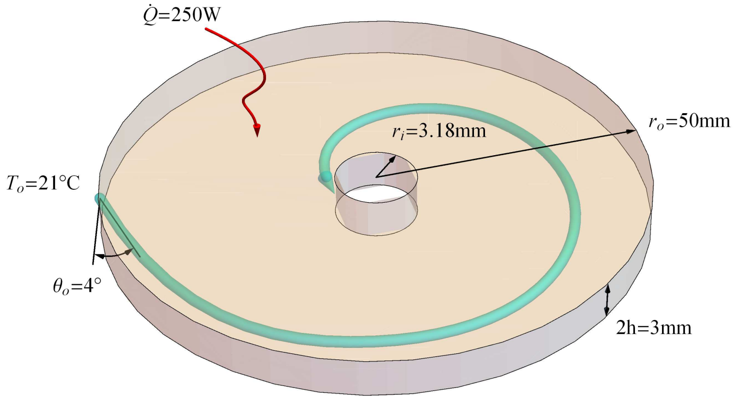

Figure 6.1: Base flow configuration used for the stability and receptivity analyses.

Results for the steady state flow are used to discuss about the local flow approximation. Experimental measurements of the pressure drop and wall temperature are used to validate the base flow in the laminar range of flow rates.

Through this chapter, we study the influence of the wavevector on the optimal growth and the componentwise receptivity. In order to do this, instead of using the radial and azimuthal components of the wavevector α and β, we use its magnitude $k = \sqrt{\alpha^2 + \beta^2}$ and the waveangle defined as $\theta_k = \arctan(\alpha/\beta) - \theta_c$, where θ_c is the local base flow flow angle at the midplane of the channel, measured starting from the tangential direction. With this notation, an angle $\theta_k = 0$ represents a wave propagating in the direction of flow in the midplane of the channel (aligned with θ_c), which we refer to as the streamwise direction. Therefore, we refer to $\theta_k = \pi/2$ as the crossflow direction, and it represents a wave direction normal to the flow at $z = 0$.

The optimal energy growth of initial disturbances is calculated for a range of wavenumbers, and the dependence of the maximum growth on the Reynolds number is examined. The discussion on the mechanisms of instability in the swirl flow channel is complemented with the results from the flow visualization experiment.

The amplification of temperature perturbations to forcing of the radial, azimuthal, and wall-normal momentum components is calculated for a range of wavenumbers and temporal frequencies. Characteristics of the most receptive types of forcing are used to identify effective heat transfer enhancement techniques. Finally, experimental results for the heat sink performance with a pulsating flow rate are presented, using the range of forcing frequencies provided by the receptivity analysis.

6.1 Base flow

Our base flow considers the steady state in a swirl flow channel with an inlet angle $\theta_o = 4^o$ and an aspect ratio $h/r_o = 0.03$, evaluated at a local radius r. Equations (3.1) allow us to calculate the local boundary layer thickness δ, the local flow angle θ_c at $z = 0$ (midplane), and the local Reynolds number Re, for different values of r, as shown in Fig. 6.2.

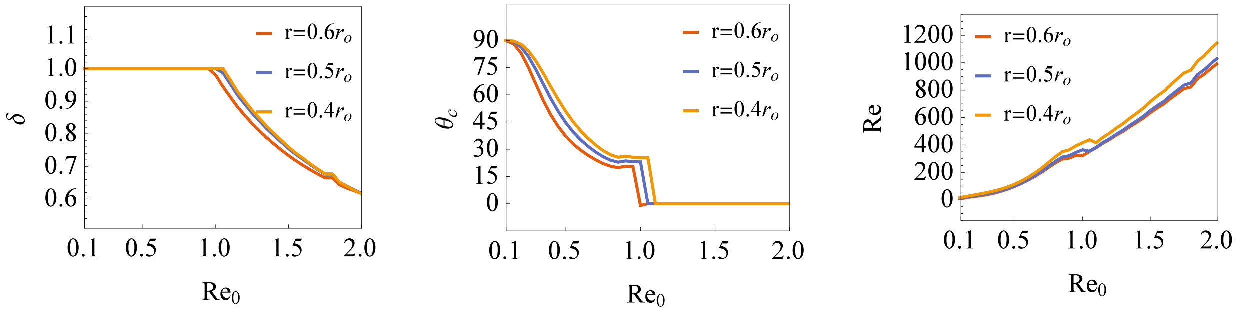

(a) (b) (c)

Figure 6.2: Base flow variables vs flow rate Reynolds number Re_o at different local radii $r/r_o = 0.4,\ 0.5$, and 0.6. (a) Boundary layer thickness δ. (b) Flow angle at the midplane of the channel θ_c, measured starting from the tangential direction. (c) Local Reynolds number Re, based on the half-height of the channel and the streamwise velocity component at $z = 0$ (midplane).

Boundary layers in the swirl flow channel are merged ($\delta = 1$) for low Re_o, they separate over a certain value Re_o, and increments over that value result in thinning of the boundary layers, as shown in Fig. 6.2.(a). Figure 6.2(b) shows how the direction of the local flow at the midplane of the channel changes as Re_o increases. Starting from radial flow ($\theta_c = 90^o$), the angle increases until we get tangential flow ($\theta_c = 0^o$) when the boundary layers separate. Figure 6.2(c) shows the values of the local Reynolds number Re increasing as a function of the flow rate Reynolds number Re_o. When the boundary layers are merged, the local flow resembles a plane Poiseuille flow in the direction of θ_c and with a Reynolds number Re which is much lower than the critical value 5772 required for the flow to be asymptotically unstable [60]. As shown in Fig. 6.2, the overall behavior of the base flow does not depend strongly on the local radius, therefore we arbitrarily select $r = 0.4r_o$ as a representative local radius for the fluid dynamics in a swirl flow channel. Although our conclusions in this study are not affected by this particular value, we consider that a global stability analysis is a logical next step for future work.

Experimental performance of the swirl flow channel heat sink for flow rates between 0.43 and 1.12 l/min without pulsations is presented in this section. The flow rate Reynolds number is calculated as $Re_o = \dot{V}h/(8\pi\nu r_o^2)$, where the viscosity is evaluated at film temperature $T_{film} = (T_o + T_w)/2$. Experimental results for the total pressure drop, wall temperature and Nusselt number as a function of Re_o are shown in Fig. 6.3.

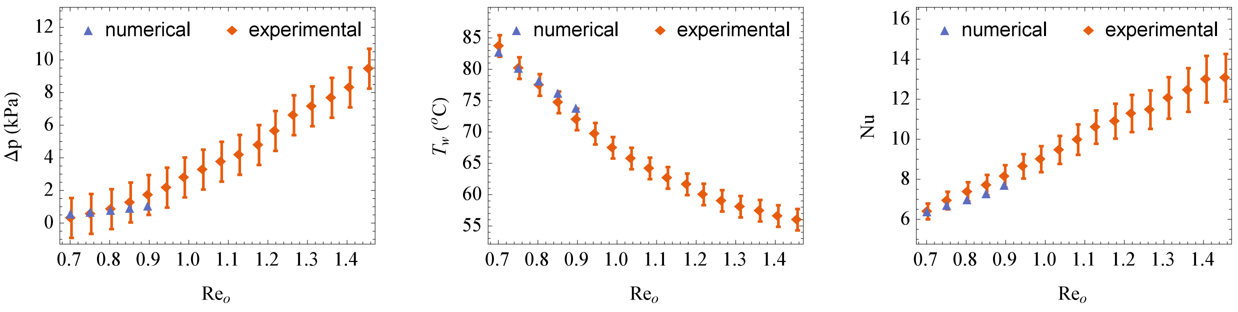

(a) (b) (c)

Figure 6.3: Numerical and experimental heat sink performance variables vs flow rate Reynolds number. (a) Total pressure drop. (b) Wall temperature. (c) Nusselt number.

Numerical results are also shown in Fig. 6.3 for flow rate Reynolds numbers up to $Re_o^c = 0.91$, where the steady state solution predicts a change in the boundary layer structure and the linear stability analysis predicts the onset of asymptotic instability. Pressure ports in the experiment are not located at the inlet and outlet of the minichannel section that corresponds to the computational domain of the numerical simulations. Therefore, the numerical values of Δp shown in Fig. 6.3.(a) consider the pressure drop from the simulations, as well as losses that take place between the pressure ports and the computational domain. These losses are calculated using typical models found in literature such as Refs. [106, 94], and include friction losses in the tubing and the feeder channel, a sudden expansion at the inlet, a sudden contraction and a 90° bend at the outlet, and the fittings. As shown in Fig. 6.3, reasonable agreement is found between the numerical and experimental results for $Re_o < Re_o^c$, thus validating the base flow that is used through this chapter for the stability and receptivity analyses.

The parameters that that govern the local base flow are: the local Reynolds number Re

Table 6.1: Local base flow parameters for $Re_o = 0.9$ at $r = 0.4r_o$.

Re	Pr	θ_c
200.97	3.41	32.17°

based on the half-height of the channel and the streamwise velocity component $\sqrt{U^2 + V^2}$ at $z = 0$, the Prandtl number Pr, and the local flow angle at the midplane of the channel θ_c, measured starting from the tangential direction. Table 6.1 shows the values of these parameters for the local base flow (at $r = 0.4r_o$) used through this chapter for $Re_o = 0.9$.

6.2 Mesh sensitivity and modal truncation

This section presents the sensitivity analyses carried out to select the number of Chebyshev collocation points N used to discretize in the z direction, and the number of modes K used for order reduction. Table 6.2 shows the real and imaginary parts of the 10^{th} eigenvalue of $\mathbf{L}$ for $k = 1$ and $\theta_k = 0$. We use $N = 120$ collocation points, as it is sufficient resolution to get convergence of up to 8 digits.

Table 6.2: Mesh sensitivity of the 10^{th} eigenvalue for $k = 1$ and $\theta_k = 0$.

N	$\mathrm{Re}(\lambda_{10})$	$\mathrm{Im}(\lambda_{10})$
20	-0.20314397	-0.36092704
60	-0.20335108	-0.36428062
120	-0.20335107	-0.36428062
200	-0.20335107	-0.36428062

To reduce the computational cost, the state vector $\hat{\mathbf{q}}$ is represented as an eigenfunction expansion using only K modes instead of all $3N - 6$. The response to radial forcing $\mathcal{R}_{u\tau}$ for $k = 10$, $\theta_k = 0$ and $\omega = 0$ is calculated for different values of K, as shown in Fig. 6.4.

Modal truncation using $K = 180$ modes is enough to get accurate results.

6.3 Stability and transient growth

This section covers the linear stability analysis of the base flow. Optimal growth $G(t)$ is calculated for flow rate Reynolds numbers Re_o between 0.1–2, and the influence of the total wavenumber k and the waveangle θ_k is studied. Figure 6.5 shows the different behaviors of $G(t)$ that can be observed for different k, θ_k, and Re_o. Flow may be asymptotically unstable

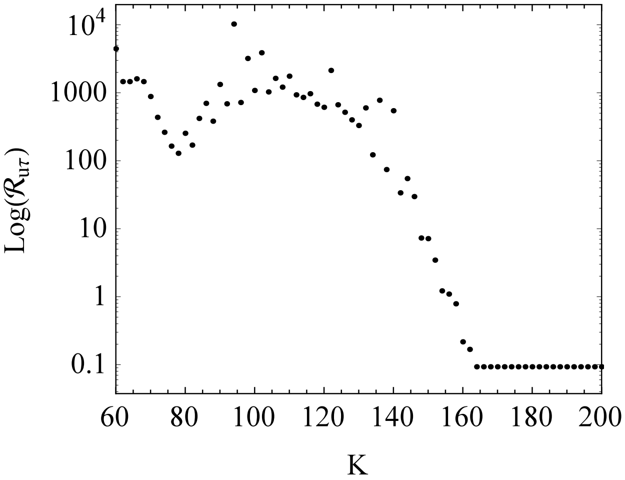

Figure 6.4: Sensitivity of $\mathcal{R}_{u\tau}$ for $k = 10$, $\theta_k = 0$ and $\omega = 0$ to the number of modes K used for modal truncation.

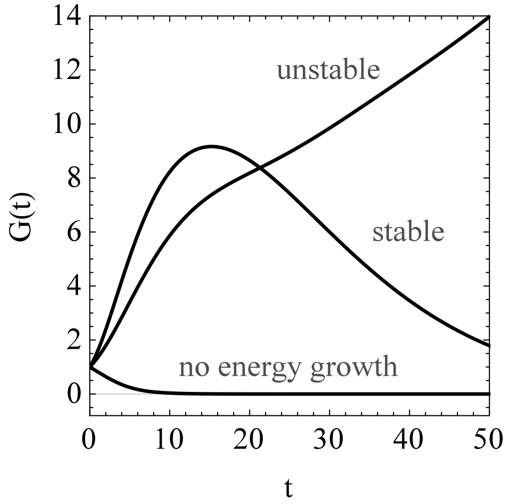

Figure 6.5: Optimal growth $G(t)$ in the crossflow direction. Curves labelled unstable for $Re_o = 1.07$ and $k = 0.75$, stable for $Re_o = 0.62$ and $k = 2.25$, and no energy growth for $Re_o = 0.30$ and $k = 2.25$.

and therefore have unbounded energy growth, it may be stable but present some transient growth, or it can present monotonic energy decay, as shown in Fig. 6.5.

For asymptotically stable flows we define the maximum growth rate as the maximum value of $G(t)$ for all time, and denote it G_{max} which is a function of k, θ_k, and Re_o. The dependence of G_{max} on the total wavenumber k and the waveangle θ_k for $Re_o = 0.8$ is shown in Fig. 6.6. Maximum growth is observed for $k = 2.12$ along the crossflow direction, where the base flow velocity profiles are most inflectional. When the flow is asymptotically unstable, the fastest growing mode corresponds to axisymmetric circular waves that travel radially inward.

The Re_o dependence of G_{max} in the crossflow direction, and the neutral curve for asymptotic stability are shown in Fig. 6.7. Two important values for the flow rate Reynolds numbers are calculated: $Re_o^E = 0.36$, below which there is no energy growth of disturbances,

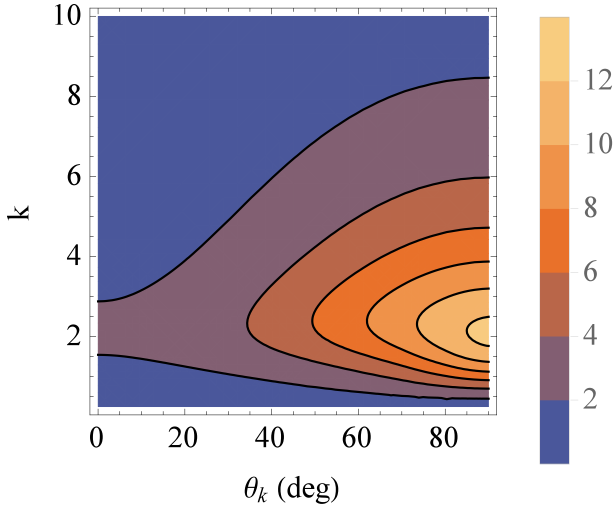

Figure 6.6: Maximum growth rate G_{max} as a function of the total wavenumber k and the waveangle θ_k for $Re_o = 0.8$.

and $Re_o^c = 0.91$ that delimits the onset of asymptotic instability where there is unbounded energy growth. Between these values, perturbations experience transient growth followed by asymptotic decay, where the kinetic energy is amplified up to $O(10)$, as shown in Fig. 6.7. For plane Poiseuille flow, transient growth plays an important role in the transition process, whereas for the swirl flow channel we find very small transient growth. This suggests that the mechanism for transition is the change in the shape of the velocity profile due to rotational effects (crossflow instability). In fact, the value for Re_o^c coincides with the change in boundary layer structure reported in the previous chapter. It is worth noting that Ruiz and Carey in Ref. [15] observed that their experimental results deviated from laminar behavior for flow rates over 190 ml/min, which corresponds to $Re_o = 0.86$ according to our definition of the flow rate Reynolds number. Therefore, we find reasonable agreement between experimental observations and predictions from our simplified analysis. The critical value for the Reynolds number, Re_o^c is also useful to determine bounds for the validity of assumptions and models of the flow inside this type of channel.

Results from the stability analysis are qualitatively compared to the diffusion patterns observed in the flow visualization experiment. In the experiment, photographs were taken at flow rates of 600, 800, 1000, 1200, and 1400ml/min ($Re_o = 0.57,\ 0.76,\ 0.95,\ 1.14$, and 1.33), as shown in Fig. 6.8.

For comparison, Fig. 6.8 also shows the asymptotic growth rate $\mathrm{Re}(\lambda_1)$ for crossflow modes maximized over all wavenumbers plotted as a function of the flow rate Reynolds number. Laminar flow is observed for the two leftmost photographs in Fig. 6.8, corresponding to the lowest Reynolds numbers. Diffusion of the colored water and unsteadiness occur for the higher Reynolds numbers, where $Re_o > Re_o^c = 0.91$.

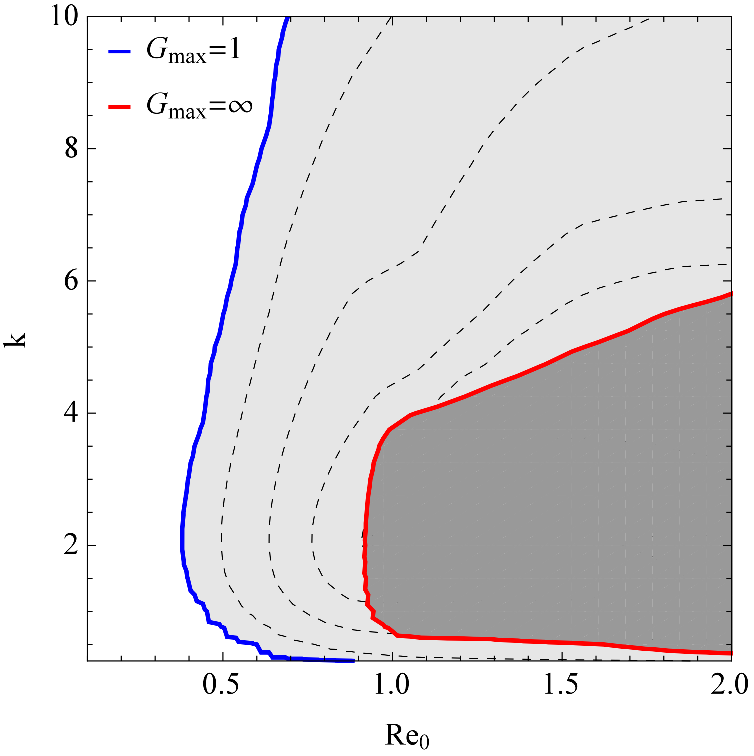

Figure 6.7: Maximum growth rate G_{max} as a function of the total wavenumber k and the the flow rate Reynolds number Re_o for $\theta_k = 90°$. Three regions can be distinguished: Asymptotic instability (*dark gray*), asymptotic decay with transient growth (*light gray*), and asymptotic decay without energy growth (*white*). Dashed contour levels, from left to right, $G_{max} = 2, 5, 10, 15$.

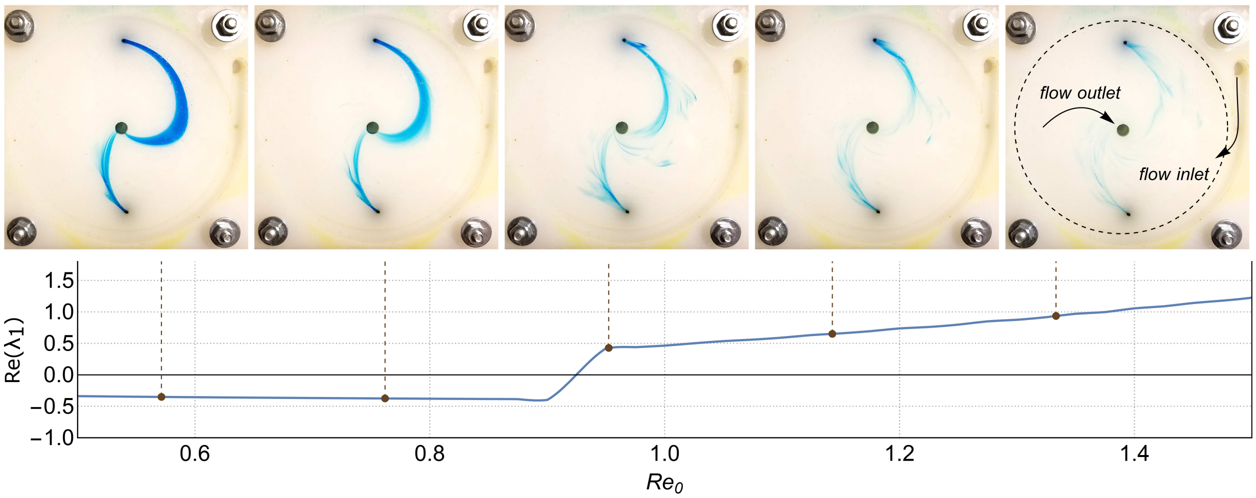

Figure 6.8: Asymptotic growth rate for crossflow modes maximized over all wavenumbers from the linear stability analysis compared to images from the flow visualization experiment.

6.4 Componentwise response

In this section we present our results and analysis of the componentwise response of the base flow and its dependence on the wavevector and temporal frequency for $Re_o = 0.9$. The componentwise response of the system is calculated for wavenumbers between $k = 0.01$ and 6, and waveangles varying from the azimuthal direction ($\theta_k = -32.17° \approx -\pi/6$) to the crossflow direction ($\theta_k = \pi/2$). Results for different values of the temporal frequency ω are shown in Figs. 6.9(a), 6.10(a) and 6.11(a), for a forcing in the radial, azimuthal and wall-normal momentum components, respectively. Our results for the componentwise $\mathcal{H}_\infty$-norm (response maximized over all ω) are shown in Figs. 6.9(b), 6.10(b) and 6.11(b), for radial, azimuthal and wall-normal momentum forcing respectively.

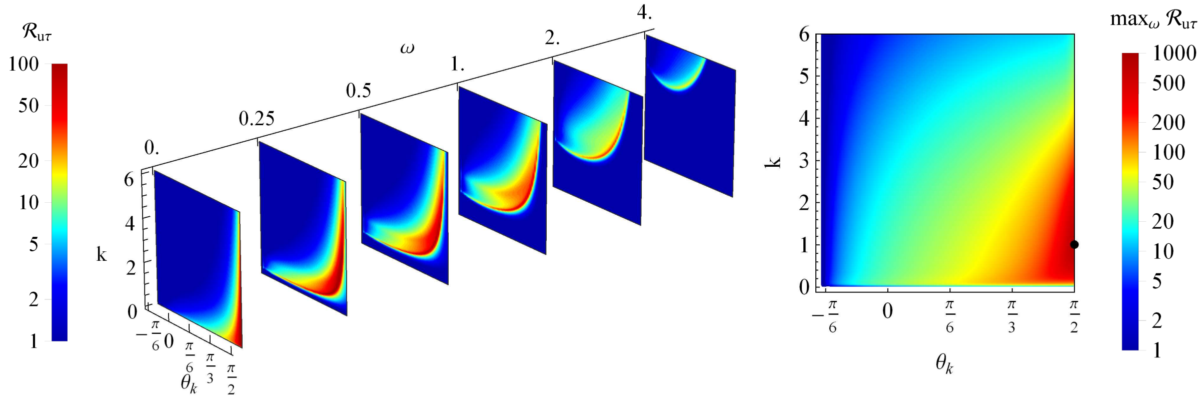

(a) (b)

Figure 6.9: Response to radial momentum forcing $\mathcal{R}_{u\tau}$ as a function of the total wavenumber k and the waveangle θ_k. (a) Slices for different values of the temporal frequency ω. (b) Response maximized over all ω. The largest response is indicated by a black dot.

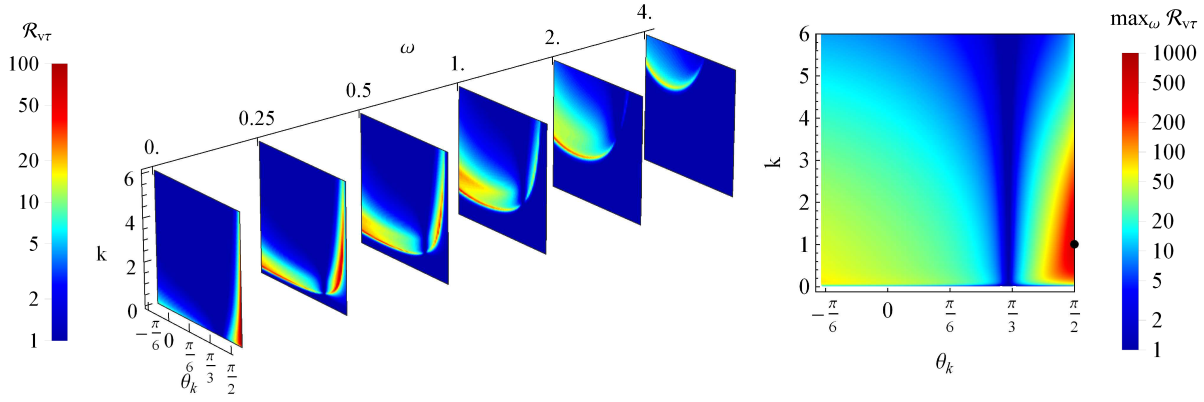

(a) (b)

Figure 6.10: Response to azimuthal momentum forcing $\mathcal{R}_{v\tau}$ as a function of the total wavenumber k and the waveangle θ_k. (a) Slices for different values of the temporal frequency ω. (b) Response maximized over all ω. The largest response is indicated by a black dot.

Temperature perturbations are most amplified by streamwise independent structures, i.e., streamwise vortices and streaks ($\theta_k = \pi/2$), as shown in Figs. 6.9(b), 6.10(b) and 6.11(b).

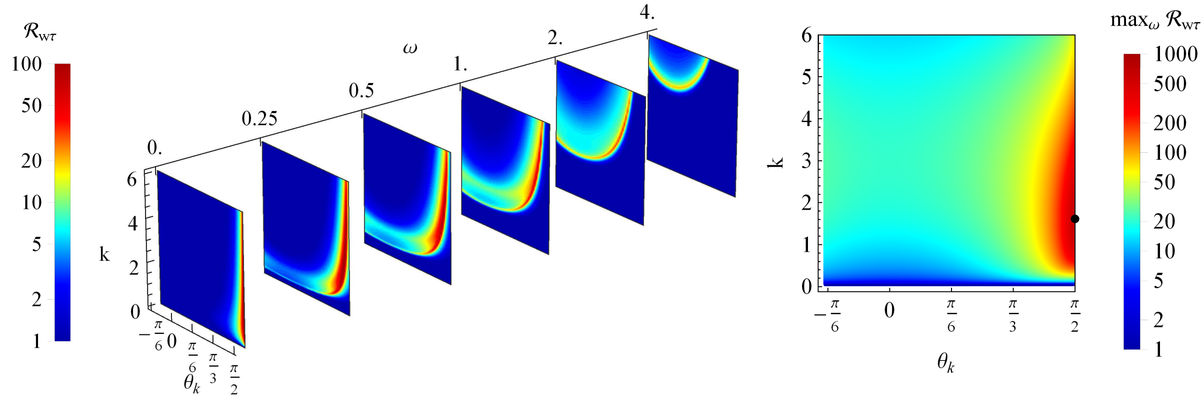

(a) (b)

Figure 6.11: Response to wall-normal momentum forcing $\mathcal{R}_{w\tau}$ as a function of the total wavenumber k and the waveangle θ_k. (a) Slices for different values of the temporal frequency ω. (b) Response maximized over all ω. The largest response is indicated by a black dot.

The maximum response is of order $O(10^3)$ for all forcing components, where the largest amplification corresponds to radial, then wall-normal, and then azimuthal forcing. These largest amplifications occur for a forcing frequency $\omega = 0$ and, as ω increases, the maximum response decreases and oblique (spiral) waves become the most amplified structures, as shown in Figs. 6.9(a), 6.10(a) and 6.11(a). Increasing ω further, the dominant structures become axisymmetric inward traveling waves ($\theta_k = -\theta_c + \pi/2 \approx \pi/3$) with an amplification of order $O(10^2)$. At even higher frequencies, amplifications are of order $O(10)$ and, azimuthally propagating waves ($\theta_k = -\theta_c \approx -\pi/3$) dominate for azimuthal forcing, while for radial and wall-normal forcing the dominant structures are streamwise propagating waves ($\theta_k = 0$), which we interpret as the spiral analog to T-S waves.

The results presented above are useful for developing heat transfer enhancement strategies, as we now know what are the flow structures that generate the largest response in the temperature field for a given range of excitation frequencies.

6.5 Heat transfer enhancement strategies

In order to develop a feasible heat transfer enhancement strategy, many practical considerations have to be taken into account. An actuator has to be designed that is able to excite waves that propagate in a particular direction for a specific range of forcing frequencies. It is also desired that the actuator is easy to manufacture and to integrate with the heat sink design. With this in mind, we will propose and discuss two strategies to enhance heat transfer with distinct objectives: 1) maximum amplification, and 2) simple implementation.

From Figs. 6.9, 6.10 and 6.11 we know that the maximum amplification is obtained for crossflow stationary waves with $\omega = 0$ (streamwise independent structures). In order to excite said structures, we propose micromachining the channel walls with spiral grooves that follow the predicted streamlines of the base flow. These grooves should be spatially periodic in the crossflow direction with a wavelength corresponding to the wavenumber that provides the largest amplification. The passive actuation is expected generate streamwise independent perturbations of the base flow in the wall-normal direction, therefore, in order to study the response to this type of forcing, we calculate $\mathcal{R}_{w\tau}$ for $\theta_k = \pi/2$, which is shown in Fig. 6.12.

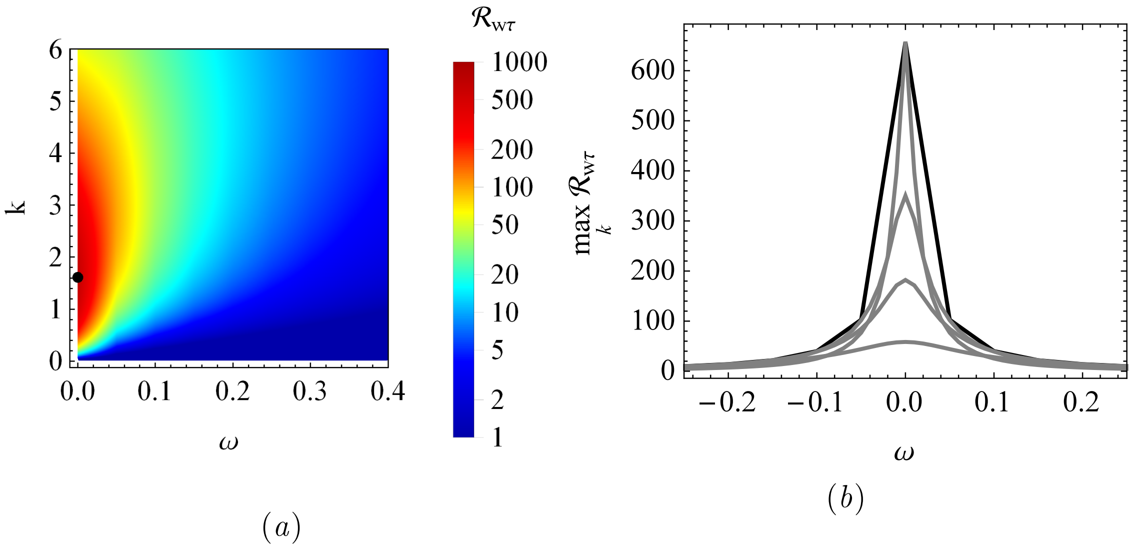

Figure 6.12: Response to wall-normal forcing of crossflow waves ($\theta_k = \pi/2$). (a) Response as a function of the total wavenumber k and temporal frequency ω. The maximum amplification is marked with a black dot. (b) Response maximized over all wavenumbers in black, and for selected wavenumbers in gray.

Large amplifications are obtained for a narrow range of forcing frequencies concentrated around $\omega = 0$, and the maximum response occurs for $k = 1.61$, as shown in Fig. 6.12(a). Structures of different wavenumbers dominate for every frequency excited, therefore the response to the actuation is given by the amplification maximized over all k, that is, the envelope of the frequency response for all k, as shown in Fig. 6.12(b).

As a second heat transfer enhancement strategy, we propose using a pulsating flow rate, which can be achieved using the actuator described in Section 4.2. Implementation of this strategy is very simple, as it does not require any modifications to the heat sink design. Using a pulsating flow rate results in an oscillating perturbation of the pressure gradient, and therefore a forcing in the radial momentum component. Pulsations are generated in the tubing upstream of the minichannel, hence we expect only streamwise propagating perturbations to reach the device. Consequently in order to study the response to this type of forcing, we calculate $\mathcal{R}_{u\tau}$ for $\theta_k = 0$, which is shown in Fig. 6.13.

Moderate amplifications are obtained for a wide range of forcing frequencies, and the maximum response occurs for $k = 0.11$ at $\omega = 0.10$, as shown in Fig. 6.13(a). As the forcing frequency increases, the largest response is obtained for a larger wavenumber, hence for a shorter wavelength. The response to the pulsating flow rate is given by the amplification maximized over all k, that is, the envelope of the frequency response for all k, as shown in Fig. 6.13(b).

It is important to remark that, the strategies here presented are based on the fact that a

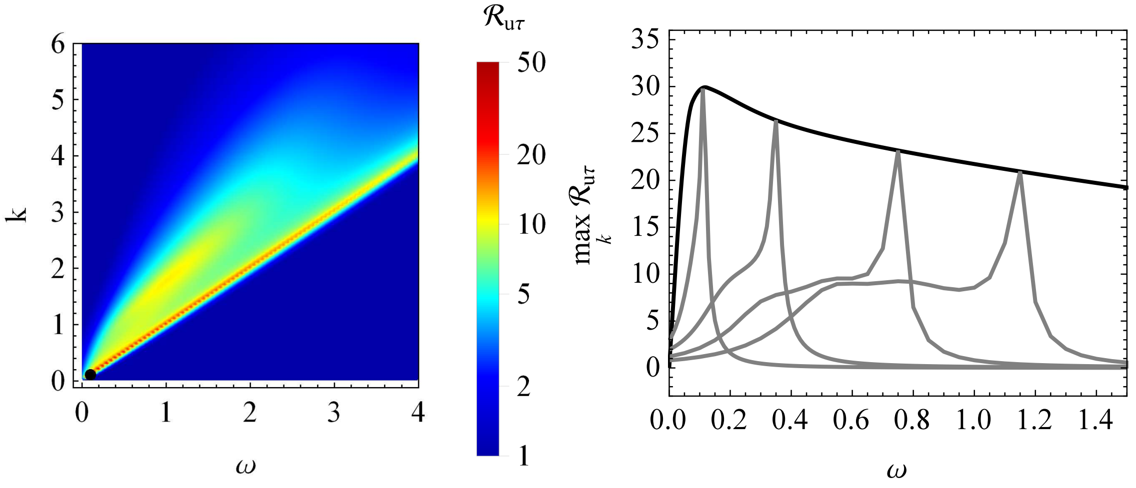

(a) (b)

Figure 6.13: Response to radial forcing of streamwise propagating waves ($\theta_k = 0$). (a) Response as a function of the total wavenumber k and temporal frequency ω. The maximum amplification is marked with a black dot. (b) Response maximized over all wavenumbers in black, and for selected wavenumbers in gray.

large temperature response to a momentum forcing suggests a heat transfer enhancement, but nothing has been said about the kinetic energy loss that may be associated with it. This may result in a higher pressure drop across the channel, and consequently an undesired heat sink performance. Experimental results for the performance of the swirl flow minichannel heat sink with a pulsating flow rate are presented in the next section. Based on the receptivity analysis, the channel with streamwise and spiral grooves should be a more efficient strategy for enhancing heat transfer. Nevertheless, testing this hypothesis experimentally requires manufacturing several devices, therefore it will be investigated in future work. In addition to the strategies here discussed, other more sophisticated techniques may be implemented using the information provided by the receptivity analysis, such as blowing and suction, vortex generators, or acoustic excitation.

6.6 Case study: pulsating flow rate

Experimetal results of the heat sink performance using a pulsating flow rate are presented in this section as a proof of concept. The range of the pulsation frequencies studied is based on the response of the system to the perturbations expected for this type of forcing, i.e., streamwise propagating waves. The actuator described in section 4.2 is used with a different number of rods to generate pulsations with frequencies of 1.67, 3.33, 6.67, 13.33, and 26.67s^{-1}. These correspond to the dimensionless angular frequencies $\omega = 0.22,\ 0.44,\ 0.88,\ 1.76$ and 3.52, based on the scales used for the receptivity analysis. The RMS pressure drop, wall temperature and Nusselt number present a similar behavior for all frequencies, and the largest response is observed for $\omega = 0.88$, which is shown in Fig. 6.14.

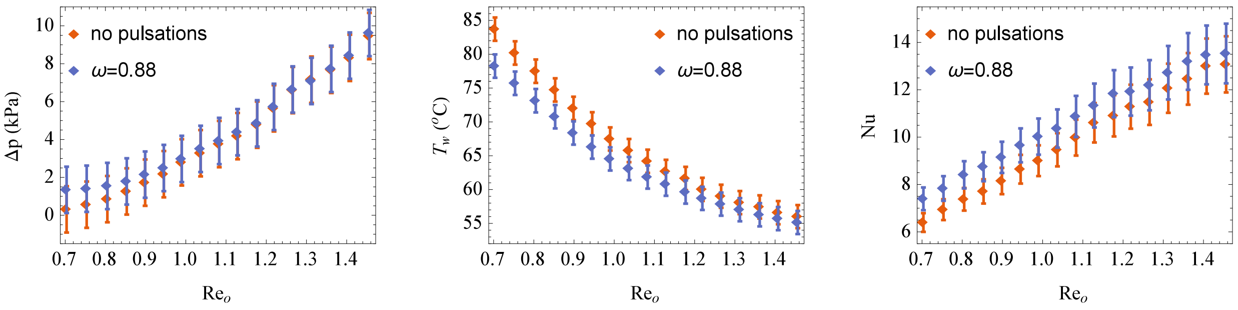

(*a*) (*b*) (*c*)

Figure 6.14: Experimental heat sink performance variables vs flow rate Reynolds number with and without forcing. (*a*) Total pressure drop. (*b*) Wall temperature. (*c*) Nusselt number.

Figure 6.14(*a*) shows that the pulsations slightly increase the total pressure drop, and this effect becomes accentuated for lower flow rate Reynolds numbers. On the other hand, for the same Re_o, the wall temperature is noticeably reduced by the actuation, with up to a 5°C difference for the lowest flow rate tested, as shown in Fig. 6.14(*b*). Because the heat input to the system is unchanged, this means that convective heat transfer is being enhanced, as evidenced by the measurements of the Nusselt number shown in Fig. 6.14(*c*).

In order to assess if the changes in performance using a pulsating flow rate are desirable, we calculate the following indicators: 1) the reduction in the pumping power required to achieve the same wall temperature as in the unforced case, and 2) the enhancement of the Nusselt number using the same pumping power as in the unforced case. These indicators are shown in Fig. 6.15 as a function of the pulsation frequency for $Re_o = 0.99$.

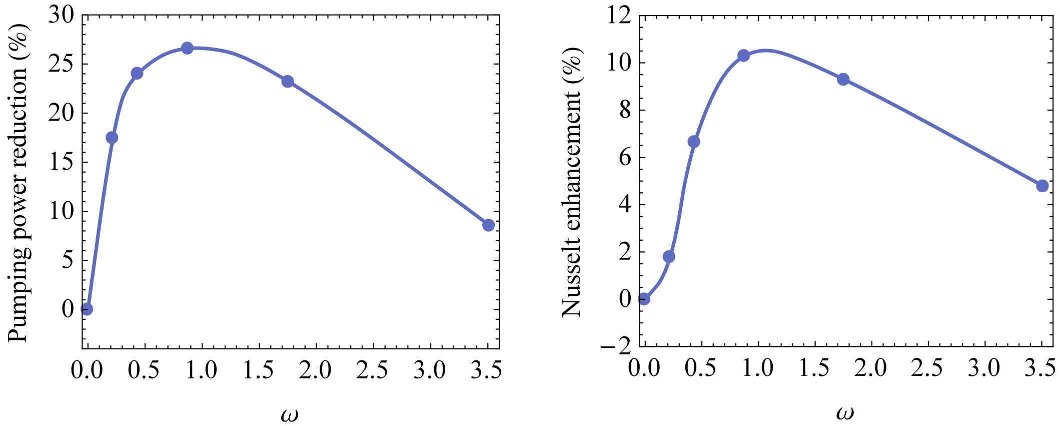

(*a*) (*b*)

Figure 6.15: Heat sink performance response to actuation as a function of the pulsation frequency ω for a flow rate Reynolds number $Re_o = 0.99$. (*a*) Pumping power reduction to achieve the same wall temperature. (*b*) Nusselt enhancement at the same pumping power.

According to figure 6.15(*a*), in order to achieve a specific wall temperature requirement, up to 26.6% less pumping power is needed when using a pulsating flow rate. If the same pumping power is used, an increment of up to 10.3% in the Nusselt number is observed with the actuation, as shown in Fig. 6.15(*b*). The experimental response curves to a pulsating flow rate, Fig. 6.15, resemble the result obtained from the receptivity analysis in Fig. 6.13(*b*), where a maximum is obtained for a relatively low frequency, and then the amplification slowly decays for higher frequencies.

These results are promising, since the receptivity analysis suggests that an even larger response should be observed for other types of forcing. However, a better heat sink performance is not guaranteed, as the pumping cost penalty may be greater than the benefit of increasing the convective heat transfer.

Chapter 7

Conclusions

This chapter summarizes the results and discussions obtained in this thesis, and presents suggestions for future research opportunities.

7.1 Concluding remarks

A promising alternative for thermal management of high heat flux applications, such as electronics and concentrated photovoltaics, is the swirl flow channel heat sink. The flow in this device has been investigated in this work with the purpose of studying the effect of design on heat sink thermohydraulic performance, determining the onset and mechanisms of hydrodynamic instabilities, and identifying efficient strategies for heat transfer enhancement.

In Chapter 5, thermohydraulic performance of the heat sink operating in steady state was calculated numerically and the effects of varying the channel height, $2h$, the flow inlet angle, θ_o, and the working fluid were investigated. A large number of cases were solved to study the development of the viscous boundary layers over a wide range of flow rate Reynolds numbers, Re_o, and θ_o. Results show that entraining boundary layers develop for high Re_o, boundary layers merge for low Re_o, and become non entraining for moderate Re_o and $\theta_o < 14^o$. In order to visualize the evolution and transitions between the different boundary layer structures, streamlines in the $r-z$ plane are plotted along with the temperature distributions.

Total pressure drop and average wall heat flux as a function of flow rate were calculated for different device designs. The design of a base case considers a channel height of $2h = 300\mu$m, a flow inlet angle of $\theta_o = 9.46^o$ and water as the working fluid. To investigate the effect of the channel height, performance curves are calculated for $2h = 100\mu$m and 500μm and compared to those of the base design. Results show that pressure drop increases with decreasing h due to the reduction in flow passage area. In addition, abrupt increments are observed in the average heat flux when boundary layers do not merge, because the flow entrainment causes fluid to be drawn towards the walls. It is interesting that unlike what happens in conventional microchannels, reducing the height may not always result in heat transfer enhancement due to boundary layers merging. When this occurs, the entrainment effect is lost, therefore the total heat flux may decrease.

To investigate the effect of the inlet angle, cases with $\theta_o = 3.18^o$ and 26.57^o were compared to the base design. Results show that pressure drop increases when θ_o decreases, which is due to the increase in the inlet swirl and consequentially larger centrifugal acceleration. When Re_o is low enough so that boundary layers merge, the inlet angle has negligible effect over the average wall heat flux. Nevertheless, heat transfer enhancement is observed when θ_o decreases for entraining and non entraining boundary layers. Therefore, for high heat flux applications, fluid should be admitted into the channel as tangential as practically possible.

The effect of reducing the Prandtl number, Pr, was investigated by comparing the performance of the heat sink using water and using a 2vol% and a 4vol% water-Cu nanofluid. Effective termophysical properties of the suspension were approximated with models found in the literature. Using the nanofluid results in higher pressure drop and average wall heat flux which is attributed to the lower kinematic viscosity and higher thermal diffusivity. Changing from pure water to a water-Cu nanofluid, the ratio of pumping power to heat rate increases only slightly compared to reducing the channel height and inlet angle. The mechanism for heat transfer enhancement when reducing h is conduction, whereas convection is the main mechanism when using a smaller θ_o or changing to a nanofluid.

Device performance was compared to other single phase channel heat sinks for high heat cooling applications. Although the swirl flow channel heat sink absorbs about 25% of the heat flux achieved with other devices, the total pressure drop is much lower. This results in a ratio of pumping power to heat rate that is only about 20% of the lowest value reported in the literature reviewed. Therefore, the swirl flow channel heat sink is suitable for applications were low pumping cost is required. Furthermore, for high heat flux applications, using techniques that enhance heat transfer but also increase the pressure drop would be acceptable.

Chapter 6 presents the results of a theoretical and numerical analysis of the energy growth of initial disturbances and of the input-output response of temperature disturbances to forcing of the momentum components in a swirl flow channel heat sink. The steady state flow is solved using the integral method and spatial discretization followed by matrix inversion, as described in Chapter 2. The device is fabricated and experiments are conducted to visualize the flow and to measure the performance of the heat sink, that is, pressure drop and wall temperature as a function of flow rate for a given heat flux. Experimental results agree with numerical calculations for subcritical Reynolds numbers, therefore validating the base flow. Linearized perturbation equations with harmonic forcing are obtained using the local and parallel flow approximations based on order of magnitude arguments.

The effect of the flow rate Reynolds number on the base flow is presented. When Re_o increases, the flow direction on the channel midplane changes gradually from radial to azimuthal and eventually boundary layers separate. Results for the stability analysis show that there is no energy growth if the Reynolds number is less than $Re_o^E = 0.36$, and the flow becomes asymptotically unstable over $Re_o^c = 0.91$, which coincides with the separation of the boundary layers. As opposed to plane Poiseuille flow, there is very little transient growth between Re_o^E and Re_o^c, with an energy amplification only up to $O(10)$. This suggests that the mechanism for transition to turbulence is the crossflow instability that occurs due to the change in the shape of the base flow velocity profiles over Re_o^c. Our results are able to predict transition, as they present reasonable agreement with the flow visualization experiment and with observations made by Ruiz and Carey in Ref. [15].

The amplification of temperature perturbations to forcing of the radial, azimuthal, and wall-normal momentum components is calculated for a range of wavenumbers, waveangles and temporal frequencies. The most amplified spatial structures are streamwise vortices and streaks ($\omega = 0$) with a maximum response of order $O(10^3)$. As the forcing frequency increases, the dominant structures change their propagating direction, from crossflow to oblique to axisymmetric radial waves with amplification of order $O(10^2)$. At higher frequencies, streamwise propagating waves dominate for radial or wall-normal forcing, and azimuthally propagating waves dominate for azimuthal forcing, in both cases with amplifications of order $O(10)$.

Excitation of streamwise independent structures gives the largest amplification of temperature disturbances, becoming an attractive strategy to enhance heat transfer. To achieve this, we propose micromachining the channel walls with spiral grooves aligned with the predicted streamlines of the base flow. The response curve to this type of forcing shows that large amplifications occur for a narrow range of frequencies concentrated around $\omega = 0$ (stationary waves). Excitation of streamwise propagating waves results in only moderate amplification of temperature disturbances. Nonetheless, in order to generate these perturbations, we propose using a pulsating flow rate as a heat transfer enhancement technique due to its simple implementation. The response curve to this type of forcing shows a wide range of actuation frequencies with similar gains.

Heat sink performance using a pulsating flow rate is measured experimentally for the range of frequencies provided by the receptivity analysis. Compared to the unforced case, the RMS pressure drop is slightly higher, specially for low flow rates, and the wall temperature decreases significantly, with a difference of up to 5°C. In order to evaluate if the heat sink performance with pulsations is better than the performance in the unforced case, we calculate the pumping power reduction to get the same wall temperature, and the Nusselt enhancement using the same pumping power. A pumping power reduction of up to 26.6% was observed, along with a Nusselt enhancement of up to 10.3%.

In this work, a significant performance improvement for the swirl flow channel heat sink was achieved using a pulsating flow rate. Actuation parameters, in this case the range of pulsation frequencies, were determined by the receptivity analysis. This physics based approach can be extended to other heat transfer enhancement techniques, for instance, to select the wavelength of a wavy surface, the periodicity of surface roughness elements, or the frequency of acoustic vibrations.

7.2 Suggestions for future work

There are a number of extensions and open problems related to this work. A few promising directions are presented here.

Concerning the steady state in a swirl flow channel heat sink, correlations for the Nusselt number and skin friction factor may be obtained for each type of boundary layer structure. For the case of merged boundary layers with a fully developed velocity profile, a modified Graetz problem is obtained, hence an analytic solution can be sought. In addition to high heat flux cooling, this research line would be relevant to turbomachinery and geophysics.

Another investigation would involve the stability analysis including temperature dependent thermophysical properties and gravitational as well as rotational buoyancy. It would be interesting to determine whether a stabilizing or destabilizing effect is observed with respect to the present results.

With the increase in available computational power, fully global stability analyses are becoming commonplace and customary. If this approach is used, the local and parallel flow approximations would not be needed, which would reduce the uncertainty in the results. Future work should also consider designing an experiment to evaluate the effectiveness of other heat transfer enhancement techniques based on the receptivity analysis. Specifically, the proposed channel with micromachined spiral grooves may be tested using the setup for the performance measurement experiment, this would require manufacturing several heat sinks.

Another interesting extension to this work would be to include a physics simulation of the device being cooled. For instance, the thermal and electronic dynamics of a photovoltaic cell or an electronic chip may be coupled with the heat sink dynamics into one multiphysics problem. In addition, this may result in a non-uniform heat flux, such as in the case of hot spots in solar cells, and the consequences for the global stability of the flow should be investigated. The methodology presented in this thesis may be used for other physical dynamical systems in order to identify mechanisms that are of interest not only to control, but also to design technological devices.

Bibliography

[1] S. G. Kandlikar and W. J. Grande, "Evaluation of Single Phase Flow in Microchannels for High Heat Flux Chip Cooling—Thermohydraulic Performance Enhancement and Fabrication Technology," *Heat Transfer Eng.*, vol. 25, no. 8, pp. 5–16, 2004.

[2] M. Datta and H.-W. Choi, "Microheat exchanger for cooling high power laser diodes," *Appl. Therm. Eng.*, vol. 90, pp. 266–273, 2015.

[3] A. Royne, C. Dey, and D. Mills, "Cooling of photovoltaic cells under concentrated illumination: a critical review," *Sol. Energy Mater. Sol. Cells*, vol. 86, no. 4, pp. 451–483, 2005.

[4] J. Osses-Márquez and W. R. Calderón-Muñoz, "Thermal influence on charge carrier transport in solar cells based on GaAs PN junctions," *J. Appl. Phys.*, vol. 116, no. 15, p. 154502, 2014.

[5] W. R. Calderón-Muñoz and C. Jara-Bravo, "Hydrodynamic modeling of hot-carrier effects in a PN junction solar cell," *Acta Mech.*, pp. 1–14, 2016.

[6] B. Agostini, M. Fabbri, J. E. Park, L. Wojtan, J. R. Thome, and B. Michel, "State of the Art of High Heat Flux Cooling Technologies," *Heat Transfer Eng.*, vol. 28, no. 4, pp. 258–281, 2007.

[7] S. G. Kandlikar and A. V. Bapat, "Evaluation of Jet Impingement, Spray and Microchannel Chip Cooling Options for High Heat Flux Removal," *Heat Transfer Eng.*, vol. 28, no. 11, pp. 911–923, 2007.

[8] A. C. Kheirabadi and D. Groulx, "Cooling of server electronics: A design review of existing technology," *Appl. Therm. Eng.*, 2016.

[9] M. E. Steinke and S. G. Kandlikar, "Review of single-phase heat transfer enhancement techniques for application in microchannels, minichannels and microdevices," *International Journal of Heat and Technology*, vol. 22, no. 2, pp. 3–11, 2004.

[10] M. Meis, F. Varas, A. Velázquez, and J. Vega, "Heat transfer enhancement in microchannels caused by vortex promoters," *International Journal of Heat and Mass Transfer*, vol. 53, no. 1, pp. 29–40, 2010.

[11] L. Léal, M. Miscevic, P. Lavieille, M. Amokrane, F. Pigache, F. Topin, B. Nogarède, and

L. Tadrist, “An overview of heat transfer enhancement methods and new perspectives: Focus on active methods using electroactive materials,” *International Journal of Heat and Mass Transfer*, vol. 61, pp. 505–524, 2013.

[12] A. Dewan and P. Srivastava, “A review of heat transfer enhancement through flow disruption in a microchannel,” *Journal of Thermal Science*, vol. 24, no. 3, pp. 203–214, 2015.

[13] N. A. C. Sidik, M. N. A. W. Muhamad, W. M. A. A. Japar, and Z. A. Rasid, “An overview of passive techniques for heat transfer augmentation in microchannel heat sink,” *International Communications in Heat and Mass Transfer*, vol. 88, pp. 74–83, 2017.

[14] M. Ruiz and V. P. Carey, “Prediction of single phase heat and momentum transport in a spiraling radial inflow microchannel heat sink,” *ASME*, Jul 2012. Paper No. HT2012-58328.

[15] M. Ruiz and V. P. Carey, “Experimental study of single phase heat transfer and pressure loss in a spiraling radial inflow microchannel heat sink,” *J. Heat Transfer*, vol. 137, no. 7, p. 071702, 2015.

[16] H. Schlichting and K. Gersten, *Boundary-Layer Theory.* Springer, 2000.

[17] M. C. Breiter and K. Pohlhausen, “Laminar flow between two parallel rotating disks,” Tech. Rep. Technical Report No. 275562, ARL, USAF, 1962.

[18] W. Rice, “An Analytical and Experimental Investigation of Multiple-Disk Turbines,” *Journal of Engineering for Power*, vol. 87, no. 1, p. 29, 1965.

[19] K. E. Boyd and W. Rice, “Laminar Inward Flow of an Incompressible Fluid Between Rotating Disks, With Full Peripheral Admission,” *J. Appl. Mech.*, vol. 35, no. 2, p. 229, 1968.

[20] B. E. Boyack and W. Rice, “Integral Method for Flow Between Corotating Disks,” *J. Basic Engineering*, vol. 93, no. 3, p. 350, 1971.

[21] D. N. Wormley, “An Analytical Model for the Incompressible Flow in Short Vortex Chambers,” *J. Basic Engineering*, vol. 91, no. 2, p. 264, 1969.

[22] M. Firouzian, J. Owen, J. Pincombe, and R. Rogers, “Flow and heat transfer in a rotating cavity with a radial inflow of fluid Part 1: The flow structure,” *Int. J. Heat Fluid Flow*, vol. 6, no. 4, p. 228, 1985.

[23] J. Owen, “Air-cooled gas-turbine discs: a review of recent research,” *Int. J. Heat Fluid Flow*, vol. 9, no. 4, p. 354, 1988.

[24] D. May, J. W. Chew, and T. J. Scanlon, “Prediction of Deswirled Radial Inflow in Rotating Cavities With Hysteresis,” *J. Turbomach.*, vol. 135, no. 4, p. 041025, 2013.

[25] B. G. Vinod Kumar, J. W. Chew, and N. J. Hills, “Rotating Flow and Heat Transfer in Cylindrical Cavities With Radial Inflow,” *J. Eng. Gas Turbines Power*, vol. 135, no. 3, p. 032502, 2013.

[26] S. Mochizuki and W.-J. Yang, “Heat Transfer and Friction Loss in Laminar Radial Flows through Rotating Annular Disks,” *J. Heat Transfer*, vol. 103, no. 2, p. 212, 1981.

[27] S. Mochizuki and W.-J. Yang, “Local heat-transfer performance and mechanisms in radial flow between parallel disks,” *J. Thermophys. Heat Transfer*, vol. 1, no. 2, pp. 112–116, 1987.

[28] N. V. Suryanarayana, T. Scofield, and R. E. Kleiss, “Heat Transfer to a Fluid in Radial, Outward Flow Between Two Coaxial Stationary or Corotating Disks,” *J. Heat Transfer*, vol. 105, no. 3, p. 519, 1983.

[29] R. Devienne and G. Cognet, “Velocity field and heat transfer in a vortex flow exchanger,” *Wärme- und Stoffübertragung*, vol. 25, no. 3, pp. 185–191, 1990.

[30] G. Roy, S. J. Palm, and C. T. Nguyen, “Heat transfer and fluid flow of nanofluids in laminar radial flow cooling systems,” *J. of Therm. Sci.*, vol. 14, no. 4, pp. 362–367, 2005.

[31] I. Gherasim, G. Roy, C. T. Nguyen, and D. Vo-Ngoc, “Experimental investigation of nanofluids in confined laminar radial flows,” *Int. J. Therm. Sci.*, vol. 48, no. 8, pp. 1486–1493, 2009.

[32] I. Gherasim, G. Roy, C. T. Nguyen, and D. Vo-Ngoc, “Heat transfer enhancement and pumping power in confined radial flows using nanoparticle suspensions (nanofluids),” *Int. J. Therm. Sci.*, vol. 50, no. 3, pp. 369–377, 2011.

[33] R. T. Deam, E. Lemma, B. Mace, and R. Collins, “On Scaling Down Turbines to Millimeter Size,” *J. Eng. Gas Turbines Power*, vol. 130, no. 5, p. 052301, 2008.

[34] V. D. Romanin and V. P. Carey, “An integral perturbation model of flow and momentum transport in rotating microchannels with smooth or microstructured wall surfaces,” *Phys. Fluids*, vol. 23, no. 8, p. 082003, 2011.

[35] V. G. Krishnan, V. Romanin, V. P. Carey, and M. M. Maharbiz, “Design and scaling of microscale Tesla turbines,” *J. Micromech. Microeng.*, vol. 23, no. 12, p. 125001, 2013.

[36] A. Pfenniger, R. Vogel, V. M. Koch, and M. Jonsson, “Performance analysis of a miniature turbine generator for intracorporeal energy harvesting,” *Artif. Organs*, vol. 38, no. 5, p. E68, 2014.

[37] S. Sengupta and A. Guha, “A theory of Tesla disc turbines,” *Proceedings of the Institution of Mechanical Engineers, Part A: Journal of Power and Energy*, vol. 226, no. 5, p. 650, 2012.

[38] S. Sengupta and A. Guha, “Analytical and computational solutions for three-

dimensional flow-field and relative pathlines for the rotating flow in a Tesla disc turbine," *Computers & Fluids*, vol. 88, p. 344, 2013.

[39] A. Guha and S. Sengupta, "The fluid dynamics of the rotating flow in a Tesla disc turbine," *Eur. J. Mech. B. Fluids*, vol. 37, p. 112, 2013.

[40] A. Guha and S. Sengupta, "The fluid dynamics of work transfer in the non-uniform viscous rotating flow within a Tesla disc turbomachine," *Phys. Fluids*, vol. 26, no. 3, p. 033601, 2014.

[41] A. Guha and S. Sengupta, "Similitude and scaling laws for the rotating flow between concentric discs," *Proceedings of the Institution of Mechanical Engineers, Part A: Journal of Power and Energy*, vol. 228, no. 4, p. 429, 2014.

[42] R. Kobayashi, Y. Kohama, and C. Takamadate, "Spiral vortices in boundary layer transition regime on a rotating disk," *Acta Mech.*, vol. 35, no. 1-2, pp. 71–82, 1980.

[43] N. Gregory, J. T. Stuart, and W. S. Walker, "On the stability of three-dimensional boundary layers with application to the flow due to a rotating disk," *Phil. Trans. R. Soc. Lond.*, vol. 248, no. 943, pp. 155–199, 1955.

[44] M. R. Malik, "The neutral curve for stationary disturbances in rotating-disk flow," *J. Fluid Mech.*, vol. 164, pp. 275–287, 1986.

[45] O. Savas, "Circular waves on a stationary disk in rotating flow," *Phys. Fluids*, vol. 26, no. 12, p. 3445, 1983.

[46] O. Savas, "Stability of Bödewadt flow," *J. Fluid Mech.*, vol. 183, no. -1, p. 77, 1987.

[47] R. J. Lingwood, "Absolute instability of the boundary layer on a rotating disk," *J. Fluid Mech.*, vol. 299, pp. 17–33, 1995.

[48] E. Serre, E. C. del Arco, and P. Bontoux, "Annular and spiral patterns in flows between rotating and stationary discs," *J. Fluid Mech.*, vol. 434, pp. 65–100, 2001.

[49] S. O. MacKerrell, "Stability of Bödewadt flow," *Philosophical Transactions of the Royal Society A: Mathematical, Physical and Engineering Sciences*, vol. 363, no. 1830, pp. 1181–1187, 2005.

[50] J. M. Lopez, F. Marques, A. M. Rubio, and M. Avila, "Crossflow instability of finite Bödewadt flows: Transients and spiral waves," *Phys. Fluids*, vol. 21, no. 11, p. 114107, 2009.

[51] Y. Do, J. M. Lopez, and F. Marques, "Optimal harmonic response in a confined Bödewadt boundary layer flow," *Phys. Rev. E*, vol. 82, no. 3, p. 036301, 2010.

[52] F. Marques, A. Y. Gelfgat, and J. M. Lopez, "Tangent double Hopf bifurcation in a differentially rotating cylinder flow," *Phys. Rev. E*, vol. 68, no. 1, p. 016310, 2003.

[53] J. Mizushima, G. Sugihara, and T. Miura, “Two modes of oscillatory instability in the flow between a pair of corotating disks,” *Phys. Fluids*, vol. 21, no. 1, p. 014101, 2009.

[54] C. Panades, F. Marques, and A. Meseguer, “Mode competition in cylindrical flows driven by sidewall oscillations,” *Phys. Rev. E*, vol. 87, no. 4, p. 043001, 2013.

[55] J. M. Lopez and F. Marques, “Rapidly rotating cylinder flow with an oscillating sidewall,” *Phys. Rev. E*, vol. 89, no. 1, p. 013013, 2014.

[56] O. Reynolds, “An experimental investigation of the circumstances which determine whether the motion of water shall be direct or sinuous, and of the law of resistance in parallel channels,” *Philos. Trans. R. Soc. Lond.*, vol. 174, pp. 935–982, 1883.

[57] P. G. Drazin and W. H. Reid, *Hydrodynamic stability.* Cambridge university press, 2004.

[58] W. M. Orr, “The stability or instability of the steady motions of a perfect liquid and of a viscous liquid,” *Proc. R. Irish Acad. A*, vol. 27, pp. 9–138, 1907.

[59] A. Sommerfeld, “Ein beitrag zur hydrodynamischen erklaerung der turbulenten fluessigkeitsbewegungen,” *Proc. 4th Int. Congr. Math., Rome*, pp. 116–124, 1908.

[60] S. A. Orszag, “Accurate solution of the Orr-Sommerfeld stability equation,” *J. Fluid Mech.*, vol. 50, pp. 689–703, 1971.

[61] D. Joseph, *Stability of Fluid Motions I.* New York: Springer-Verlag, 1976.

[62] W. Tollmien, “Über die entstehung der turbulenz,” *Nachr. Ges. Wiss. Göttingen*, pp. 21–44, 1929.

[63] H. Schlichting, “Berechnung der anfachung kleiner störungen bei der plattenströmung,” *ZAMM*, vol. 13, pp. 171–174, 1933.

[64] G. B. Schubauer and H. K. Skramstad, “Laminar boundary-layer oscillations and transition on a flat plate,” *J. Res. Nat. Bur. Stand.*, vol. 38, pp. 251–292, 1947.

[65] P. Klebanoff, K. Tidstrom, and L. Sargent, “The three-dimensional nature of boundary layer instability,” *J. Fluid Mech.*, vol. 12, pp. 1–34, 1962.

[66] S. A. Orszag and P. A. T., “Secondary instability of wall-bounded shear flows,” *J. Fluid Mech.*, vol. 128, pp. 347–385, 1983.

[67] T. Herbert, “Secondary instability of boundary layers,” *Annu. Rev. Fluid Mech.*, vol. 20, pp. 487–526, 1988.

[68] L. M. Mack, “The inviscid stability of the compressible laminar boundary layer,” *Space Progr. Summ.*, vol. 37-23, p. 297, 1963.

[69] G. Taylor, “Stability of a viscous liquid contained between two rotating cylinders,” *Philos. Trans. R. Soc. Lond. A*, vol. 223, pp. 289–343, 1923.

[70] M. Gaster, "On the generation of spatially growing waves in the theory of hydrodynamic stability," *J. Fluid Mech.*, vol. 22, pp. 433–441, 1965.

[71] P. Huerre and P. A. Monkewithz, "Local and global instabilities of spatially developing flows," *Annu. Rev. Fluid Mech.*, vol. 22, pp. 473–537, 1990.

[72] F. Bertolotti, T. Herbert, and P. Spalart, "Linear and nonlinear stability of the blasius boundary layer," *J. Fluid Mech.*, vol. 242, pp. 441–474, 1992.

[73] C.-L. Chang and M. R. Malik, "Oblique mode breakdown and secondary instability in supersonic boundary layers," *J. Fluid Mech.*, vol. 273, pp. 323–360, 1994.

[74] M. V. Dyke, *An Album of Fluid Motion.* The Parabolic Press, 14th edition, 2012.

[75] K. M. Butler and B. F. Farrel, "Three-dimensional optimal perturbations in viscous shear flows," *Phys. Fluids A*, vol. 4, pp. 1637–1650, 1992.

[76] L. H. Gustavsson, "Energy growth of three-dimensional disturbances in plane poiseuille flow," *J. Fluid Mech.*, vol. 224, pp. 241–260, 1991.

[77] S. C. Reddy and D. S. Henningson, "Energy growth in viscous channel flows," *J. Fluid Mech.*, vol. 252, pp. 209–238, 1993.

[78] S. C. Reddy, P. J. Schmid, and D. S. Henningson, "Pseudospectra of the Orr-Sommerfeld operator," *SIAM J. Appl. Math.*, vol. 53, pp. 15–47, 1993.

[79] L. N. Trefethen, A. E. Trefethen, S. C. Reddy, and T. A. Driscoll, "Hydrodynamic stability without eigenvalues," *Science*, vol. 261, no. 5121, pp. 578–584, 1993.

[80] P. J. Schmid and D. S. Henningson, *Stability and transition in shear flows.* New York: Springer-Verlag, 2001.

[81] P. J. Schmid, "Nonmodal stability theory," *Annu. Rev. Fluid Mech.*, vol. 39, no. 1, pp. 129–162, 2007.

[82] P. J. Schmid and L. Brandt, "Analysis of fluid systems: Stability, receptivity, sensitivity," *Appl. Mech. Rev.*, vol. 66, no. 2, p. 024803, 2013.

[83] M. R. Jovanović and B. Bamieh, "Componentwise energy amplification in channel flows," *J. Fluid Mech.*, vol. 534, pp. 145–183, 2005.

[84] A. Mager, "Generalization of boundary-layer momentum-integral equations to three-dimensional flows including those of rotating system," Tech. Rep. 1067, NACA, 1952.

[85] J. M. Owen, J. R. Pincombe, and R. H. Rogers, "Source-sink flow inside a rotating cylindrical cavity," *J. Fluid Mech.*, vol. 155, p. 233, 1985.

[86] L. N. Trefethen, *Spectral Methods in MATLAB.* Cambridge University Pr., 2000.

[87] F. S. Alfio Quarteroni, Riccardo Sacco, *Numerical Mathematics.* Springer Berlin Hei-

delberg, 2010.

[88] D. A. A. Richard H. Pletcher, John C. Tannehill, *Computational Fluid Mechanics and Heat Transfer*. Taylor & Francis Inc, 2012.

[89] L. H. Gustavsson, "Excitation of direct resonances in plane Poiseuille flow," *Stud. Appl. Math.*, vol. 75, no. 3, pp. 227–248, 1986.

[90] L. N. Trefethen and M. Embree, *Spectra and Pseudospectra: The Behavior of Nonnormal Matrices and Operators*. Princeton Uni. Press, 2005.

[91] K. Zhou, J. C. Doyle, K. Glover, *et al.*, *Robust and optimal control*, vol. 40. Prentice hall New Jersey, 1996.

[92] P. Benner and H. Faßbender, *Model Order Reduction: Techniques and Tools*, pp. 1–10. London: Springer London, 2013.

[93] A. C. Antoulas, *Approximation of Large-Scale Dynamical Systems*. SIAM, 2005.

[94] F. M. White, *Fluid Mechanics*. McGraw-Hill Education Ltd, 2011.

[95] Y. Xuan and Q. Li, "Heat transfer enhancement of nanofluids," *Int. J. Heat Fluid Flow*, vol. 21, no. 1, pp. 58–64, 2000.

[96] S. P. Jang and S. U. Choi, "Cooling performance of a microchannel heat sink with nanofluids," *Appl. Therm. Eng.*, vol. 26, no. 17-18, pp. 2457–2463, 2006.

[97] M. Rafati, A. Hamidi, and M. S. Niaser, "Application of nanofluids in computer cooling systems (heat transfer performance of nanofluids)," *Appl. Therm. Eng.*, vol. 45-46, pp. 9–14, 2012.

[98] S. Kakac and A. Pramuanjaroenkij, "Review of convective heat transfer enhancement with nanofluids," *Int. J. Heat Mass Transfer*, vol. 52, no. 13-14, pp. 3187–3196, 2009.

[99] M. Ghanbarpour, N. Nikkam, R. Khodabandeh, and M. Toprak, "Improvement of heat transfer characteristics of cylindrical heat pipe by using SiC nanofluids," *Appl. Therm. Eng.*, vol. 90, pp. 127–135, 2015.

[100] J. Wu, J. Zhao, J. Lei, and B. Liu, "Effectiveness of nanofluid on improving the performance of microchannel heat sink," *Appl. Therm. Eng.*, 2016.

[101] P. C. Mishra, S. Mukherjee, S. K. Nayak, and A. Panda, "A brief review on viscosity of nanofluids," *International Nano Letters*, vol. 4, no. 4, pp. 109–120, 2014.

[102] H. C. Brinkman, "The Viscosity of Concentrated Suspensions and Solutions," *The Journal of Chemical Physics*, vol. 20, no. 4, p. 571, 1952.

[103] R. L. Hamilton and O. K. Crosser, "Thermal Conductivity of Heterogeneous Two-Component Systems," *Ind. Eng. Chem. Fund.*, vol. 1, no. 3, pp. 187–191, 1962.

[104] S. Murshed, K. Leong, and C. Yang, “Thermophysical and electrokinetic properties of nanofluids – A critical review,” *Appl. Therm. Eng.*, vol. 28, no. 17-18, pp. 2109–2125, 2008.

[105] G. Puliti, S. Paolucci, and M. Sen, “Nanofluids and Their Properties,” *Appl. Mech. Rev.*, vol. 64, no. 3, p. 030803, 2012.

[106] S. Kandlikar, S. Garimella, D. Li, S. Colin, and M. R. King, *Heat transfer and fluid flow in minichannels and microchannels.* Elsevier, 2005.

Appendix A

Wolfram Mathematica subroutines

Subroutines programmed using *Wolfram Mathematica 10.3* are here presented. The first code does four steps of *4th* order Runge Kutta and saves them to initialize the adaptive Adams predictor-corrector method shown in the second code. The last subroutine calculates the Chebyshev differentiation and integration matrices used throughout this work.

```
(*saves four steps of 4th order Runge Kutta to initialize Adams method*)
rk4[I_,h_]:= Module[{},
 For[i=1,i<=3,i++,
  k1=h*f[X[[I+i]],Y[[I+i]]];
  k2=h*f[X[[I+i]]+h/2,Y[[I+i]]+k1/2];
  k3=h*f[X[[I+i]]+h/2,Y[[I+i]]+k2/2];
  k4=h*f[X[[I+i]]+h,Y[[I+i]]+k3];
  AppendTo[Y,Y[[I+i]]+k1/6+(k2+k3)/3+k4/6];
  AppendTo[X,X[[I+i]]+h];
 ];
 F0=f[X[[I+1]],Y[[I+1]]];
 F1=f[X[[I+2]],Y[[I+2]]];
 F2=f[X[[I+3]],Y[[I+3]]];
 F3=f[X[[I+4]],Y[[I+4]]];
];
```

```
adams[Emin_,Emax_]:=Module[{},
 (*initialize with 4th order Runge Kutta*)
 rk4[0,dx];
 For[j=4,X[[j]]<Xend,j++,
  (*4th order Adams-Bashforth predictor step*)
  Yp=Y[[j]]+(dx/24)*(-9*F0+37*F1-59*F2+55*F3);
  (*4th order Adams-Moulton corrector step*)
  Yc=Y[[j]]+(dx/24)*(F1-5*F2+19*F3+9*f[X[[j]]+dx,Yp]);
  (*calculate local truncation error*)
  LTE=(19/270)*Max[Abs[Yc-Yp]];
  (*if LTE is out of bounds, adapt dx and reinitialize*)
  If[LTE<=Emin,
   dx=2*dx; rk4[j-1,dx]; j=j+2,
   If[LTE>=Emax,
    dx=dx/2; rk4[j-1,dx]; j=j+2,
    AppendTo[Y,Yc];
    AppendTo[X,X[[j]]+dx];
    F0=F1;
    F1=F2;
    F2=F3;
    F3=f[X[[j+1]],Y[[j+1]]];
]]]];
```

```
(*calculate Chebyshev differentiation and integration matrices*)
cheb[n_]:=Module[{c,Z,dZ,S,\[Theta],w,v},
  c=Table[1*(-1)^i,{i,0,n-1}];
  c[[1]]=2;
  c[[n]]=2(-1)^(n-1);
  z=Cos[Pi*(Range[0,n-1]/(n-1))];
  z=N[z,MachinePrecision];
  Z=Table[z,{n}]\[Transpose];
  dZ=Z-Z\[Transpose];
  D1=KroneckerProduct[c,1/c]/(dZ+IdentityMatrix[n]);
  D1=D1-DiagonalMatrix[Sum[D1\[Transpose][[i]],{i,1,n}]];
  D1=N[D1,MachinePrecision];
  D2=N[D1.D1,MachinePrecision];
  D3=N[D1.D1.D1,MachinePrecision];
  S=DiagonalMatrix[Join[{0},1/(1-z[[2;;n-1]]^2),{0}]]  ;
  D4=((1-z^2)D2.D2-8 z D1.D2-12 D2).S;
  D4=N[D4,MachinePrecision];
  \[Theta]=ArcCos[z];
  w=Table[0,{n}];
  v=Table[1,{n-2}];
  If[Floor[(n-1)/2]==(n-1)/2,
   w[[1]]=1/((n-1)^2-1);
   w[[n]]=w[[1]];
   Do[
     v=v-2Cos[2k\[Theta][[2;;n-1]]]/(4k^2-1),
   {k,1,(n-1)/2-1}];
   v=v-Cos[(n-1)\[Theta][[2;;n-1]]]/((n-1)^2-1),
   w[[1]]=1/(n-1)^2;
   w[[n]]=w[[1]];
   Do[
     v=v-2Cos[2k\[Theta][[2;;n-1]]]/(4k^2-1),
   {k,1,(n-2)/2}];
  ];
  w[[2;;n-1]]=2v/(n-1);
  wI=N[w,MachinePrecision];
  WI=Table[0,{n},{n}];
  Do[
   WI[[i,1;;i]]=wI[[1;;i]],
  {i,1,n}];
];
```

Appendix B

Heat sink fabrication schematic

The fabrication schematic of the swirl flow channel heat sink used for the performance measurement experiment is here presented.

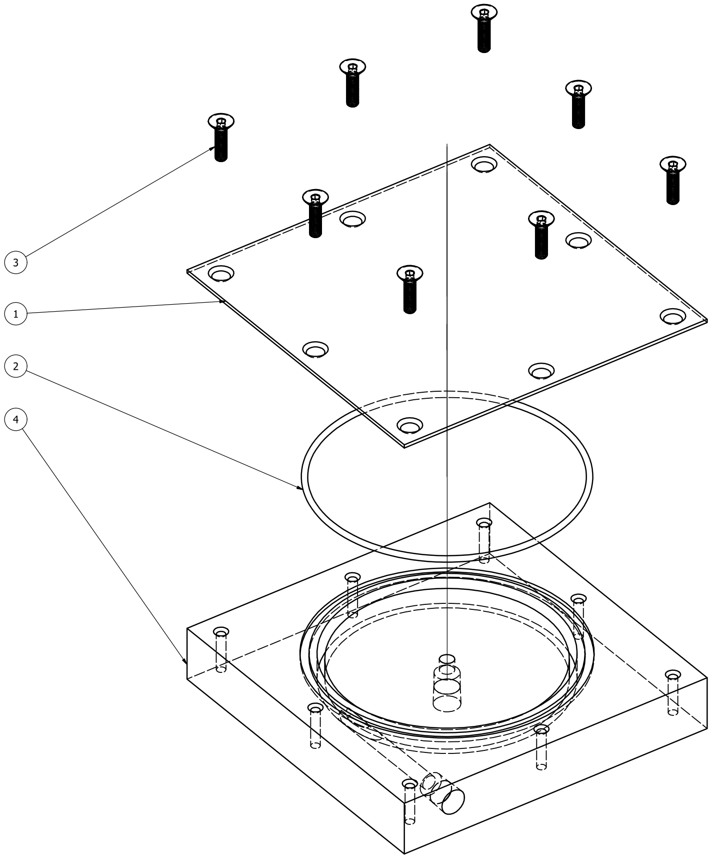

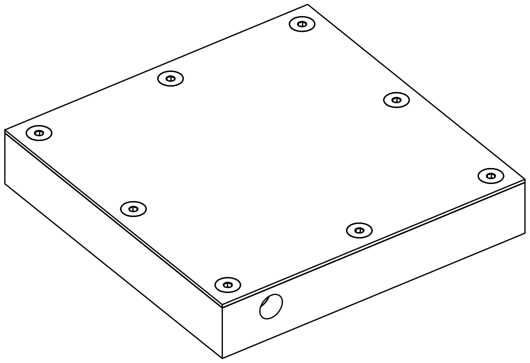

PARTS LIST			
ITEM	QTY	PART NUMBER	DESCRIPTION
1	1	1	6061 Aluminum cover
2	1	2	High temperature EDPM O-Ring 3/32'' wd, n° 157
3	8	3	Stainless steel hex drive flat head screw 10-32 x 3/4"
4	1	4	Cast Nylon minichannel

DRAWN
Benjamin Herrmann 7/7/2017
CHECKED
QA
MFG
APPROVED

TITLE
Minichannel heat sink

SIZE D
DWG NO 0
REV
SCALE 1 : 1
SHEET 1 OF 3

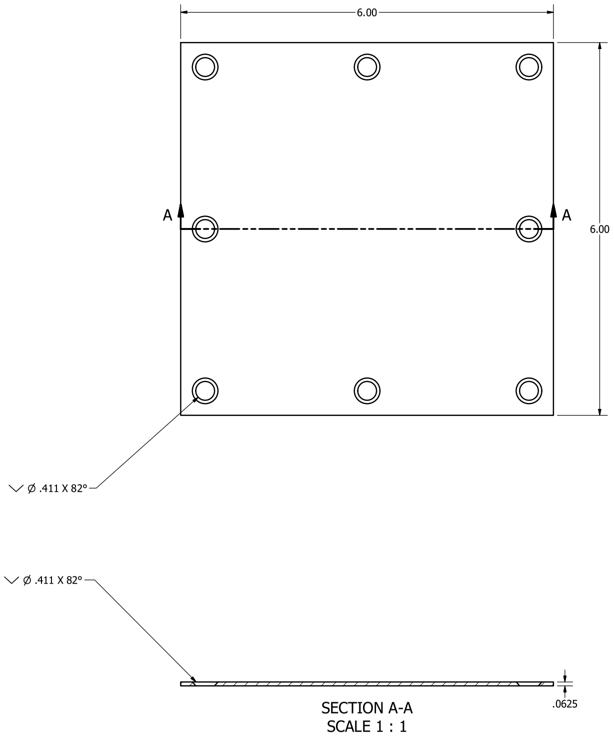

SECTION A-A
SCALE 1 : 1

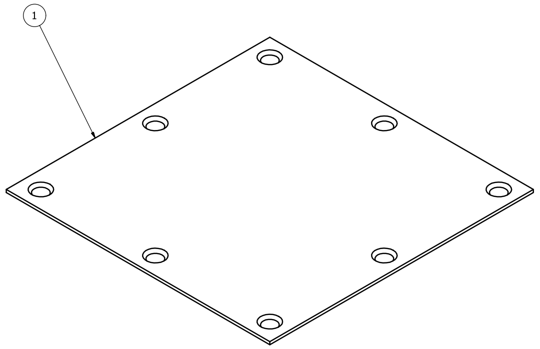

DRAWN Benjamin Herrmann	7/7/2017	
CHECKED		TITLE
QA		Minichannel heat sink
MFG		
APPROVED		
		SIZE D · DWG NO 0 · REV
		SCALE 1 : 1 · SHEET 2 OF 3

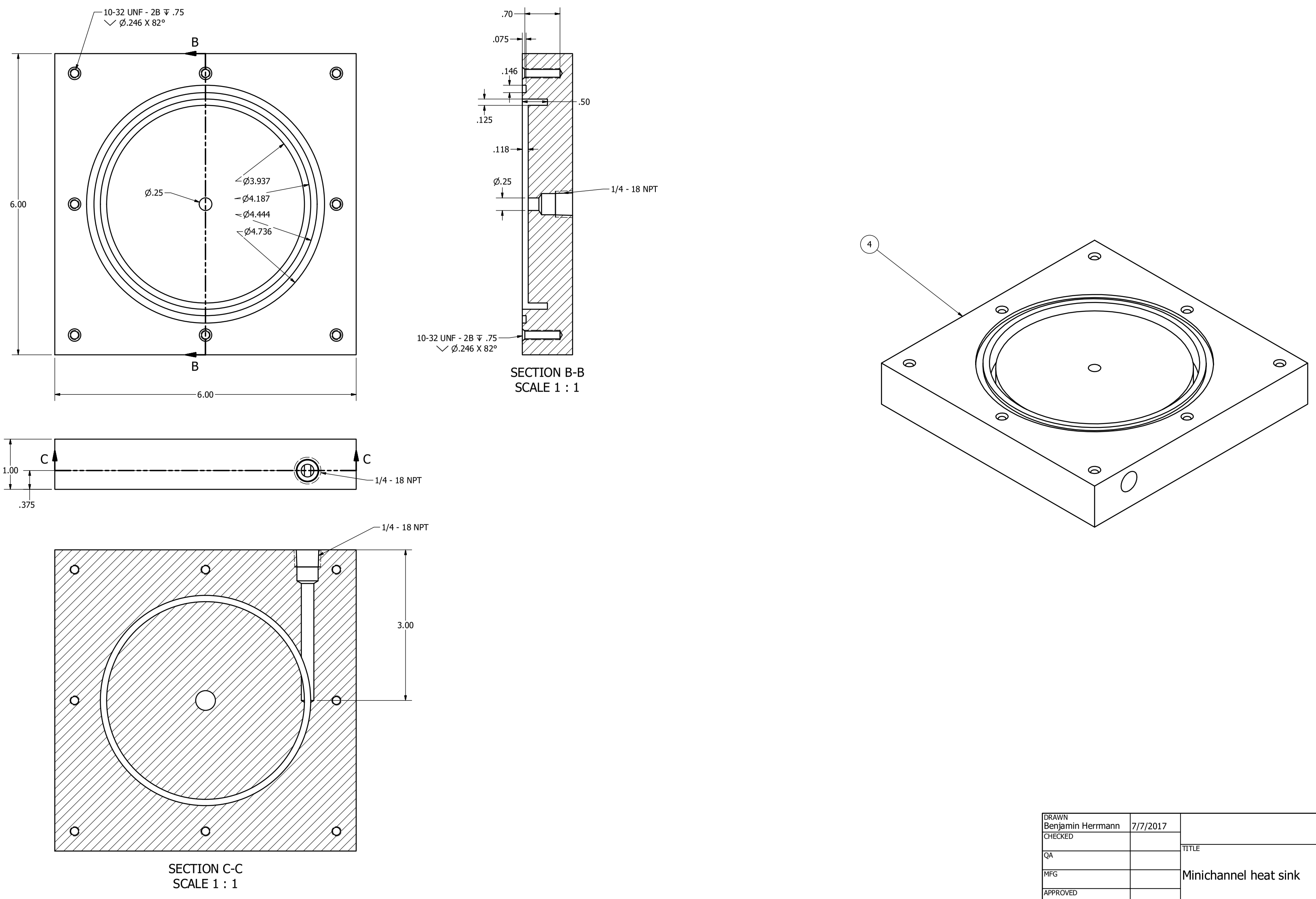

DRAWN Benjamin Herrmann	7/7/2017	
CHECKED		TITLE
QA		Minichannel heat sink
MFG		
APPROVED		SIZE D · DWG NO 0 · REV
		SCALE 1 : 1 · SHEET 3 OF 3

Appendix C

NI Labview code for data acquisition

The routine programmed in *NI Labview 2015* used for data acquisition in the performance measurement experiment is here presented.

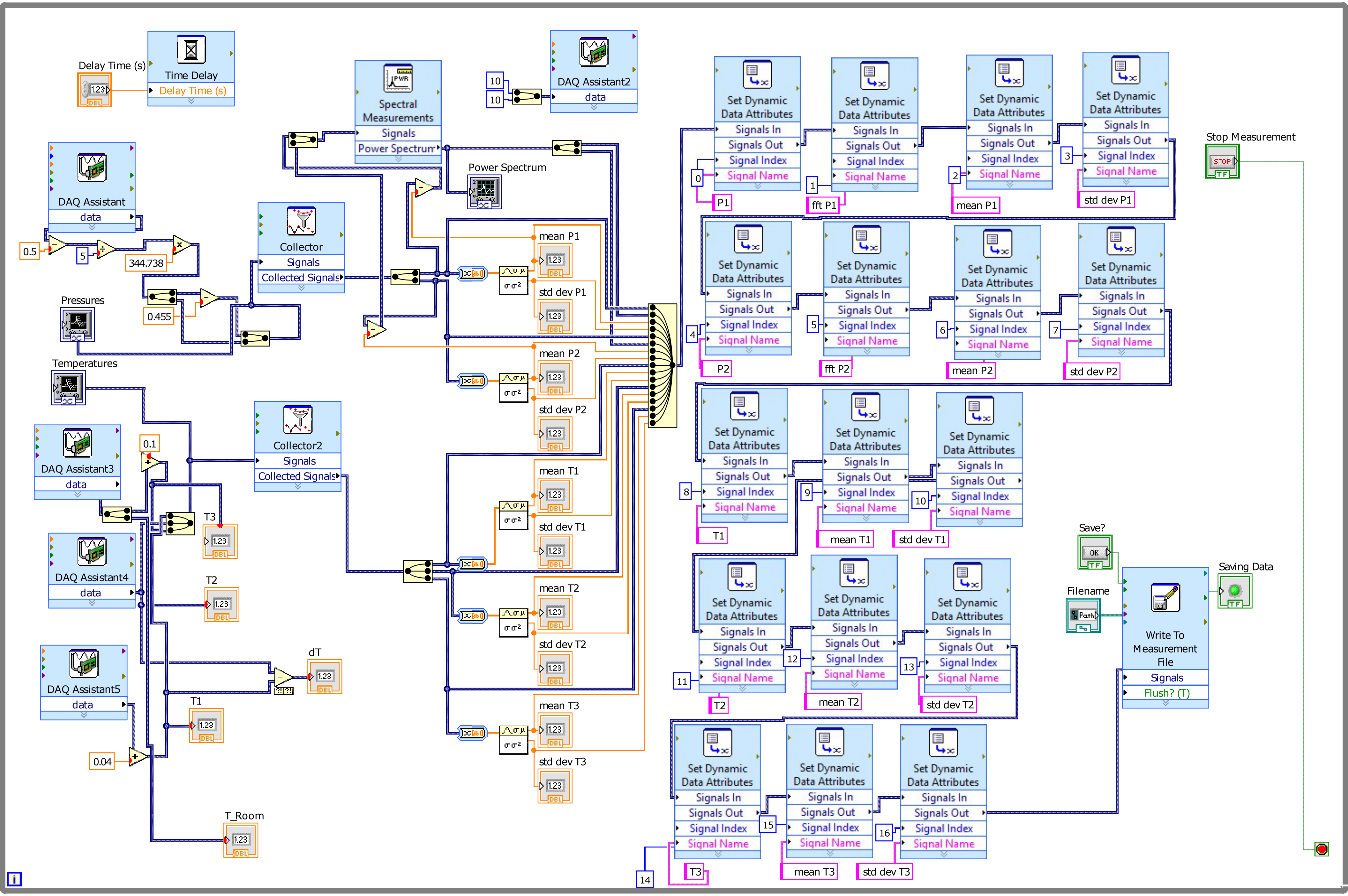
Delay Time (s)
Time Delay
Delay Time (s)
Spectral Measurements
Signals
Power Spectrum
10
10
DAQ Assistant2
data
DAQ Assistant
data
0.5
5
344.738
Collector
Signals
Collected Signals
Power Spectrum
Pressures
0.455
Temperatures
DAQ Assistant3
data
0.1
Collector2
Signals
Collected Signals
T3
DAQ Assistant4
data
T2
dT
DAQ Assistant5
data
T1
0.04
T_Room
mean P1
std dev P1
mean P2
std dev P2
mean T1
std dev T1
mean T2
std dev T2
mean T3
std dev T3
Set Dynamic Data Attributes
Signals In
Signals Out
Signal Index
Signal Name
0
P1
1
fft P1
2
mean P1
3
std dev P1
4
P2
5
fft P2
6
mean P2
7
std dev P2
8
T1
9
mean T1
10
std dev T1
11
T2
12
mean T2
13
std dev T2
14
T3
15
mean T3
16
std dev T3
Stop Measurement
STOP
Save?
OK
Filename
Write To Measurement File
Signals
Flush? (T)
Saving Data